

Single Electrons from Decays of Heavy Quarks Produced in Cu+Cu Collisions at the Relativistic Heavy Ion Collider

A Dissertation Presented

by

Nicole Jean Apadula

to

The Graduate School

in Partial Fulfillment of the Requirements

for the Degree of

Doctor of Philosophy

in

Physics

Stony Brook University

May 2013

UMI Number: 3564347

All rights reserved

INFORMATION TO ALL USERS

The quality of this reproduction is dependent upon the quality of the copy submitted.

In the unlikely event that the author did not send a complete manuscript and there are missing pages, these will be noted. Also, if material had to be removed, a note will indicate the deletion.



UMI 3564347

Published by ProQuest LLC (2013). Copyright in the Dissertation held by the Author.

Microform Edition © ProQuest LLC.

All rights reserved. This work is protected against unauthorized copying under Title 17, United States Code



ProQuest LLC.
789 East Eisenhower Parkway
P.O. Box 1346
Ann Arbor, MI 48106 - 1346

Copyright by
Nicole Jean Apadula
2013

Stony Brook University

The Graduate School

Nicole Jean Apadula

We, the dissertation committee for the above candidate for the Doctor of Philosophy degree, hereby recommend acceptance of this dissertation.

Dr. Axel Drees – Dissertation Advisor
Department of Physics and Astronomy, Stony Brook University

Dr. Derek Teaney – Chairperson of Defense
Department of Physics and Astronomy, Stony Brook University

Dr. Thomas Weinacht
Department of Physics and Astronomy, Stony Brook University

Dr. Martin Purshcke
Department of Physics, Brookhaven National Laboratory

This dissertation is accepted by the Graduate School.

Charles Taber
Interim Dean of the Graduate
School

Abstract of the Dissertation

**Single Electrons from Decays of Heavy Quarks
Produced in Cu+Cu Collisions at the
Relativistic Heavy Ion Collider**

by

Nicole Jean Apadula

Doctor of Philosophy

in

Physics

Stony Brook University

2013

The PHENIX experiment at the Relativistic Heavy Ion Collider (RHIC) has measured charm and bottom quark production at mid-rapidity in p+p, d+Au, and Au+Au collisions at $\sqrt{s} = 200 \text{ GeV}$ through their semi-leptonic decay into electrons. The large mass of the charm and bottom quarks means they are formed predominately by gluon-gluon fusion in the initial hard scatterings at RHIC and thus experience the full evolution of the medium, making them a good probe of medium effects. The yield in central Au+Au collisions is suppressed relative to p+p collisions, suggesting that the heavy quarks lose a significant portion of their initial energy in the medium. The d+Au results are enhanced relative to the p+p,

pointing to cold nuclear matter effects that are masked by the hot medium in the Au+Au collisions. Studies of the intermediately sized Cu+Cu system provide a way to explore these competing effects as a function of system size and number of participating nucleons. In this dissertation, measurements of electrons from the decays of heavy quarks produced in Cu+Cu collisions are presented. We examine the interplay between hot and cold nuclear matter effects on open heavy flavor by comparing the results to those already measured in Au+Au and d+Au collisions. It has already been shown in the central Au+Au that partonic energy loss models are insufficient to describe the level of suppression. New models that include cold nuclear matter effects and the addition of meson dissociation are shown and compared to the Cu+Cu results.

To Giovanni, Santino and the love of my life, Felice.

Contents

List of Figures	viii
List of Tables	xii
Acknowledgements	xiii
1 Introduction	1
1.1 Motivation	1
1.2 Heavy Flavor at RHIC	3
2 PHENIX Experiment	10
2.1 PHENIX Detector Overview	10
2.2 Global Detectors	11
2.2.1 Beam-Beam Counter	11
2.3 Central Arm	16
2.3.1 Magnet	16
2.3.2 Drift Chamber	16
2.3.3 Pad Chamber	21
2.3.4 Ring-Imaging Cherenkov Detector	23
2.3.5 Electromagnetic Calorimeter	25
3 Data Analysis	29
3.1 Event Selection	29
3.2 Electron Track Selection	30
3.2.1 Electron Identification	30
3.3 Run Selection	32
3.4 Randomly Associated Tracks	33
3.5 Trigger Efficiency	38
3.6 Single Electron Efficiency	45
3.6.1 Tuning Detector Response	46
3.6.2 RICH cut correction	47

3.6.3	Acceptance×efficiency correction	54
3.6.4	Invariant yield	55
4	Estimation of Electron Background Sources	59
4.1	Cocktail Method	60
4.1.1	Light Mesons	60
4.1.2	Pion double check	63
4.1.3	Conversions	64
4.1.4	Ke3 Decays	68
4.1.5	Direct Photon Contributions	68
4.1.6	Quarkonia and Drell-Yan	69
4.1.7	Total cocktail	72
4.2	Converter Analysis	73
4.3	Comparison of the Two Methods	77
4.3.1	R_{NP}	77
5	Systematic Error Estimation	81
5.1	Inclusive Yield	81
5.1.1	Run Group Correction	81
5.1.2	Electron Identification	81
5.1.3	Geometric Matching	82
5.1.4	Trigger Efficiency	82
5.1.5	Total Inclusive Systematic Error	84
5.2	Cocktail	84
5.3	Converter	85
6	Results and Discussion	87
6.1	Heavy Flavor Spectra	87
6.2	Nuclear Modification Factor	88
6.3	Comparison to Theory	104
6.3.1	Partonic Energy Loss	105
6.3.2	Dissociation	106
6.3.3	The Energy Loss Picture	108
6.4	Comparison to Forward Results	110
7	Conclusion	116
A	Heavy Flavor Spectra	118
B	R_{CuCu}	124
	Bibliography	130

List of Figures

1.1	QCD phase diagram	2
1.2	Some decay diagrams.	4
1.3	Non-photonic electron yield in Au+Au collisions scaled by the number of binary collisions	4
1.4	Open heavy-flavor electron R_{AuAu} compared to various energy loss models	6
1.5	R_{dA} and R_{AA} for π^0 and e_{HF}^\pm	7
1.6	Cartoon showing the N_{coll} range of the d+Au, Cu+Cu and Au+Au systems. Cu+Cu provides the bridge to tie the d+Au and Au+Au results together.	8
2.1	PHENIX detector in the 2004 RHIC run, same as the 2005 run with the exception of the MVD. Beam view, looking down the north going beam direction.	12
2.2	PHENIX detector in the 2004 RHIC run, same as the 2005 run with the exception of the MVD. Side view, looking at the West side of the detector.	13
2.3	Schematic view of the BBC.	14
2.4	BBC Charge North+South Distribution for minimum bias events.	15
2.5	Magnetic field lines for the two central magnet coils in combined (++) field mode.	17
2.6	DC frame.	19
2.7	Left: Layout of wire position in one sector and anode net configuration. Right: Top view of UV wire orientation.	20
2.8	A sample track with the Hough Transform parameters.	22
2.9	Schematic of the placement of the PC.	23
2.10	Cartoon of Čerenkov radiation.	24
2.11	Top (a): A cutaway view of one arm of the RICH. Bottom (b): Schematic of the RICH.	26
2.12	PbSc and PbGl	28
3.1	Derivation of RICH variables n0 and n1.	31

3.2	Number of electrons per event as a function of PHENIX run number for MB triggered events.	34
3.3	Number of electrons per event as a function of PHENIX run number for ERT triggered events.	35
3.4	Number of electrons per event as a function of PHENIX run number for MB triggered events after run removal procedure.	36
3.5	Number of electrons per event as a function of PHENIX run number for ERT triggered events after run removal procedure.	37
3.6	E/p graphs with electrons passing the $n_1 \geq 5$ cut in red, $sn_1 \geq 5$ cut in blue and the difference in black.	38
3.7	Uncorrected MB spectra for both the n_1 and sn_1 cuts.	39
3.8	Uncorrected MB and ERT spectra from group A.	41
3.9	Uncorrected MB and ERT spectra from group B.	42
3.10	Trigger efficiencies for group A(left) and group B(right). Each is fit separately to a Fermi-like function.	43
3.11	Ratio of corrected ERT spectra and MB spectra for group A(top) and group B(bottom).	44
3.12	Top: From left, n_1 , prob and emcdtrk_e for p_T 1-2 GeV. Bottom: same for p_T 2-5 GeV.	46
3.13	The E/p distribution fit with a Gaussian. Left: MB data. Right: Simulation.	47
3.14	Mean of each Gaussian fit plotted vs p_T	48
3.15	Sigma of each Gaussian fit plotted vs p_T	49
3.16	$\cos(\theta_0)$ vs bbc_z in data on left and in simulation on the right.	50
3.17	Comparison of real and simulated phi distributions. Data is in red.	51
3.18	Comparison of real and simulated zed distribution for the west arm. Data is in red.	52
3.19	Comparison of real and simulated zed distribution for the east arm. Data is in red.	53
3.20	Left: Ratio of the $n_1 \geq 3$ and $n_1 \geq 5$ spectra. Right: Ratio of $sn_1 \geq 3$ and $sn_1 \geq 5$ spectra.	54
3.21	Acc* Eff curve.	55
3.22	Fully corrected inclusive electron spectrum for MB and 5 centralities.	58
4.1	Hagedorn fit to the neutral pion data in MB and 5 centralities.	61
4.2	Ratio of the data to the fit for MB and 5 centralities.	62
4.3	Left: π_{new} in black, $(\pi)_{\text{cocktail}}$ in red. Right: Ratio of π_{new} and $(\pi)_{\text{cocktail}}$	65

4.4	Hagedorn fit to the combination of π_{new} and the original neutral pions. π_{new} ends at 3 GeV where the statistics start to run out.	66
4.5	Ratios of π_{new} and $(\pi)_{\text{cocktail}}$ for a second iteration for MB and 5 centralities.	67
4.6	Kaplan fit to J/ψ spectra	69
4.7	Kaplan fit to the 0-10% central J/ψ bin.	70
4.8	Kaplan fit to the MB J/ψ bin.	71
4.9	The background electron cocktail for MB.	72
4.10	$d\eta/d\phi$ for the converter runs in red and non-converter runs in black.	73
4.11	Minimum bias inclusive yield for the converter(red) and non-converter (black) runs.	74
4.12	The p_T dependence of R_γ	75
4.13	R_{CN} for MB and 5 centralities. Y-intercept value is approximately R_γ	76
4.14	The ratio of the photonic spectra as determined by the converter and the photonic cocktail for MB and 5 centralities.	78
4.15	R_{NP} for the cocktail method (black) and converter method (red) for MB and 5 centralities.	80
5.1	Loose, standard and tight eid cuts. Spread is systematic error on electron identification.	83
5.2	Minimum Bias cocktail systematic errors.	85
5.3	Minimum Bias converter systematic errors.	86
6.1	Yield of electrons from open heavy flavor.	89
6.2	Nuclear modification factor for minimum bias collisions.	90
6.3	Nuclear modification factor for 0-10% central collisions.	91
6.4	Nuclear modification factor for 0-20% central collisions.	92
6.5	Nuclear modification factor for 20-40% collisions.	93
6.6	Nuclear modification factor for 40-60% collisions.	94
6.7	Nuclear modification factor for 60-94% central collisions.	95
6.8	R_{CP} for four centralities.	96
6.9	Top: $R_{\text{AuAu},20-40}$ and $R_{\text{CuCu},0-10}$. Bottom: $R_{\text{AuAu},40-60}$ and $R_{\text{CuCu},0-20}$	97
6.10	Top: $R_{\text{dAu},0-20}$ and $R_{\text{CuCu},40-60}$. Bottom: $R_{\text{dAu},40-60}$ and $R_{\text{CuCu},60-94}$	98
6.11	Blue: $R_{\text{dAu},0-20}$, green: $R_{\text{CuCu},0-10}$, red: R_{AuAu}	99
6.12	Average R_{AA} between 1-3 GeV/c in p_T as a function of N_{coll}	100
6.13	Average R_{AA} between 3-5 GeV/c in p_T as a function of N_{coll}	101
6.14	Average R_{AA} between 1-3 GeV/c in p_T as a function of N_{part}	102
6.15	Average R_{AA} between 3-5 GeV/c in p_T as a function of N_{part}	103

6.16	R_{CuCu} for π^0 and e^\pm_{HF}	104
6.17	pQCD calculation of pion suppression in central Au+Au and Cu+Cu	106
6.18	pQCD calculations for D and B meson production	107
6.19	Suppression of heavy-flavor electrons from D and B meson spectra softened by collisional dissociation in central Au+Au collisions	109
6.20	Suppression of D and B production from dissociation and partonic energy loss	111
6.21	R_{AA} for single non-photonic electrons in central Au+Au and Cu+Cu collisions	112
6.22	R_{CuCu} for 0-10% central collisions compared to suppression due to meson dissociation and heavy quark quenching	113
6.23	R_{CuCu} for electrons and muons from heavy flavor	114
6.24	R_{CuCu} for electrons and muons from heavy flavor	115

List of Tables

1.1	N_{coll} values	9
2.1	Summary of PHENIX Detector Subsystems	11
3.1	Electron identification criteria.	32
4.1	meson/ π^0 ratios at high momentum.	63
5.1	The sets of electron ID parameters used to evaluate systematic errors on the acc \times eff correction.	82
5.2	Systematic errors on the inclusive spectrum.	84
A.1	Heavy-flavor $\frac{e^+ + e^-}{2}$ yield, 0-94% MB centrality. Yield and errors in units of $(\text{GeV}/c)^{-2}$, p_T is in units of GeV/c	118
A.2	Heavy-flavor $\frac{e^+ + e^-}{2}$ yield, 0-10% centrality. Yield and errors in units of $(\text{GeV}/c)^{-2}$, p_T is in units of GeV/c	119
A.3	Heavy-flavor $\frac{e^+ + e^-}{2}$ yield, 0-20% centrality. Yield and errors in units of $(\text{GeV}/c)^{-2}$, p_T is in units of GeV/c	120
A.4	Heavy-flavor $\frac{e^+ + e^-}{2}$ yield, 20-40% centrality. Yield and errors in units of $(\text{GeV}/c)^{-2}$, p_T is in units of GeV/c	121
A.5	Heavy-flavor $\frac{e^+ + e^-}{2}$ yield, 40-60% centrality. Yield and errors in units of $(\text{GeV}/c)^{-2}$, p_T is in units of GeV/c	122
A.6	Heavy-flavor $\frac{e^+ + e^-}{2}$ yield, 60-94% centrality. Yield and errors in units of $(\text{GeV}/c)^{-2}$, p_T is in units of GeV/c	123
B.1	R_{CuCu} , 0-94% centrality. The p_T is in units of GeV/c	124
B.2	R_{CuCu} , 0-10% centrality. The p_T is in units of GeV/c	125
B.3	R_{CuCu} , 0-20% centrality. The p_T is in units of GeV/c	126
B.4	R_{CuCu} , 20-40% centrality. The p_T is in units of GeV/c	127
B.5	R_{CuCu} , 40-60% centrality. The p_T is in units of GeV/c	128
B.6	R_{CuCu} , 60-94% centrality. The p_T is in units of GeV/c	129

Acknowledgements

It has been a long journey towards this Ph.D. and I owe my success to many different people.

It has been wonderful to be a part of such a large, diverse group at Stony Brook. I have learned so much from my fellow graduate students and from the assorted faculty and staff. Our weekly group meetings are a great benefit to any student. Being a member of the Relativistic Heavy Ion Group at Stony Brook gave me the opportunity to be a part of the PHENIX collaboration. I had never thought that a large collaboration was for me, but the support and help from so many people has been a big part of my success and I am thankful for every moment.

In my time with the PHENIX VTX group I was lucky enough to work with Chuck Pancake. His vast knowledge on the inner workings of anything electronic taught me more than any class I have taken. I will be forever grateful for his patience and the opportunities that working with him opened up for me.

One of the smartest things I did as a graduate student was to ask Axel Drees to take me on as a student. He has stuck by me through everything with infinite patience. His flexibility to allow me to work on a schedule that accommodated me and my family made my experience at Stony Brook as stress-free as grad school can be. Axel was quick to help with a problem and was always able to lead me on the right course to solving it. Axel has been a great advisor and wonderful mentor.

Finally, I would like to thank my family, without whom none of this would be possible. My parents have supported me, in every way, for my entire life. I would never be where I am without them and I will never be able to thank them enough. I can only hope that being able to brag that their oldest child has a Ph.D. in nuclear physics will be enough. Through all of the teasing about being a perpetual student, my siblings have been nothing but supportive. They have sat through numerous practice talks, read through proposals, and gave me encouragement when I need it. Lastly, I thank my own little family. My sons, Giovanni and Santino, are the reasons I do everything. I hope that I

have shown them that through hard work and dedication they can achieve anything they set out to. Though I am proud to now be Dr.Apadula, Mommy will always be the most important title I carry. To my husband, Felice, who has stood by me through this whole journey with unending support and love, I say thank you. He has been the rock, supporting our family while I pursued my dream, and I hope that one day I can do the same.

Chapter 1

Introduction

1.1 Motivation

The main goal of the Relativistic Heavy Ion Collider (RHIC) is to produce and study the quark-gluon plasma (QGP), a phase of matter postulated to contain asymptotically free quarks and gluons [1]. By colliding gold nuclei at 100 GeV per nucleon, the temperature of the medium produced at RHIC can exceed that of the temperature of the QCD phase transition into the QGP as shown in Figure 1.1. It is now believed that this medium is produced at RHIC as evidenced by the “white” papers of the four experiments at RHIC [2, 3, 4, 5]. The QGP does not behave like a gas as originally thought, but as a “perfect” fluid that flows collectively and can be described by the hydrodynamic equations for a low viscosity fluid.

RHIC was designed to collide various beam species at various energies, including Au+Au to produce the QGP and most recently Cu+Au that provides an additional asymmetry with which to study the medium. These different systems allow for detailed comparisons between different medium effects. In addition to colliding heavy nuclei, RHIC also collides p+p in part to provide a baseline with which to study the properties of the medium. Gold nuclei are also collided with deuteron nuclei to isolate cold nuclear matter (CNM) effects that are difficult to isolate in the hot medium produced in Au+Au collisions. There is a large difference in the system size between the d+Au and Au+Au systems, making some comparisons and conclusions difficult. Colliding Cu nuclei provides an intermediate system size that can serve as a transition between the d+Au and Au+Au systems.

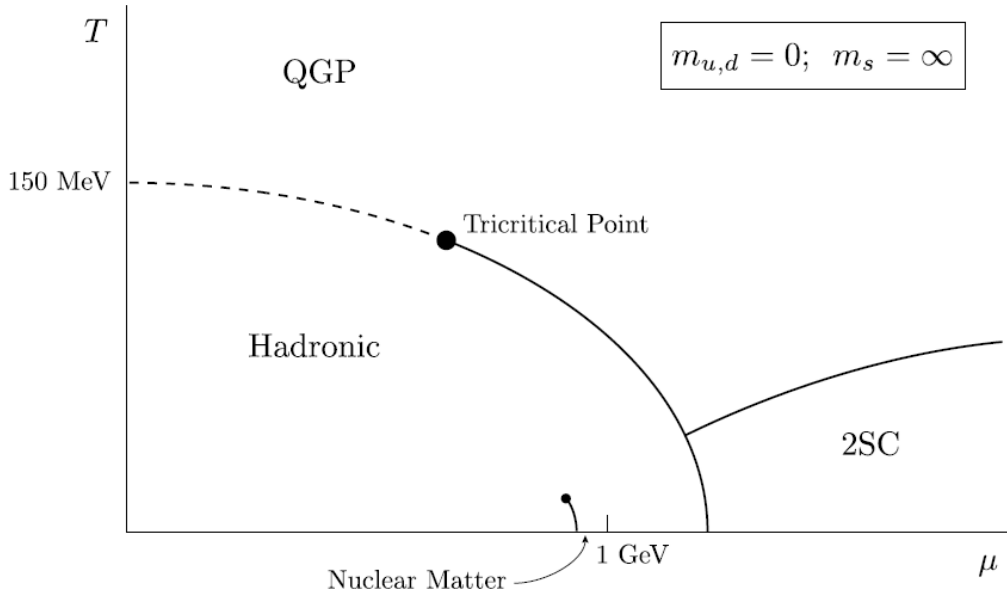


Figure 1.1: Schematic phase diagram of nuclear matter for two massless quarks [3].

Since the medium produced at RHIC is tiny (1000 fm^3) and short-lived ($\sim 10 \text{ fm/c}$) it cannot be studied directly, but through the emerging particles that hit the detectors. One of the many probes used to study the medium are hard probes, particles created through QCD hard scattering that are created in the initial stages of the collision. This thesis focuses on these hard probes, specifically particles that come from heavy quarks (charm and bottom). The masses of the charm and bottom quarks are much larger than the temperature of the medium produced at RHIC so they are created, predominately by gluon-gluon fusion, in the early stages of the collisions. Since they are produced early they experience the full evolution of the medium and any modification to the yield will come from interaction with the medium itself, making them an excellent probe.

As quarks traverse the medium they lose energy and the expectation was that the energy loss would be mainly through radiative processes. Early predictions for this energy loss postulated that heavy quarks would radiate less energy in the medium than the light quarks due to the suppression of small-angle gluon radiation, known as the “dead cone” effect [6]. Previous Au+Au results from RHIC, as will be discussed later, seem to contradict this theory. To reconcile this discrepancy, new theories were developed that include collisional energy loss [7] [8]. However this is insufficient to describe the amount of

suppression seen in Au+Au. More recently, energy loss due to quark fragmentation and meson dissociation were calculated for the heavy-light bound states of the D and B mesons ([9], [10], [11]) and have been found to be successful in describing the data. The dissociation models do not include partonic energy loss and are thus an incomplete picture on their own.

Experimentally, energy loss of heavy quarks would best be measured by observing decays of D and B mesons ($D \rightarrow K \pi$, $B \rightarrow J/\psi K$), but this requires a precise measurement of the displaced decay vertex. The new Vertex (VTX) and Forward Vertex (FVTX) detectors, installed in 2011, have been designed with the ability to directly measure this displaced vertex, but PHENIX did not have this capability during the 2005 RHIC run when the data from this thesis was taken. Alternatively, heavy flavor can be measured more indirectly through the semi-leptonic decay of D and B mesons into electrons or muons, examples are shown in Figure 1.2. This thesis focuses on the measurement of electrons that come from the decays of open heavy flavor hadrons, i.e. hadrons with one heavy quark and the rest light quarks. The yield of these “non-photonic” electrons scales with the number of binary collisions N_{coll} [12], as shown in Figure 1.3, just like a hard process, confirming that they likely come from heavy flavor. The open heavy flavor hadrons decay after the dispersion of the medium and thus the modification to the electron spectra reflects the modification to the mesons and not a modification of the decay kinematics.

1.2 Heavy Flavor at RHIC

Electrons from heavy flavor have been previously been analyzed for p+p, Au+Au and d+Au at RHIC. Heavy quark production in p+p collisions agrees well with fixed-order plus next-to-leading-logarithm (FONLL) pQCD calculations [13], [14], serving as a testing ground for QCD, while also functioning as a well understood baseline for studying medium effects in heavy ion collisions. In the absence of any medium modification we would expect the differential yield in p_T from heavy ion collisions to be the same as the differential yield in p+p scaled by the number of binary collisions, N_{coll} . The nuclear modification factor, R_{AA} , is used to quantify nuclear effects on particle production and is defined as:

$$R_{\text{AA}} = \frac{dN_{\text{AA}}}{\langle N_{\text{coll}} \rangle \times dN_{\text{pp}}} \quad (1.1)$$

where $dN_{\text{AA}}(dN_{\text{pp}})$ is the differential yield in heavy ion (p+p) collisions. An R_{AA} value of one would mean no modification from the medium. Since the

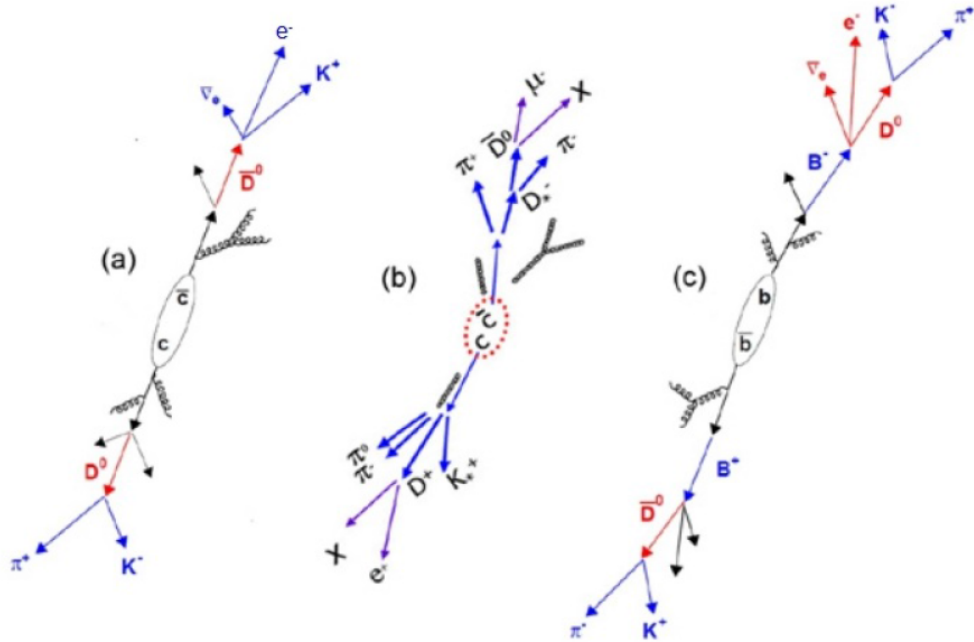


Figure 1.2: Some decay diagrams.

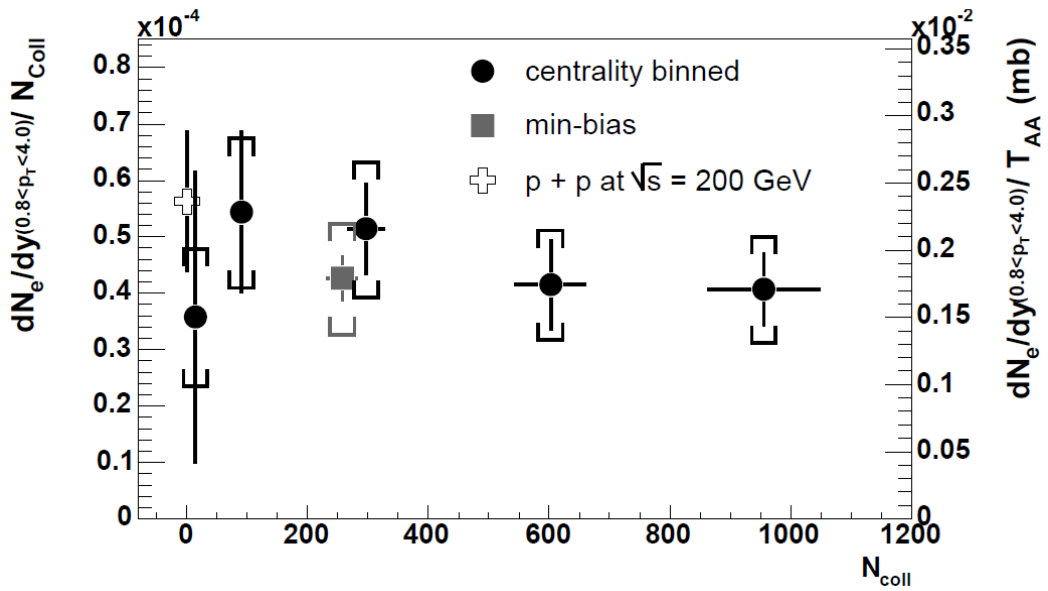


Figure 1.3: Non-photonic electron yield in $\sqrt{s_{\text{NN}}}=200 \text{ GeV}$ Au+Au collisions scaled by the number of binary collisions N_{coll} [12].

QGP is most likely to be formed in head-on collisions, R_{AA} is measured in bins corresponding to how head-on the collision is, defined as centrality. The smaller the impact parameter, b , the distance between the centers of the two colliding nuclei, the more central an event. A peripheral event would be characterized by the two nuclei barely grazing each other. The number of participants, N_{part} , in a peripheral event is small, closer to the two participants in a p+p event. N_{coll} and N_{part} increase as centrality increases.

The first measurement of single electrons from Au+Au were made at $\sqrt{s} = 130 \text{ GeV}$ [15]. The data from the 2002 $\sqrt{s} = 200 \text{ GeV}$, shown in Figure 1.3, showed that the total cross section of the non-photonic electrons scales with the number of binary collisions as is expected from a hard process [12]. In 2004, the R_{AuAu} of non-photonic electrons was plotted as a function of p_T and found to have significant suppression in the most central bin [16]. The suppression is on the same level as the neutral pions in central Au+Au collisions [17], in contradiction to the expectation due to “dead cone” effect. The top (yellow) band in Figure 1.4 shows the DGLV prediction for radiative energy loss for electrons from D and B decays [18], which under predicts the level of suppression seen in the data. However, if only the D meson is taken into account, as shown in the thin dashed lines, the prediction agrees within uncertainties. Charm is the dominate contribution to the non-photonic electron yield at low p_T , and though we know the charm and bottom contributions are about equal at 5 GeV in p+p, it is unknown in Au+Au. If the charm does lose more energy than bottom, the charm will shift to lower p_T and the bottom will dominate sooner. Whether or not this is the case, the addition of the B meson suppression in 1.4 is not enough to account for the large suppression in the electron yield.

A full understanding of these effects requires measurements of initial state effects inherent to nuclear collisions. These initial state effects are present in Au+Au collisions but are difficult to distinguish from the effects of the hot medium. The parton distribution functions (PDFs) inside the nucleus are significantly modified compared to free protons and neutrons and so there can also be modification to processes which originate from partonic interactions [19]. Partons can also have a broadened transverse momentum spectrum due to collisions inside the nucleus [20], or lose energy in the nuclear medium in the initial stages of the collision [21]. These effects may introduce cold nuclear matter (CNM) effects on the observed yield. These CNM effects include the Cronin Effect [22], CNM energy loss [21], and dynamical shadowing [23], [24], [25], [26]. To study these CNM effects electrons from open heavy flavor were measured in the 2008 $\sqrt{s} = 200 \text{ GeV}$ d+Au collisions, where no medium is

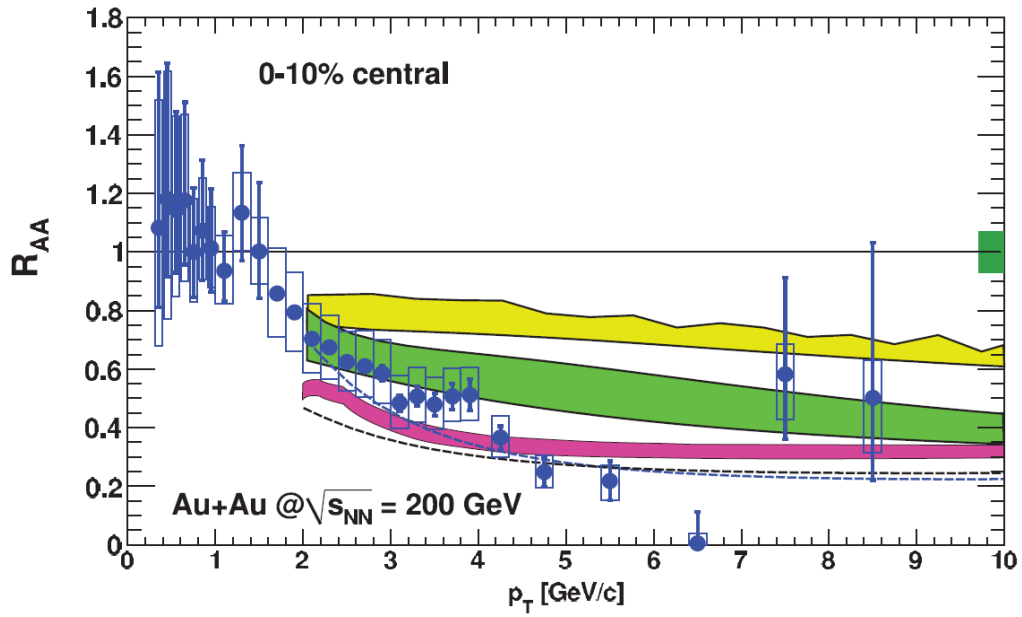


Figure 1.4: Open heavy-flavor electron R_{AA} for the most central bin compared with various models. The upper two bands are DGLV [18] calculations for electrons from D and B decays. The upper band is radiative energy loss only and the middle band includes both radiative and collisional energy loss. The lower band is from a collisional dissociation model [9]. The thin dashed lines are from DGLV calculations for D decays only.

expected to form and therefore any modification from the p+p shape will be from the particle production in the nucleus. The d+Au results show no suppression in any centrality bin and in fact show a significant enhancement, larger than that of the pions and kaons [27], an example is shown in Figure 1.5. The enhancement could be caused by parton scattering in the nucleus, though any effect on heavy flavor production could also modify the spectra.

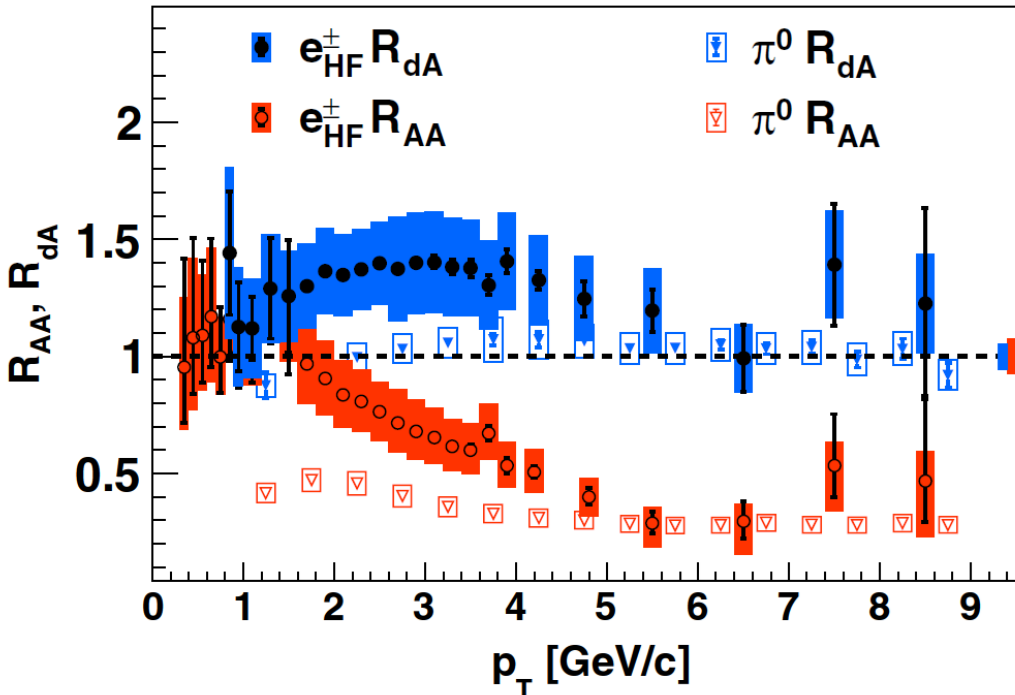


Figure 1.5: The nuclear modification factors R_{dA} and R_{AA} for minimum bias d+Au and Au+Au collisions, for the π^0 and e_{HF}^{\pm} [28].

Figure 1.5 also shows the differences in the R_{dA} between the light and heavy flavor hadrons. This difference indicates that the initial state effects on the light and heavy quarks are quite different and may contribute to the differences in the light and heavy flavor R_{AA} at moderate p_{T} . Recently fragmentation and dissociation have been suggested as an energy loss mechanism for heavy flavor mesons [29],[30],[31]. The hadron formation time is inversely proportional to the mass of the hadron, $\tau_{\text{form}} \propto 1/m_h^2$. If we take $\tau_{\text{form}} \sim 0.6 \text{ fm}$, the small mass of the pion ensures that the parent light quarks and gluons will fragment outside of the QGP, as per the traditional picture of jet quenching. However, the large masses of the D and B mesons implies that charm and bottom will fragment inside the medium, with the effect extending farther in p_{T} for the B

meson. There is likely a competition between heavy meson dissociation and charm and bottom decay in the medium that leads to the level of suppression measured in Au+Au.

The opposing effects of cold nuclear matter enhancement and hot nuclear matter suppression form an interplay of competing effects that seem to depend on system size. The average number of binary collisions, N_{coll} , is vastly different between d+Au and Au+Au collisions (7.59 and 257.8 respectively). To further understand these phenomena, RHIC collided Cu nuclei at the same center of mass energy per nucleon in 2005. The N_{coll} spread of the Cu+Cu collisions spans the gap between the d+Au and Au+Au systems, as illustrated by the cartoon in Figure 1.6 and shown in Table 1.1. Peripheral Cu+Cu collisions have a similar N_{coll} to mid-central d+Au, while the central Cu+Cu collisions are similar to semi-peripheral Au+Au. The centrality dependence in this intermediately-sized system allows for a detailed examination of the competition between differing effects.

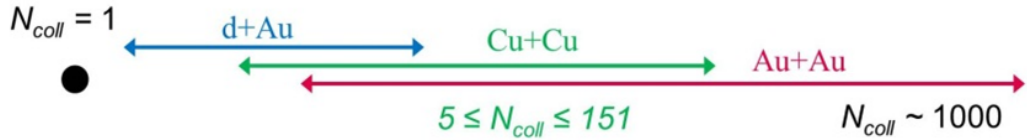


Figure 1.6: Cartoon showing the N_{coll} range of the d+Au, Cu+Cu and Au+Au systems. Cu+Cu provides the bridge to tie the d+Au and Au+Au results together.

In this thesis the analysis of the medium modification of the yield of electrons from the decay of open heavy flavor in Cu+Cu collisions at $\sqrt{s}=200 \text{ GeV}$ will be detailed. Chapter 2 presents an overview of the PHENIX detector system related to this analysis. Chapters 3 and 4 present the details of the data analysis and the background subtraction, respectively. Chapter 5 details the systematic errors in the analysis. Chapter 6 shows the analysis results, including the nuclear modification factor, and makes comparisons with previously measured PHENIX data and various theoretical predictions. Finally, Chapter 7 gives a brief summary.

Table 1.1: N_{coll} values for d+Au[32], Cu+Cu[33], and Au+Au[34] collisions.

Colliding Species	Centrality	N_{coll}
d+Au	0-100%	7.59 ± 0.43
	0-20%	15.06 ± 1.01
	20-40%	10.25 ± 0.70
	40-60%	6.58 ± 0.44
	60-88%	3.20 ± 0.19
Cu+Cu	0-94%	51.8 ± 5.6
	0-10%	182.7 ± 20.7
	0-20%	151.8 ± 17.1
	20-40%	61.2 ± 6.6
	40-60%	22.3 ± 2.9
	60-94%	5.1 ± 0.7
Au+Au	0-93%	257.8 ± 25.4
	0-10%	955.4 ± 93.6
	10-20%	602.6 ± 59.3
	20-40%	296.8 ± 31.1
	40-60%	90.70 ± 11.8
	60-93%	14.50 ± 4.00

Chapter 2

PHENIX Experiment

2.1 PHENIX Detector Overview

RHIC was designed to collide a large variety of beams, such as different types of Heavy Ions, and polarized protons. In order to study the source of certain effects, one would also want to collide protons with Heavy Ions. Unfortunately, this is not possible without significant modifications to the beamline magnets, because protons and Heavy Ions have different magnetic rigidities. As a compromise, we have chosen deuteron-gold collisions instead. In the future, a dedicated RHIC Run is planned which will allow collisions of protons with Heavy Ions. To study the properties of these collisions a variety of probes, including leptons (electrons and muons), photons and hadrons, need to be measured with excellent momentum and energy resolution. To that order the Pioneering High Energy Nuclear Interaction eXperiment (PHENIX) was designed and built to meet these needs.

The PHENIX detector includes global detectors to determine collisional properties, two central arm spectrometers at mid-rapidity to measure electrons, photons and hadrons and two muon arms at forward and backward rapidity for the measurement of muons. Figures 2.1 and 2.2 show a cartoon representation of the PHENIX detector in the 2005 RHIC run. The beam view of the detector, Figure 2.1, shows the central arm spectrometers. The side view is shown in Figure 2.2 with a view of the global detectors and the muon arm spectrometers. This analysis uses a subset of the individual PHENIX detectors. The global Beam-Beam Counters (BBC) and Zero-Degree Calorimeters (ZDC) are used as a base trigger and for centrality determination. Since this analysis studies electrons at mid-rapidity, only the central arm spectrometers

are used. In particular the Drift Chamber (DC) and Pad Chamber (PC) for charged tracking and the Electromagnetic Calorimeter (EMCal) and Ring-Imaging Cherenkov Detector (RICH) for electron identification. Table 2.1 [35] shows an overview of each detector, including their $\Delta\eta$ and $\Delta\phi$ range. Each detector will be discussed in detail in the following sections.

Detector	$\Delta\eta$	$\Delta\phi$	Features
Magnet: central(CM) muon south muon north	± 0.35	360°	Up to 1.15 Tm
	-1.1 to -2.2	360°	0.72 Tm for $\eta = 2$
	1.1 to 2.4	360°	0.72 Tm for $\eta = 2$
BBC ZDC	$\pm(3.1 \text{ to } 3.9)$ $\pm 2 \text{ mrad}$	360° 360°	Start timing, fast vertex Minimum bias trigger
DC PC TEC	± 0.35	$90^\circ \times 2$ $90^\circ \times 2$ 90°	Good momentum and mass resolution, $\delta m/m = 0.4\%$ at $m = 1 \text{ GeV}$. Pattern recognition, tracking for non-bend direction Pattern recognition, dE/dx
RICH ToF EMCal: PbSc PbGl	± 0.35 ± 0.35 ± 0.35 ± 0.35	$90^\circ \times 2$ 45° $90^\circ + 45^\circ$ 45°	Electron identification Good hadron identification, $\sigma < 100 \text{ ps}$ Photon and electron detection Good e^\pm/π^\pm separation at $p > 1 \text{ GeV}/c$ by EM shower and $p < 0.35 \text{ GeV}/c$ by ToF. K^\pm/π^\pm separation up to $1 \text{ GeV}/c$ by ToF
μ tracker south north μ identifier: south north	-1.15 to -2.25 1.15 to 2.44 -1.15 to -2.25 1.15 to 2.44	360° 360° 360° 360°	Tracking for muons Steel absorbers and Iarocci tubes for muon/hadron separation

Table 2.1: Summary of PHENIX Detector Subsystems [35].

2.2 Global Detectors

2.2.1 Beam-Beam Counter

The PHENIX Beam-Beam Counters (BBC) are used to provide an initial collision time for timing detectors, as a data trigger, to determine the collision vertex point on the z-axis(beam axis) and, along with the ZDC, to determine centrality. They are placed at $\pm 1.44 \text{ m}$ along the beam pipe from the center of

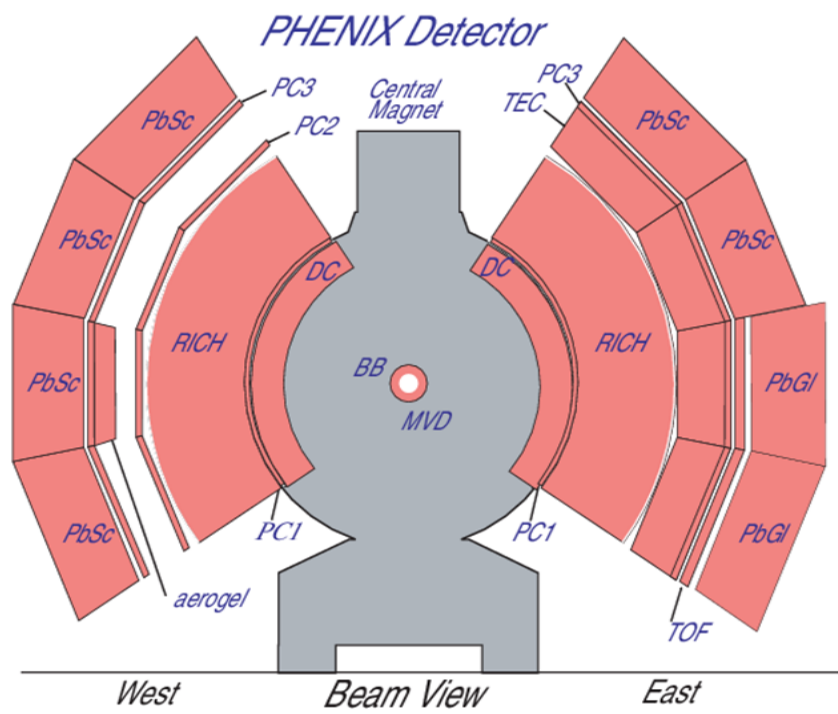


Figure 2.1: PHENIX detector in the 2004 RHIC run, same as the 2005 run with the exception of the MVD. Beam view, looking down the north going beam direction.

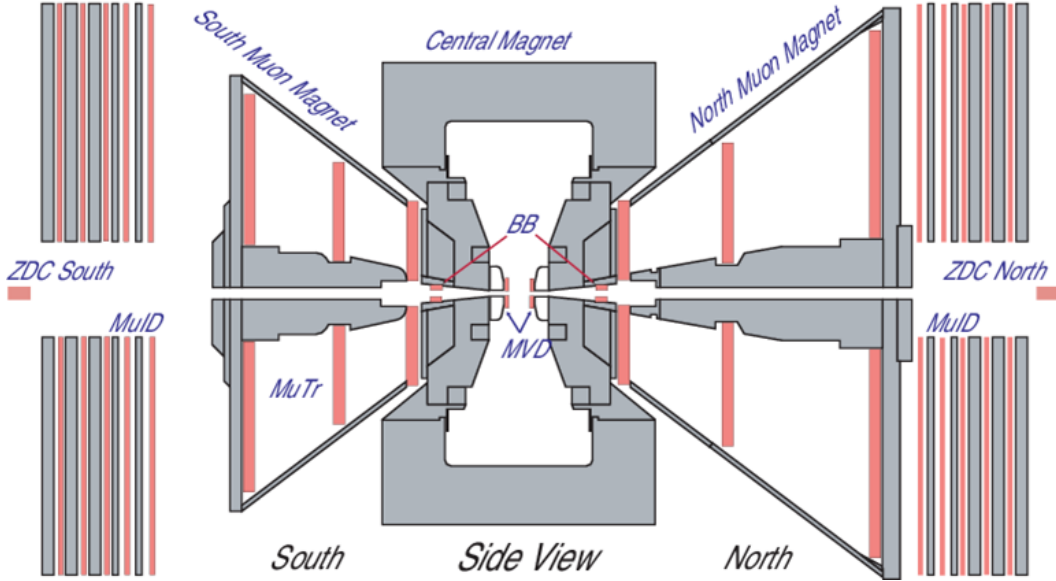


Figure 2.2: PHENIX detector in the 2004 RHIC run, same as the 2005 run with the exception of the MVD. Side view, looking at the West side of the detector.

the PHENIX detector (north and south) and their η and ϕ coverage are shown in Table 2.1. The BBC are made up of 64 photomultiplier tubes (PMTs) arranged in three rings from an inner radius of 5 cm outward to 30 cm and are mounted on a Čerenkov radiating quartz, which serves as the entrance window to the PMT. Figure 2.3 shows a schematic of the BBC. The BBCs have a large dynamic range capable of measuring between 1 and 30 minimum ionizing particles (MIP) in each PMT and are thus able to be used in all collisional systems at PHENIX. The timing resolution of the BBC is 50 ps and the t_0 is found by taking the average time measured by each PMT in the north and averaged with the same measurement in the south. The difference in average time between the north and the south BBCs,

$$Z_{\text{vtx}}^{\text{BBC}} = \frac{(t_{\text{BBCN}} - t_{\text{BBCS}})}{2c}, \quad (2.1)$$

determines the z-vertex (ZVTX) position along the beam axis. This allows the detector to be used for a “minimum bias” trigger. The “minimum bias” trigger requires a hit in at least one PMT in both the north and south BBC and the vertex position to be within 50 cm of PHENIX center. In the Cu+Cu collisions the BBC Level-1 minimum bias trigger has an efficiency of $94\% \pm 2\%$.

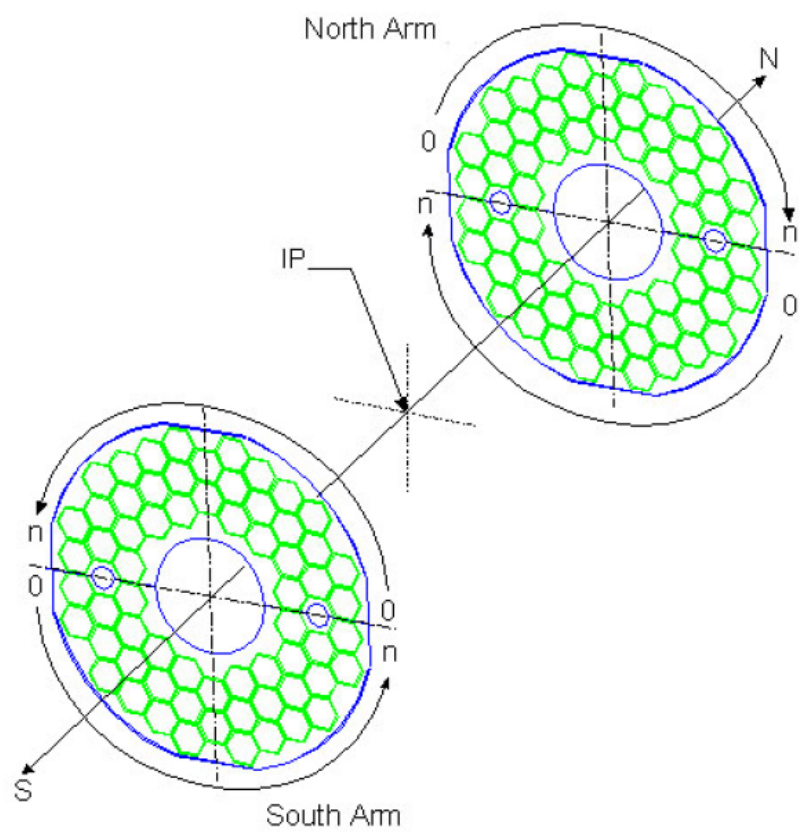


Figure 2.3: Schematic view of the BBC.

The charge measured in the BBC is used to determine centrality. An example is shown in Figure 2.4. The charge in the BBC increases with charged particle multiplicity and is maximum in the most central collisions. Centrality is determined in five percent bins, where each bin has the same number of events. Head-on collisions would have a centrality of 0-5% and peripheral collisions have a centrality closer to 100%.

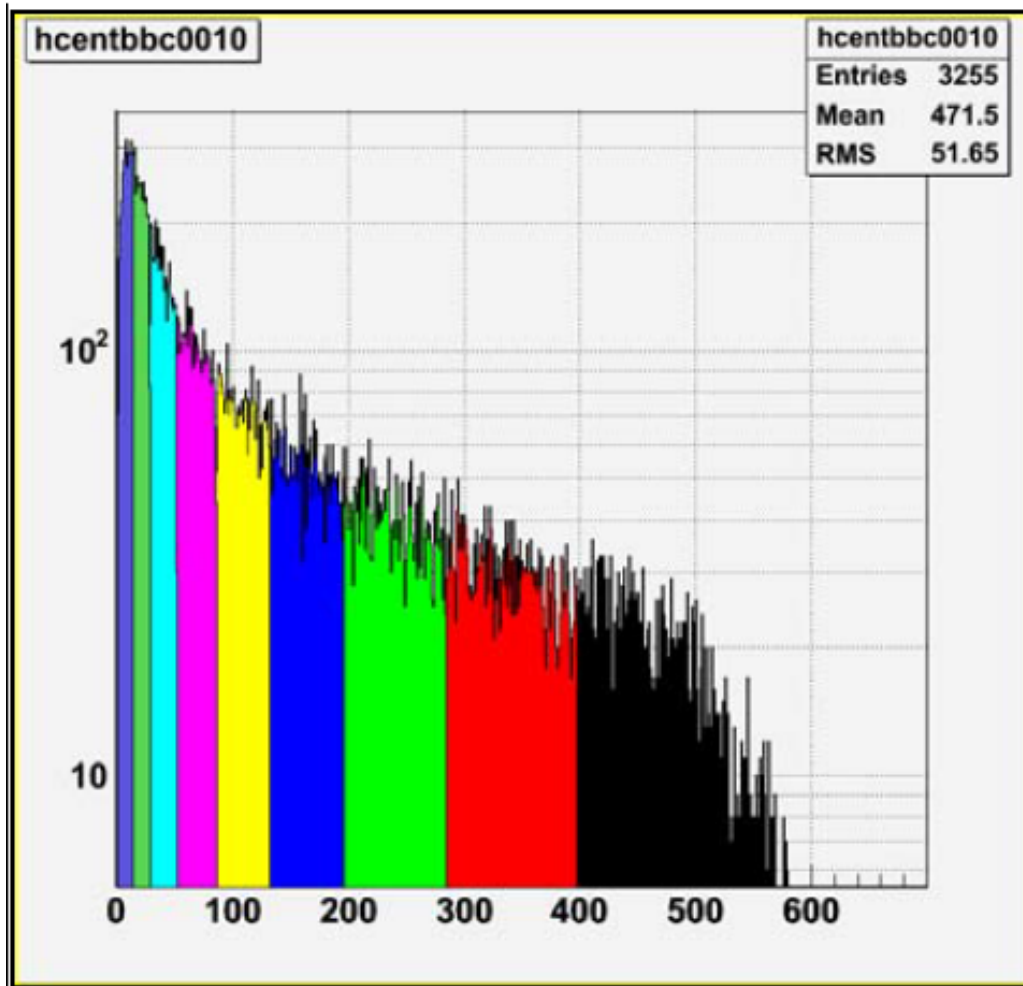


Figure 2.4: BBC Charge North+South Distribution for minimum bias events.

2.3 Central Arm

2.3.1 Magnet

The PHENIX magnet system is comprised of three magnets, a Central Magnet (CM) and two Muon Magnets (MMN and MMS). This analysis is done at mid-rapidity and we therefore focus on the CM. The CM is an axial field magnet that is energized by two pairs of concentric coils that can be run in three configurations, “++”, “- -” and “+ -”. It was designed so there is no material before the central spectrometers, which eliminates additional scatterings, and dense material before the muon spectrometers to serve as hadron absorbers. It covers ± 0.35 units of rapidity and the field integral for a track in the “++” field is 1.15 Tm near the beam axis. The field is minimal at the radius of the Drift Chamber (DC) and beyond for tracking that assumes straight tracks. In the 2005 Cu+Cu runs the field was run in both “NORMAL” (“++”) and “REVERSED” (“- -”) field configurations. Figure 2.5 shows the field lines in the “++” field.

2.3.2 Drift Chamber

The Drift Chambers (DC) are located in both arms and are the main tracking detectors in PHENIX. They are located between 2.02 and 2.46 m in the radial direction and the acceptance is as follows:

- 90° in ϕ
- ± 90 cm in Z
- $\pm |0.35|$ in η

The main objectives of the DC are to precisely measure the charged particle momentum and provide charged particle tracking in conjunction with the other central arm detectors. In order to satisfy these objectives the DC need to meet the following requirements [36]:

- Single wire spatial resolution better than 0.15 mm
- Single wire two track separation better than 1.5 mm
- Spatial resolution better than 2 mm in Z direction

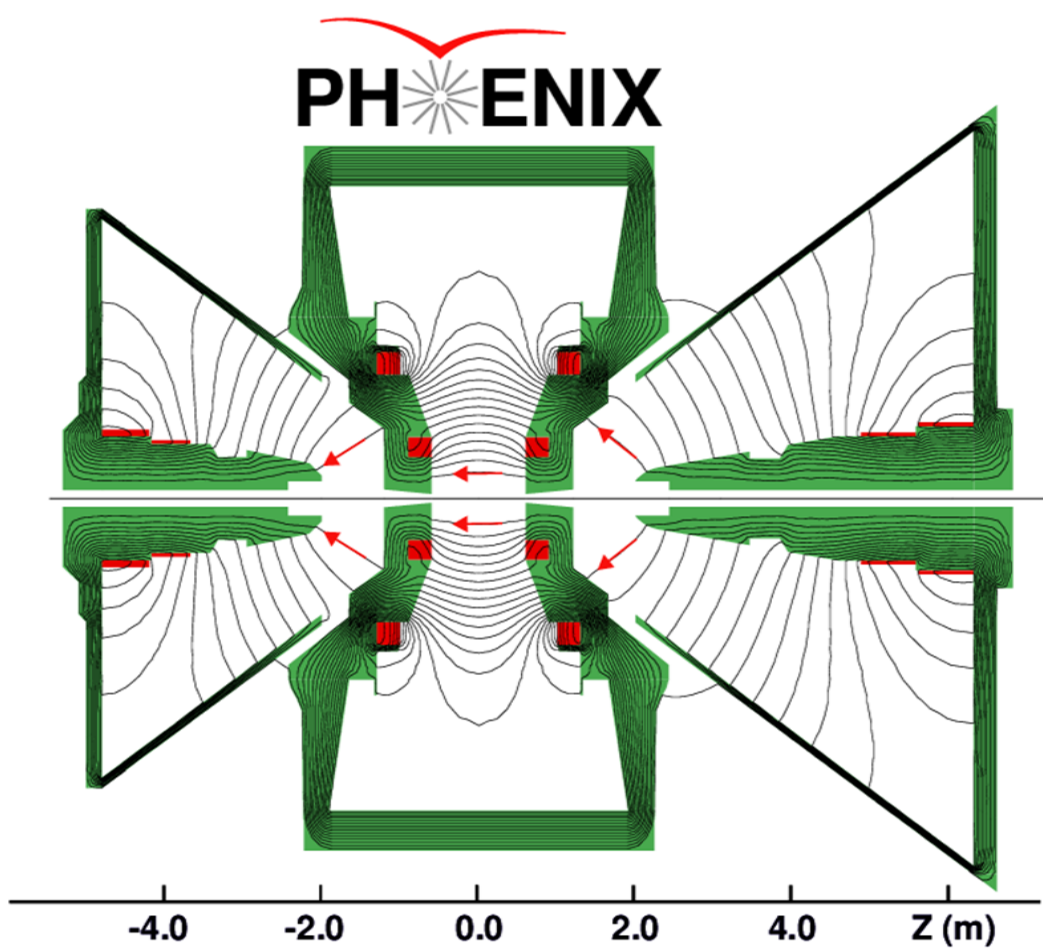


Figure 2.5: Magnetic field lines for the two central magnet coils in combined (++) field mode.

- Single wire efficiency better than 95%.

The DC consists of two identical arms in the east and west. Figure 2.6 shows the titanium framework of a DC arm. They are each filled with a gas mixture made up of 50% Ar and 50% C_2H_6 . This mixture was chosen to provide a uniform drift, high gain, and a low diffusion coefficient. The DC measures the drift time of the electrons that are ionized by a charged particle traversing the gas. Since the gas mixture was chosen to have a uniform drift velocity the drift time can be translated linearly into a distance. Each arm is made up of 20 equal sectors called keystones, each covering 4.5° in ϕ . A keystone has 6 wire modules named X1, U1, V1, X2, U2, and V2 that consist of 4 anode and 4 cathode wire nets apiece. The X1 and X2 wire modules run parallel to the beam axis and are used to measure the ϕ component of the track. The U1, V1, U2 and V2 wire modules are rotated with respect to the X wire modules to measure the z component of the track. The configuration of the wire modules can be seen in Figure 2.7.

There are twelve anode wires per anode net in the X wire modules, while the UV wire modules have four. This combination gives each sector 40 drift cells. The layout of the wires in each sector is shown in Figure 2.7. UV wires begin in one sector and end in a neighboring sector on the opposite side of the DC.

The anode wire nets contain other wires besides the anode(sense) wires as shown in Figure 2.7. Potential wires create a high field which helps to separate neighboring sense wires and control the gas gain. Gate wires also create a high field which limits the drift length of the track to about 3 mm and reduces the detector occupancy. Termination wires reduce boundary effects and help maintain uniform gas gain. Finally, the back wires have a low potential which blocks the drift from one side of the anode wire. This eliminates the left-right ambiguity and reduces the tracks seen by one anode wire, even wires will collect from one side while odd wires collect from the other. The anode wires are separated into two halves, each of which are read out independently, for efficient track recognition up to 500 tracks. The two halves are electrically isolated by a low mass central support made of $100\mu m$ thick kapton. The approximately 6500 DC anode wires correspond to about 13,000 total readout channels.

Hits in the X1 and X2 planes are combined into tracks using a combinatorial Hough transform [37]. The tracking assumes that the charged track is straight in the DC detector region, where the PHENIX magnetic field is minimal. Figure 2.8 shows the definition of the two coordinates that are used to describe

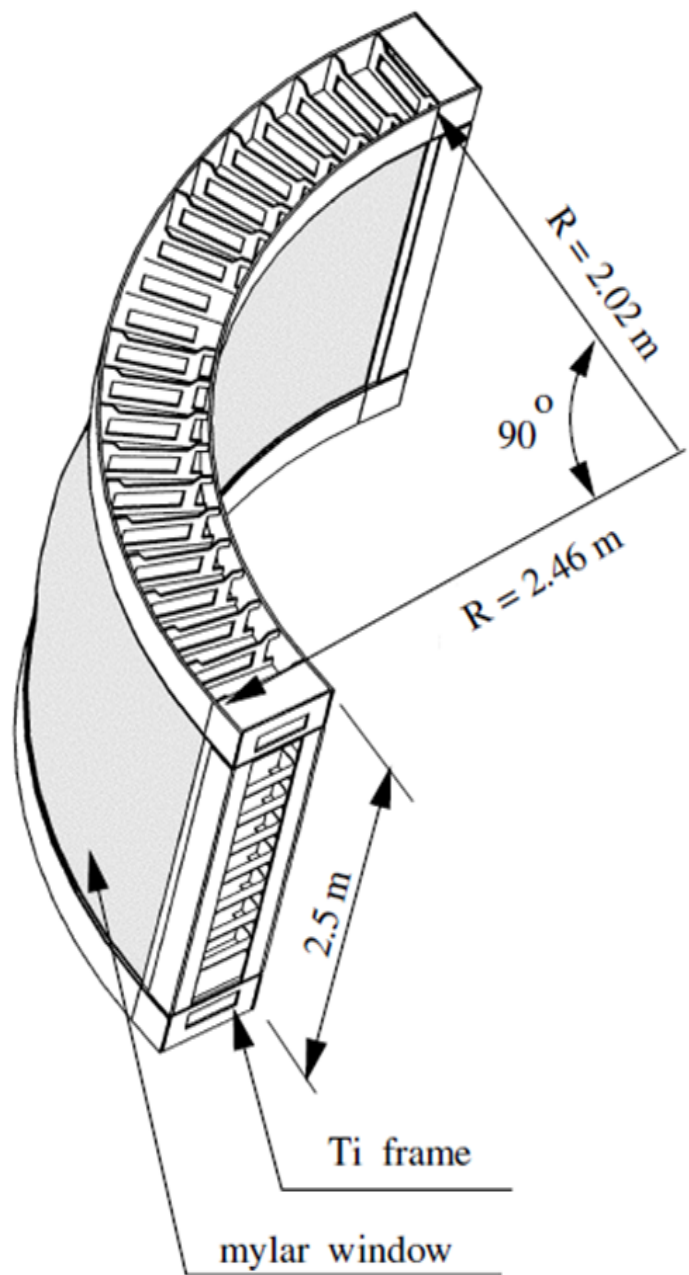


Figure 2.6: DC frame.

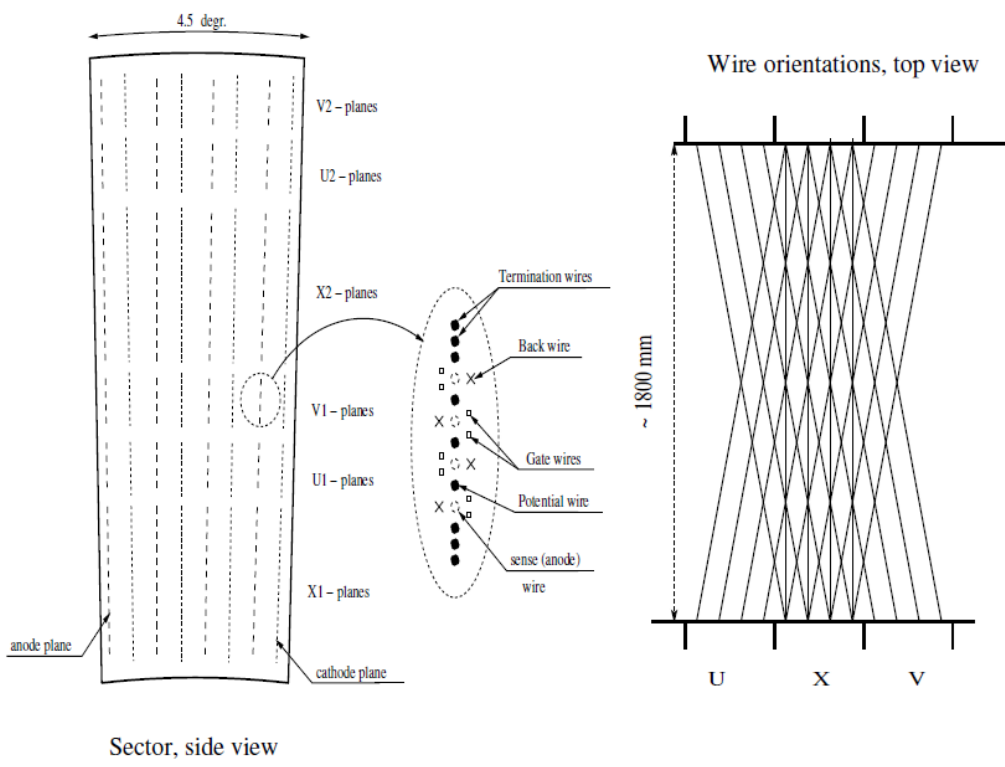


Figure 2.7: Left: Layout of wire position in one sector and anode net configuration. Right: Top view of UV wire orientation.

the tracks in the DC, ϕ and α . The polar angle at the intersection of the track with the reference radius (near the middle of the DC) is ϕ and α is the inclination of the track. Using these coordinates can directly map to other variables because the momentum of the particle can be determined, as a first order approximation, from alpha:

$$p = \frac{\text{constant}}{\alpha}. \quad (2.2)$$

The Hough transform calculates ϕ and α for all possible combination of hits, with the requirement that there be hits in both X1 and X2, and puts them into an array. These are then considered good track candidates and the next step is to remove background tracks. First is to determine whether a hit in the DC is associated with a track. In an iterative procedure, hits are weighted according to how far they are from the straight track guess. The weighting drops to zero far from the track so random noise does not affect the fit. Each hit can correspond to only one track and so the track closest to each hit is kept and the hit is removed from any other track candidates. Using these requirements, in a standard Au+Au environment, 98% of the tracks from the origin that pass completely through the DC are found. The falsely reconstructed, or “ghost”, track rate is less than 1 %.

Since the X layers do not give z information, the tracking as it stands described above will only give information in the $r\text{-}\phi$ plane. The z information is found from the vertex position determined by the BBC and from the PC1. The z position of a hit in PC1 that is associated with the track projection from the DC gives the z position of the track. If there is more than one associated PC1 hit then the UV sections of the DC are used to determine the appropriate PC1 hit.

2.3.3 Pad Chamber

PHENIX has three layers of multiwire proportional chambers called the pad chambers (PC) shown in Figure 2.9. The first layer, PC1, is in both arms located between the DC and the RICH. PC3 is also in both arms, located in front of the EMCAL. PC2 is in the west arm only, located behind the RICH. Each PC is composed of a single plane of wires inside a gas volume that is bound by two cathode planes, one of which is finely segmented into an array of pixels that determines space points in a straight line trajectory. The PC are essential for particle identification, particularly for the electrons in this analysis. The DC and the PC1 determine the three-dimensional momentum

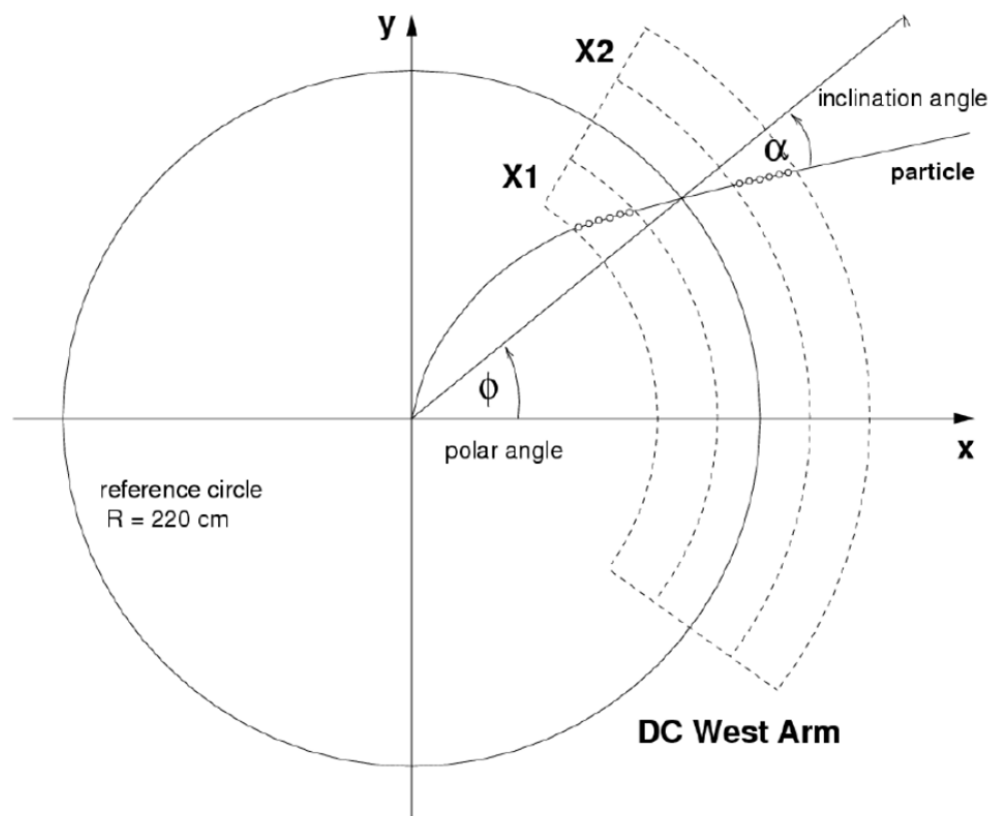


Figure 2.8: A sample track with the Hough Transform parameters.

vector and provide information that gives direction vectors through the RICH, essential for electron identification.

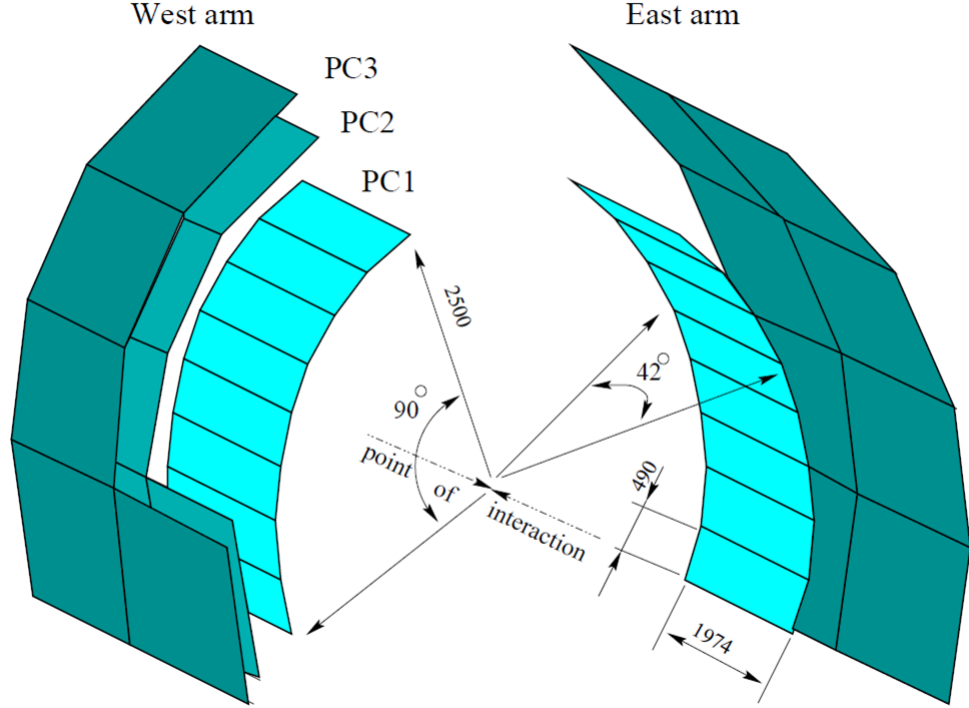


Figure 2.9: Schematic of the placement of the PC.

2.3.4 Ring-Imaging Cherenkov Detector

The Ring Imaging Cherenkov (RICH) detectors are located in each of the PHENIX central arms. As its name implies, the RICH detects Čerenkov(Cherenkov) light. If a charged particle's speed exceeds the speed of light in a medium ($\beta > 1/n$) it will emit Čerenkov light. The emission angle of the light is

$$\cos \theta_c = \frac{1}{\beta n}, \quad (2.3)$$

and is illustrated in Figure 2.10. If the momentum of the particle is known it can be identified using the Čerenkov light measurements.

The RICH detectors, using CO_2 radiator gas, provide e/π discrimination to better than 1 part in 10^4 below 4.7 GeV/c, the π Čerenkov threshold, for

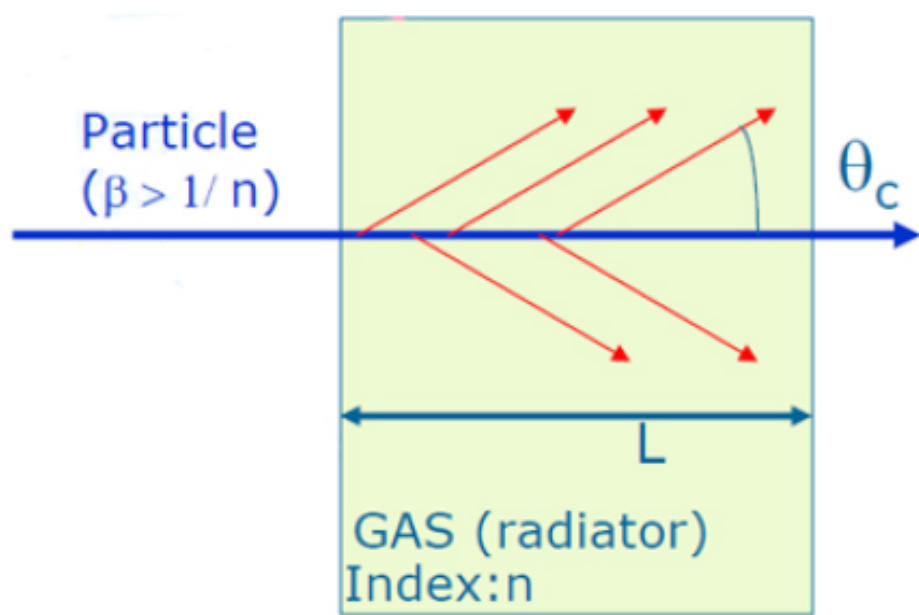


Figure 2.10: Cartoon of Čerenkov radiation.

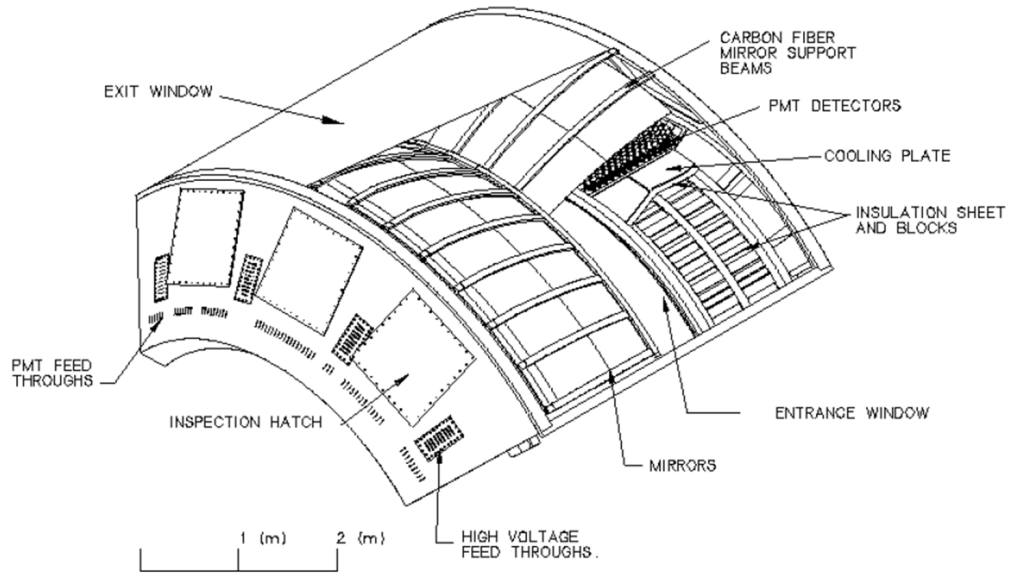
p+p collisions. Figure 2.11 shows a cutaway view of one of the RICH detectors along with a side-view schematic . The RICH detectors have a volume of 40 m^3 , an entrance window area of 8.9 m^2 , and an exit window area of 21.6 m^2 in each arm. They each have 48 composite mirror panels that form two intersecting spherical surfaces, with a total reflecting area of 20 m^2 . Two sets of photomultiplier tubes (PMT) on either side of the RICH entrance windows (2560 in each arm) collect the Cerenkov light focused by the mirrors. Photons with wavelengths below 200 nm are absorbed by the phototube glass windows. At 200 nm the reflectivity of the mirrors is 83%, rising to 90% at 250 nm. In addition to being used for electron identification the RICH is also used with the EMCAL as an electron trigger.

2.3.5 Electromagnetic Calorimeter

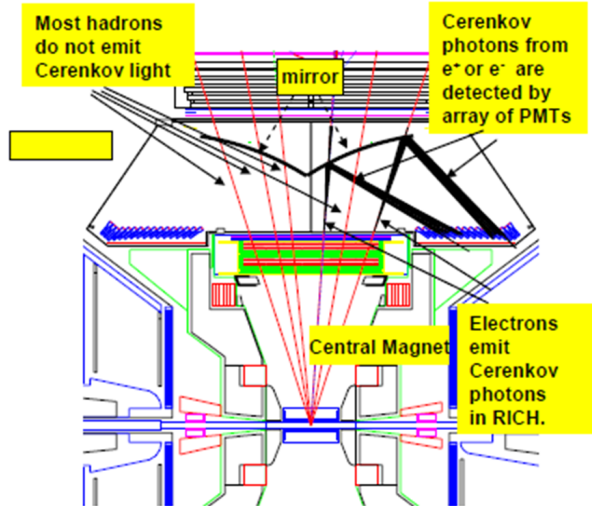
The main goal of the Electromagnetic Calorimeter (EMCal) is to provide energy and position measurements of photons and electrons produced in the collisions at RHIC. It is also used in particle identification and in the PHENIX trigger system. The EMCal is made up of two different calorimeters, the Pb-Scintillator (PbSc) and the Pb-Glass (PbGl) which together cover the full central arm acceptance in PHENIX. The PbSc is made up of six sectors, four in the west arm and two in the east arm, and two PbGl sectors make up the rest of the east arm. The two detectors have different strengths and give different systematics, thus increasing the confidence level of the physics results.

The EMCal absorbs the measured particles energy. The energy resolution of the calorimeter increases as a function of the particle energy because it exploits the particle multiplication process known as showering. Electromagnetic showers, specifically from electrons, shower because of bremsstrahlung. An electron will bremsstrahl photons until the critical energy, where ionizational energy loss brings it to rest. The photons will then convert and the electron-positron pairs will repeat the process until all the energy is absorbed. Greater incident energy gives a greater number of particles and therefore a better energy resolution.

The PbSc is a shashlik type sampling calorimeter with alternating tiles of Pb and scintillator that consists of 15552 individual towers, with dimensions $5.25 \times 5.25 \times 37.0\text{ cm}^3$. Four of these towers make up a module, each of which is read out individually. The interior view of one of these modules is shown in the top portion of Figure 2.12. Thirty-six modules are attached together to form a structure called a supermodule and eighteen supermodules make a sector. The PbSc excels in timing and has a timing resolution of $\sim 400\text{ ps}$ for



(a)



(b)

Figure 2.11: Top (a): A cutaway view of one arm of the RICH. Bottom (b): Schematic of the RICH.

electromagnetic showers and an energy resolution of $8.1\%/\sqrt{E}(\text{GeV}) \oplus 2.1\%$ [38]. The PbGl is composed of 9216 elements that were previously used in the WA98 [39] experiment at CERN. A PbGl supermodule is shown in the bottom half of Figure 2.12. Energy measurements are better with the PbGl, with a nominal energy resolution of $5.95\%/\sqrt{E}(\text{GeV}) \oplus 0.76\%$ and an intrinsic timing resolution of $\sim 500\text{ ps}$ [38].

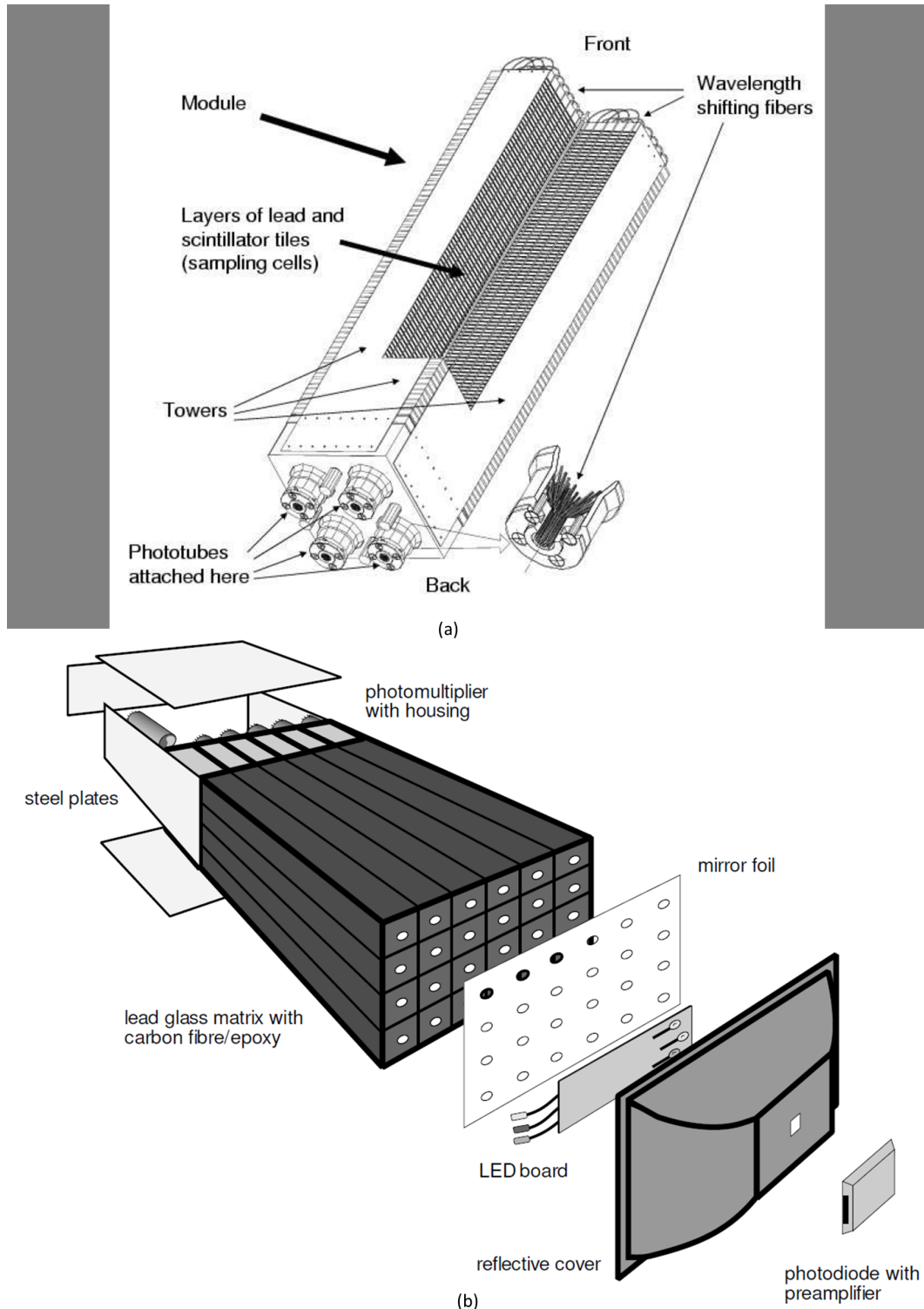


Figure 2.12: Top (a): Interior view of the PbSc module. Bottom (b): Exploded view of a PbGl supermodule [38].

Chapter 3

Data Analysis

The first step to understanding medium effects, using the nuclear modification factor for the single electron spectrum, is determining the inclusive invariant electron spectrum. First we determine the yield of all electrons (this chapter) and then, using different background subtraction techniques (see Chapter 4), we isolate the heavy flavor electrons from the inclusive yield (see Chapter 6).

3.1 Event Selection

This analysis uses two different event selection techniques. The first is a minimum-bias (MB) trigger which fires when there is at least one PMT fired in each BBC (north and south). The z-vertex position is required to be between ± 20 cm of the collision vertex. The MB data set provides good statistics at low momentum, but the statistics run out as momentum increases. To combat the low statistics a triggered data set is used. The EMCal-RICH trigger (ERT) is an electron trigger that uses a coincidence between the EMCal and RICH detectors that were described in the previous section. The EMCal is fired when the energy deposited is greater than the threshold set by the trigger. This creates a turn on curve and since there are enough statistics in the MB, the ERT trigger is used starting at $p_T = 3$ GeV, well beyond the trigger turn on curve ($p_T \sim 1.2$ GeV). In the 2005 Cu+Cu runs the ERT trigger conditions were as follows:

- *Runs 150474- 157419:* EMCal threshold - 1.08 GeV, RICH - 3 p.e.

- *Runs 157419 - end:* EMCAL threshold - 800 MeV, RICH - 3 p.e.

Centrality is determined with the clock method described in the previous section. The centrality classes used in this analysis are 0-10%, 0-20%, 20-40%, 40-60% and 60-94%. These are in addition to a minimum bias (MB) centrality that corresponds to 0-94%. This MB is not to be confused with the MB trigger data sample described above.

3.2 Electron Track Selection

Electrons are selected from a set of charged tracks that are determined to be electrons by passing a set of identification cuts. These electron candidates must also pass fiducial cuts that require them to be within a certain portion of the detector that is well understood and functioning properly.

3.2.1 Electron Identification

Table 3.1 outlines the cuts used in this analysis. Electron candidates start with charged tracks identified by the DC and PC and are given a quality determination based on which X sectors in the DC are used and whether they have associated hits in the UV sectors and/or the PC1. The tracks are reconstructed with the Hough transform using both the X1 and X2 sections and are required to have an associated hit in the PC1. These tracks are then identified as electrons by passing a set of electron identification cuts. First the track is projected to the RICH where there should be PMTs fired around the projection. The number of PMTs fired is counted in an annulus and a disc. The variables for the number of PMTs fired are n_0 and n_1 respectively, with a representation shown in Figure 3.1. The inner radius of the annulus is 3.4 cm and the outer is 8.4 cm, surrounding the 5.9 cm Čerenkov radius of an electron. The disc has a radius of 11 cm, larger than that of the annulus. This analysis uses the n_1 variable with a cut requiring at least 5 PMTs to have fired. This is a harder cut that is generally used above the pion threshold, but since the MB trigger has sufficient statistics at the low momentum, we don't lose information by using the harder cut over the entire p_T range. This also removes the need to patch the spectra later if two different cuts were used.

After the RICH, the projection is matched to energy deposited in the EMCAL. The difference between the projection and the center of the energy deposition in the EMCAL are represented by $emcdz$ and $emcdphi$. These dif-

RICH focal plane

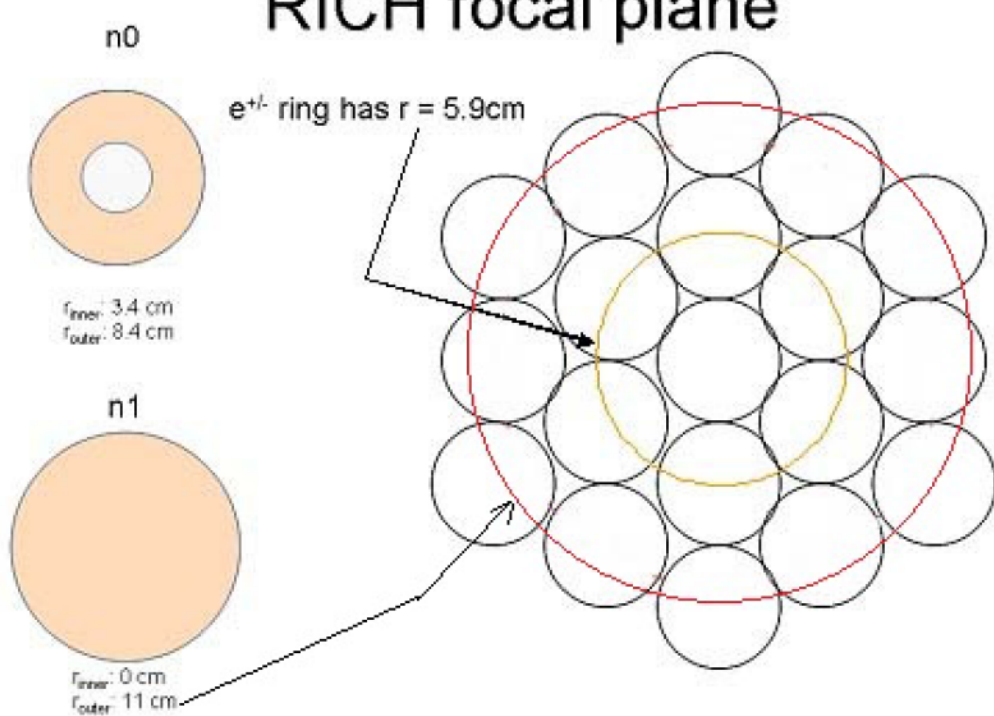


Figure 3.1: Derivation of RICH variables n_0 and n_1 .

ferences follow a Gaussian distribution which depends on the shower type, so cuts are made based on the sigma of the distribution assuming the appropriate resolution for an electromagnetic shower, represented by emcsdz_e and emcsdphi_e . A 3 sigma cut is made on the quadrature sum of the two ($\text{emcdtrk_e} = \sqrt{\text{emcsdphi_e}^2 + \text{emcsdz_e}^2}$).

A cut is also made on the shape of the EMC shower shape, called prob, defined as:

$$\text{prob} = \sum_i \frac{(E_i^{\text{pred}} - E_i^{\text{meas}})^2}{\sigma_i}, \quad (3.1)$$

where E_i^{meas} is the measured energy in tower i and E_i^{pred} is the predicted energy and prob is normalized to be between 0 and 1. Hadronic showers have a larger radius and thus have a smaller prob value. Finally a cut is made on the ratio of the energy deposited in the EMCal to the momentum determined by the DC, represented by E/p . An electron deposits most of its energy in the EMCal and since its mass is so small, $E \approx p$ and the E/p for an electron will be close to 1. Since hadrons don't typically deposit all of their energy, they will have an E/p less than 1. The E/p cut is made symmetrically around 1.

Variable	Value
$ zvtx $	< 20
n1	≥ 5
E/p	$0.8 < E/p < 1.2$
prob	$> 0.01 (> 0.2 \text{ for } p_T > 4.7 \text{ GeV/c})$
EMCal Track Matching	$\sqrt{\text{emcsdphi_e}^2 + \text{emcsdz_e}^2} < 3.0$
Track Quality	= (63 or 51 or 31)
DC/RICH gap cut	see text

Table 3.1: Electron identification criteria.

3.3 Run Selection

Once electron candidates are selected, run selection must be performed to remove any runs that are significantly different from the rest. Data acquired in-between successive starts of the PHENIX data acquisition (DAQ) system are PHENIX runs. The average number of electrons per event can fluctuate run-by-run due to a number of factors, including changes in live detector area, extra material in the detector, or changes in DAQ conditions. These outlier runs are a small portion of the total number of runs and have been removed

to simplify the analysis.

The number of electrons per event is plotted as a function of run number, after loose cuts on the number of events and electrons per event, in Figures 3.2 & 3.3 for the Minimum Bias (MB) trigger and EMCal-RICH Trigger (ERT) respectively. The runs are then separated into three groups. In group 3, with the highest number of electrons per event, a converter was installed in PHENIX that increased the photonic yield of electrons. Further information about the converter will be discussed in Chapter 4. Groups 1 & 2 are before and after the converter respectively. Unsatisfactory runs are removed by finding the weighted average of each group and then removing runs that are more than 3σ away from the average. This process is then iterated four times, after which all outliers have been removed. The MB & ERT plots with the runs removed are shown in Figures 3.4 & 3.5. The average number of electrons per event after the iteration process for the MB triggered data are as follows:

$$\begin{aligned}\left\langle \frac{N_e}{N_{\text{events}}} \right\rangle_{\text{Group1}} &= 0.01869 \pm 0.00041 \\ \left\langle \frac{N_e}{N_{\text{events}}} \right\rangle_{\text{Group2}} &= 0.01844 \pm 0.00049 \\ \left\langle \frac{N_e}{N_{\text{events}}} \right\rangle_{\text{Converter}} &= 0.03297 \pm 0.00042\end{aligned}$$

Since the two groups agree within errors they were thus treated as one group for the rest of the analysis. The same cannot be done with the ERT triggered data because the trigger threshold changed between Groups 1 & 2.

3.4 Randomly Associated Tracks

Though the electron ID cuts give a good sample of electrons, in a high multiplicity environment, overlap in the detectors can cause hadrons to be misidentified as electrons. The number and properties of those fake tracks reconstructed by random association can be obtained by exchanging, in software, the north and south halves of the RICH, and re-running the tracking. For example, DC tracks from the south are matched with the RICH north and vice versa. After the swap, there cannot be any actual tracks, and all reconstructed ones are, by definition, fake tracks. The north and south sides of the RICH are the same, with less than a 1% difference in dead area, so we can be reassured that the estimation is valid. To see the effect from these randomly associated (or swapped) tracks, the number of tracks are plotted as a function of E/p in p_T slices and shown in Figure 3.6. The red points are electrons

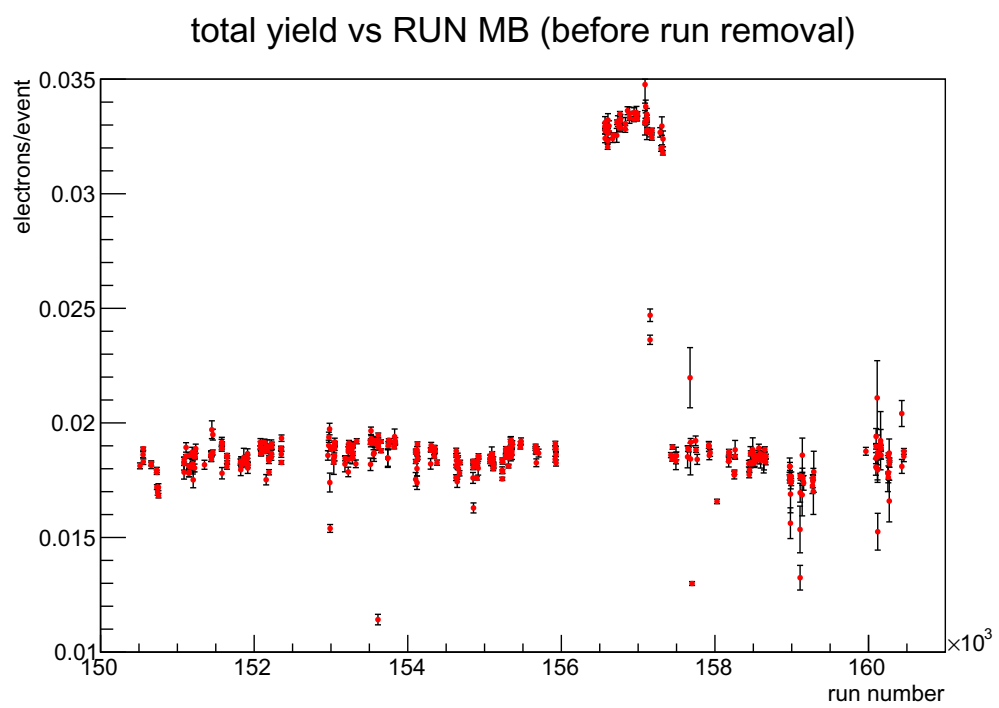


Figure 3.2: Number of electrons per event as a function of PHENIX run number for MB triggered events.

total yield vs RUN ERT (before run removal)

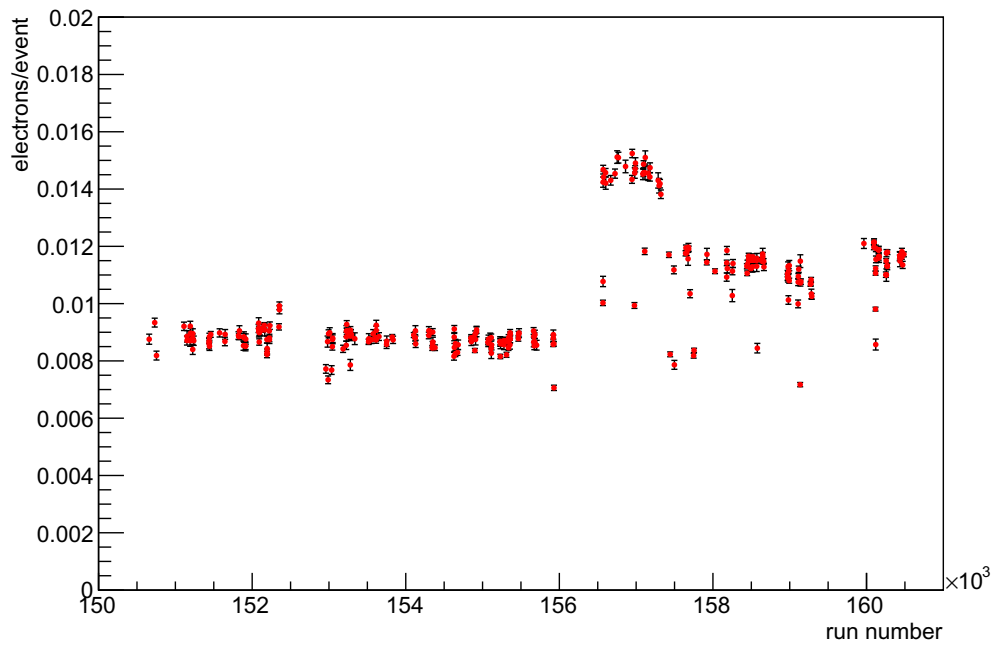


Figure 3.3: Number of electrons per event as a function of PHENIX run number for ERT triggered events.

total yield vs RUN MB

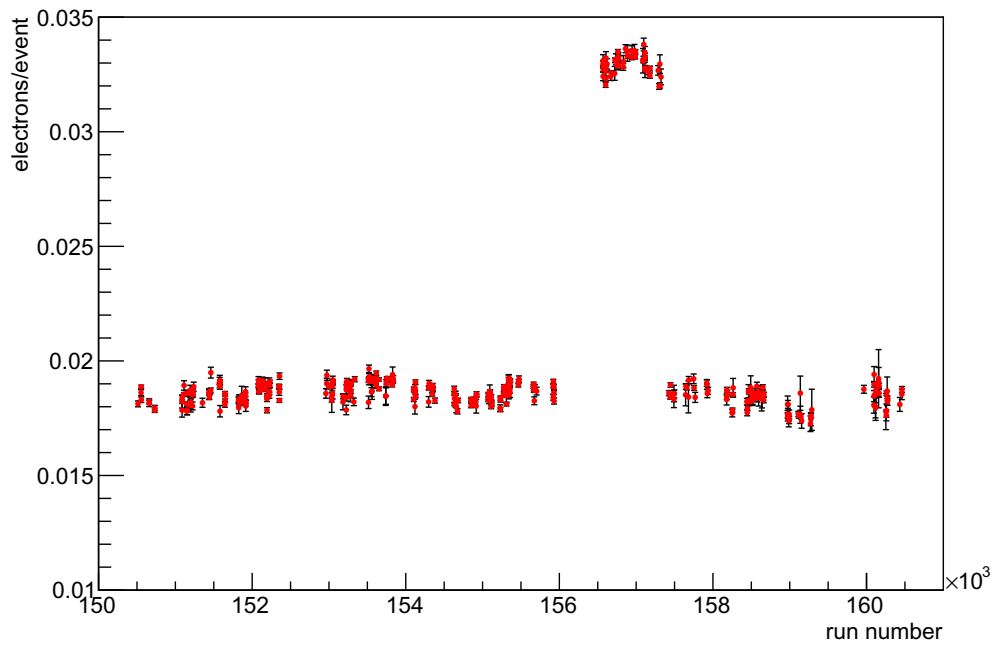


Figure 3.4: Number of electrons per event as a function of PHENIX run number for MB triggered events after run removal procedure.

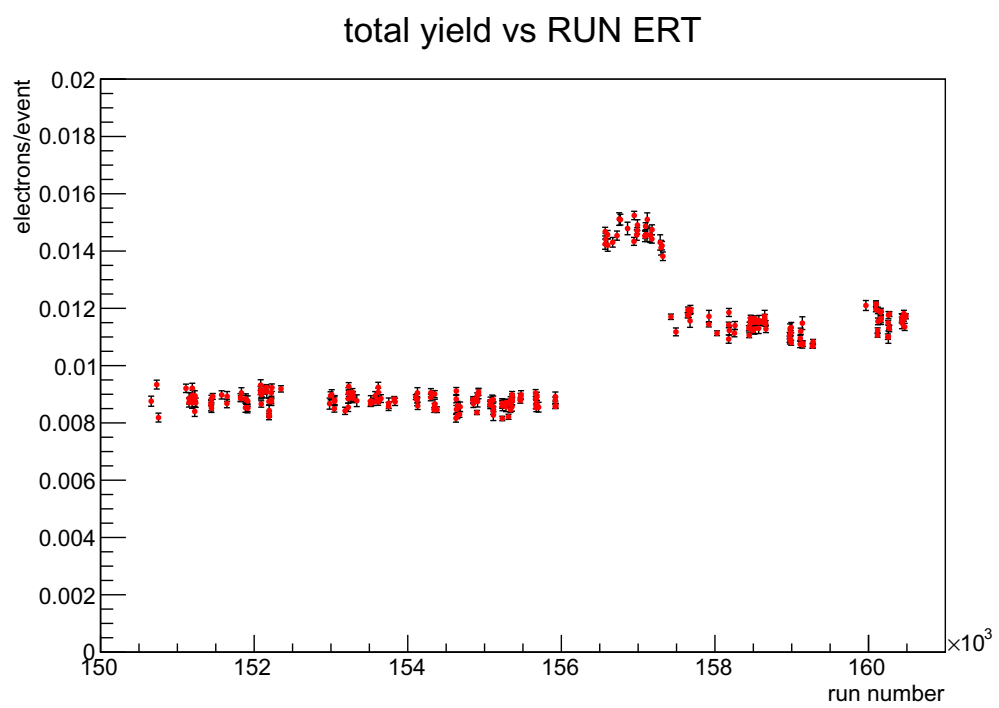


Figure 3.5: Number of electrons per event as a function of PHENIX run number for ERT triggered events after run removal procedure.

passing all the standard electron identification cuts from Table 3.1, except the E/p cut and the blue points are the same except the n1 cut is replaced with a cut on sn1, swapping the RICH. The contamination from randomly associated tracks is small underneath the electron peak and is largest at low momentum, where we expect hadrons to be since they do not deposit all of their energy in to the calorimeter.

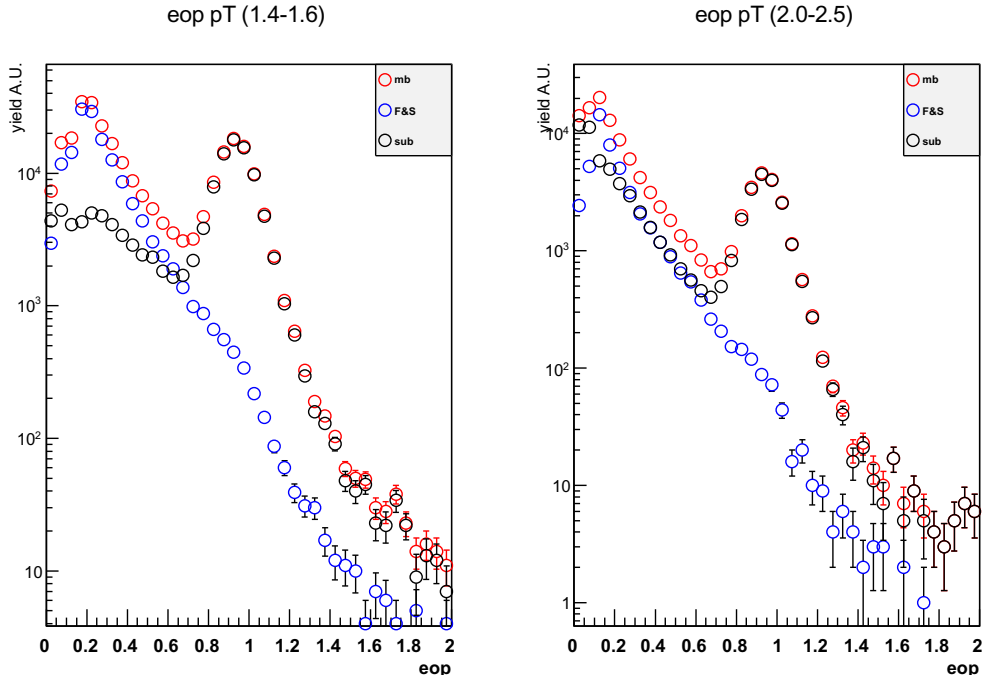


Figure 3.6: E/p graphs with electrons passing the $n_1 \geq 5$ cut in red, $sn_1 \geq 5$ cut in blue and the difference in black.

We can see the effect of the hadron background better on the electron spectra. Figure 3.7 shows the uncorrected MB electron spectra that pass the n_1 cut in red and sn_1 cut in blue. The effect of the hadron background is highest at the low momentum and is at most a 10 percent effect. The background is estimated and subtracted for each centrality separately.

3.5 Trigger Efficiency

A large number of events are satisfied by the MB trigger and the event rate sometimes exceeds the max DAQ rate. So, to keep the DAQ running

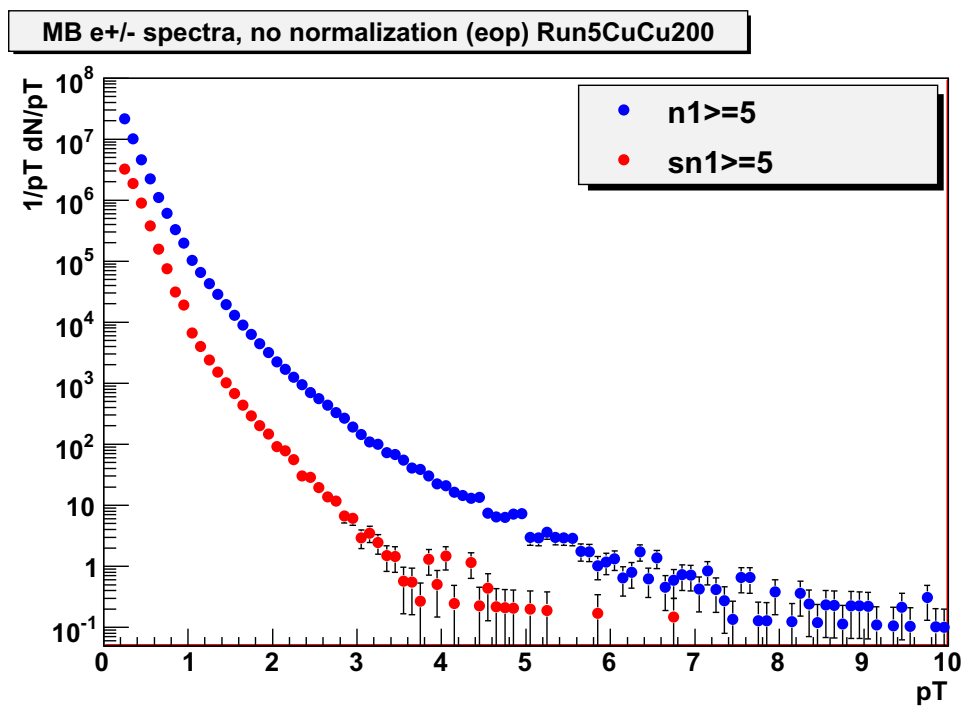


Figure 3.7: Uncorrected MB spectra for both the $n1$ and $sn1$ cuts.

smoothly and keep dead time to a minimum, not all events are written out. Instead a scale factor, n , is assigned to the trigger such that every $n+1$ event is written to disc and the rest are ignored. Triggers, in particular the ERT for this analysis, are specialized and do not fire on as many events. Most, if not all, of the triggered events are written to disc. We can exploit this fact to increase the statistics of our measurement in the high p_T region. To use the ERT data set, however, we must first make a few corrections.

As was just mentioned, not all of the MB, but most of the ERT, data are written to disc and they therefore have a different number of events. The final spectra in this analysis will be per event and so to make direct comparisons between the MB and ERT data sets we need to correct for the number of events in each. The number of events in the MB data set is just the number of recorded events, $N_{\text{MB}_{\text{recorded}}}$. The ERT trigger requires that the MB trigger fired and so the number of ERT events is linked to the number of MB events, specifically the total number of MB events if there were no scaledown, divided by the number of scaled down ERT events, $N_{\text{MB}_{\text{live}}}$,

$$N_{\text{MB}_{\text{live}}} = \frac{N_{\text{MB}_{\text{recorded}}} * (\text{scaledownfactor}_{\text{MB}} + 1)}{\text{scaledownfactor}_{\text{ERT}} + 1}. \quad (3.2)$$

The MB and ERT spectra, corrected for the number of events, are shown in Figure 3.8 for ERT group A and Figure 3.9 for group B.

The ERT data set must be corrected for the trigger bias. The ERT trigger efficiency is calculated as the fraction of electrons in the MB data set that pass the ERT trigger. The ERT trigger candidates are found by requiring the trigger bit to be set and that the trigger tile matches that of the electron track. There were two different trigger thresholds in the 2005 Cu+Cu run and the trigger efficiencies must be determined separately for each one. Figures 3.8 and 3.9 show the uncorrected spectra for group A and group B respectively.

Figure 3.10 shows the trigger efficiencies for the two different ERT groups, corresponding to two different trigger thresholds. We are only concerned with the plateau region since below that the MB statistics are sufficient enough that the ERT data is not needed. Group 1 has a larger threshold and thus the plateau starts at a higher p_T than group 2. Though only the plateau is of importance the statistics are poor there and a flat line fit to that region yield very different results depending on where the fit is started. Instead the points are fit to a Fermi-like function,

$$\epsilon_{\text{trigger}} = \frac{a}{\exp(-\frac{p_T - b}{c})}, \quad (3.3)$$

with the starting point set to approximately the middle of the rise region.

e⁺/- spectra, (eop) group A

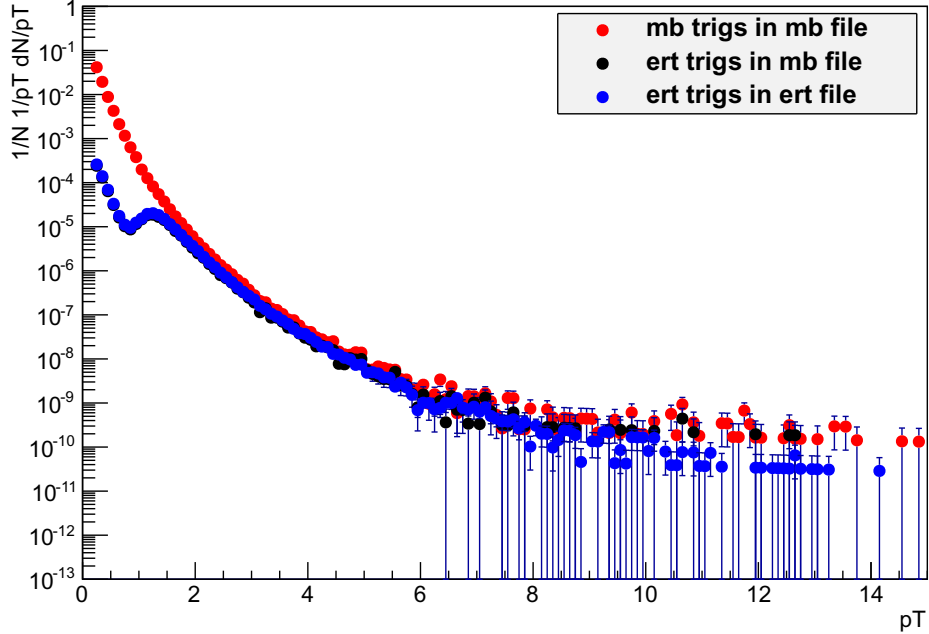


Figure 3.8: Uncorrected MB and ERT spectra from group A.

Equation 3.3 is used to correct the ERT spectra from the ERT data set. We take the ratio of the corrected ERT spectra and the MB spectra to ensure that the ERT spectra are corrected properly. The ratios are shown in Figure 3.11. The ratio shows that the ERT is being under-corrected by about 10%. The Fermi fit is very sensitive to the starting p_T point and as long as the resulting ratio between the MB and corrected ERT spectra is flat, we can apply a normalization correction. The ERT data will replace the MB data at 3 GeV and so a straight line is fit in that region and the ERT data is corrected up to match the MB data, ensuring a smooth transition.

e⁺/- spectra, (eop) group B

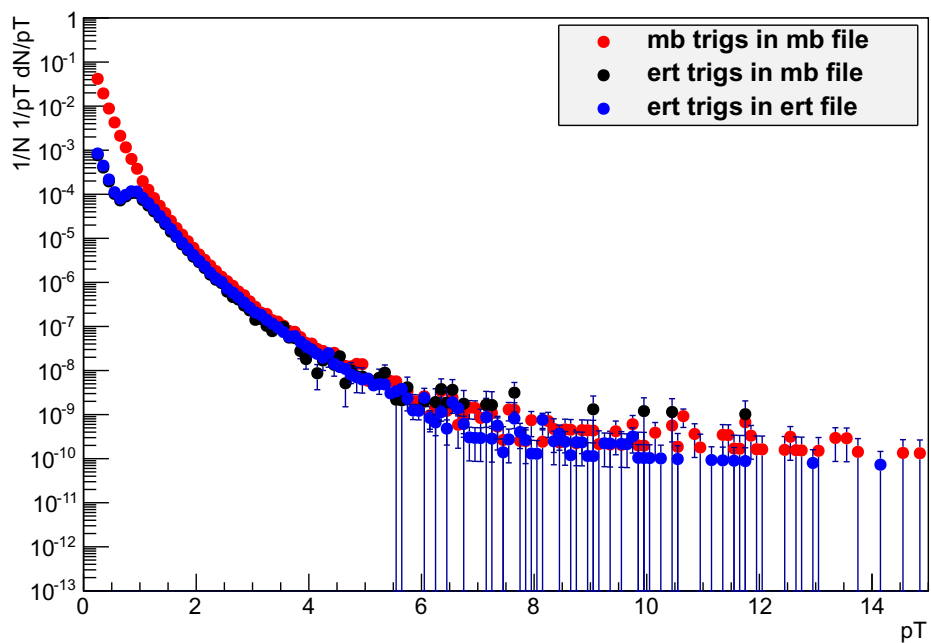


Figure 3.9: Uncorrected MB and ERT spectra from group B.

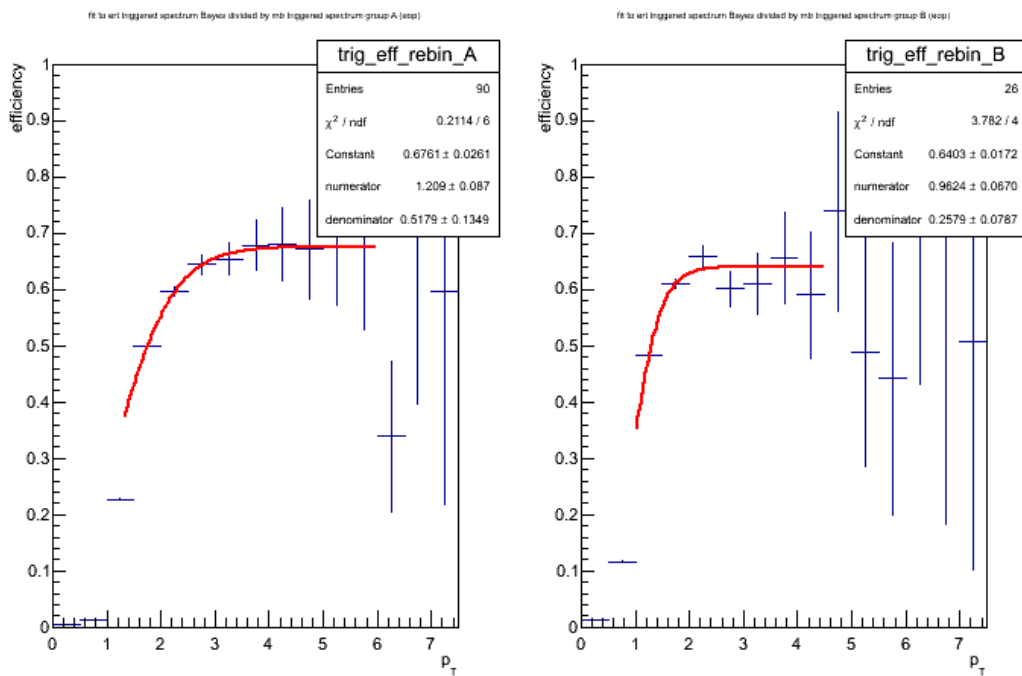


Figure 3.10: Trigger efficiencies for group A(left) and group B(right). Each is fit separately to a Fermi-like function.

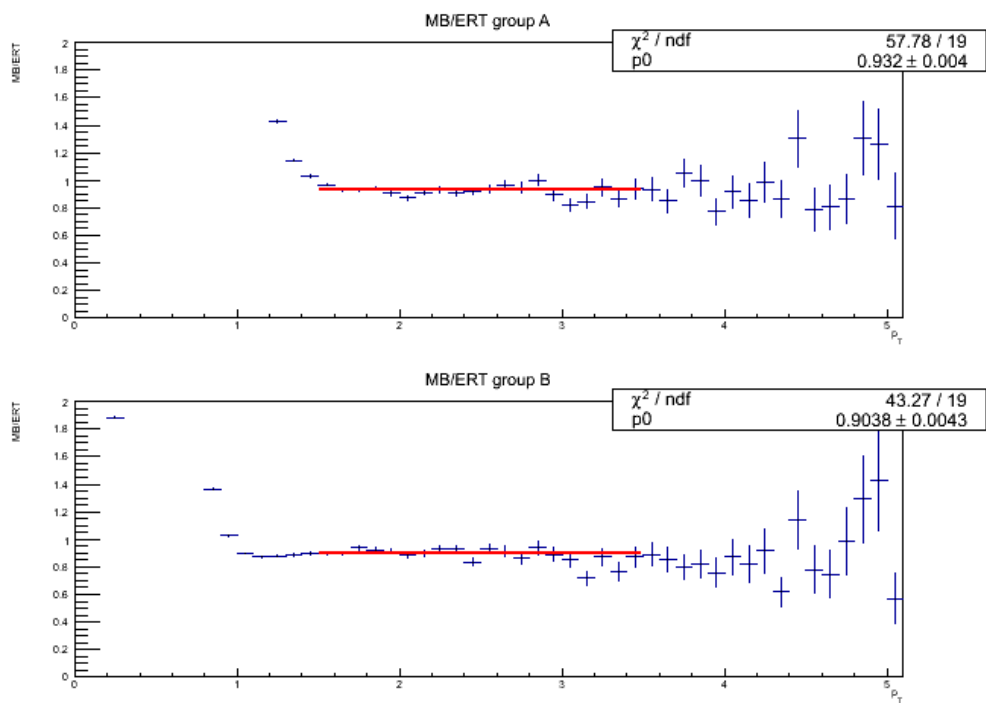


Figure 3.11: Ratio of corrected ERT spectra and MB spectra for group A (top) and group B (bottom).

3.6 Single Electron Efficiency

Before isolating the electrons from open heavy flavor, we must first make a measurement of the invariant electron yield,

$$E \frac{d^3N}{d^3p} = \frac{c}{2\pi p_T} \frac{d^2N}{dp_T dy}. \quad (3.4)$$

However, the yield as measured directly by PHENIX has an inherent bias caused by the detector itself. The central arm acceptance creates an artificial apparent azimuthal dependence to the yield. In addition there are parts of the detector that are not functioning during the run and others that we remove with fiducial cuts that lower the measured yield. The cuts used to isolate electrons are not 100% efficient and remove some good electrons in addition to removing background. In order to correct for the acceptance and efficiency effects we run a full GEANT simulation. Using a particle generator, EXODUS, two million electrons and two million positrons were generated with the following characteristics:

- Flat in p_T 0 - 15 GeV
- Flat in rapidity $-0.5 < y < 0.5$
- $-30 \text{ cm} < z_{\text{vertex}} < 30 \text{ cm}$
- $0 < \phi < 2\pi$

Electrons are generated in a larger rapidity range than the PHENIX acceptance, and later corrected back, in order to fully include edge effects. The generated electrons are run through the same analysis code as the data to ensure the same cuts are made. The electrons were generated flat in p_T to give sufficient statistics at high p_T . The simulated electrons are then run through a full GEANT based detector simulation and reconstructed the same as in the data. The simulated electrons are weighted with a realistic p_T distribution,

$$w(p_T) = \frac{0.006301 * p_T}{(0.4749 + p_T)^{8.461}}, \quad (3.5)$$

to account for momentum smearing effects due to the finite momentum resolution of the drift chamber. The weighting function used, Equation 3.5, is a power law fit to the expected spectrum of decay electrons.

3.6.1 Tuning Detector Response

It is important that the distribution of all variables agree in both simulation and data. Additionally, the detector acceptance must also agree in both. Figure 3.12 shows the comparison between data and simulation for the n1, prob and emcdtrk_e cut for two different p_T bins. In each of these distributions all electron cuts are made except for the one that is being plotted. The prob and emcdtrk_e cuts match well in the data and simulation. The n1 cut notoriously does not match well in data and simulation. The difference in the fractional yield at $n1 \geq 5$ is just short of 20%, whereas it is less than 5% at $n1 \geq 3$ cut. The solution is to set the n1 cut to $n1 \geq 3$ in simulation and correct the data up by the ratio of $n1 \geq 3$ to $n1 \geq 5$, more details will be shown in Section 3.6.2

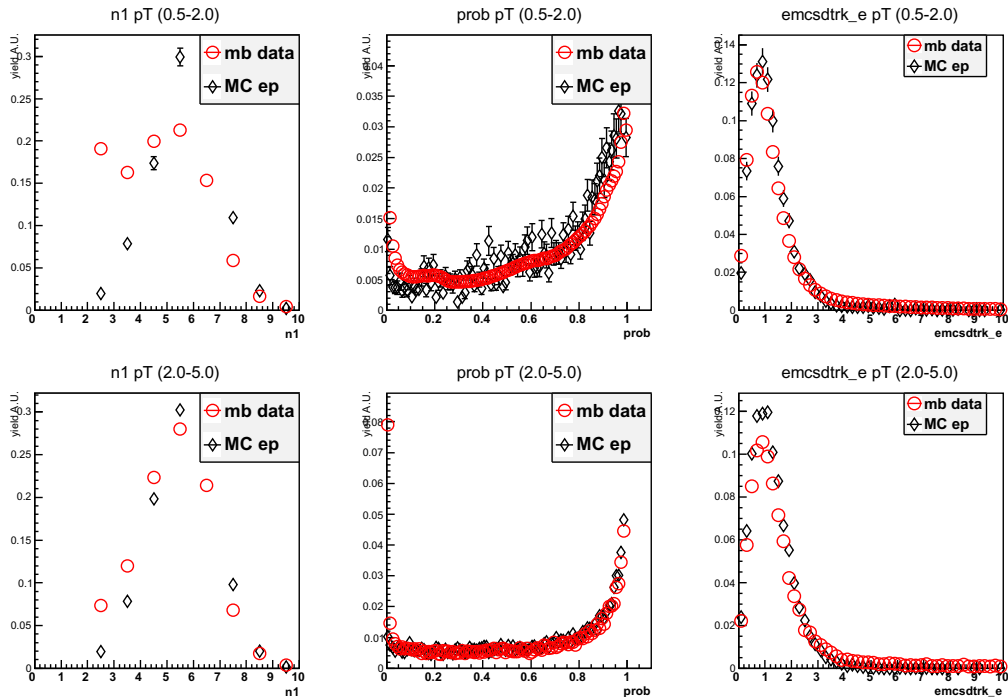


Figure 3.12: Top: From left, n1, prob and emcdtrk_e for p_T 1-2 GeV. Bottom: same for p_T 2-5 GeV.

The E/p distributions are fitted with a gaussian between $0.7 \leq E/p \leq 1.2$ in p_T slices. An example is shown in Figure 3.13. The means and sigmas of the fits are then plotted versus p_T and are shown in Figure 3.14 and Figure 3.15.

The means are fit with a simple plateau function

$$\mu = \frac{p_0}{1 + e^{-\frac{p_T - p_1}{p_2}}}. \quad (3.6)$$

The fit to the sigmas comes from the resolutions of the DC and the EMCAL and is described by the function,

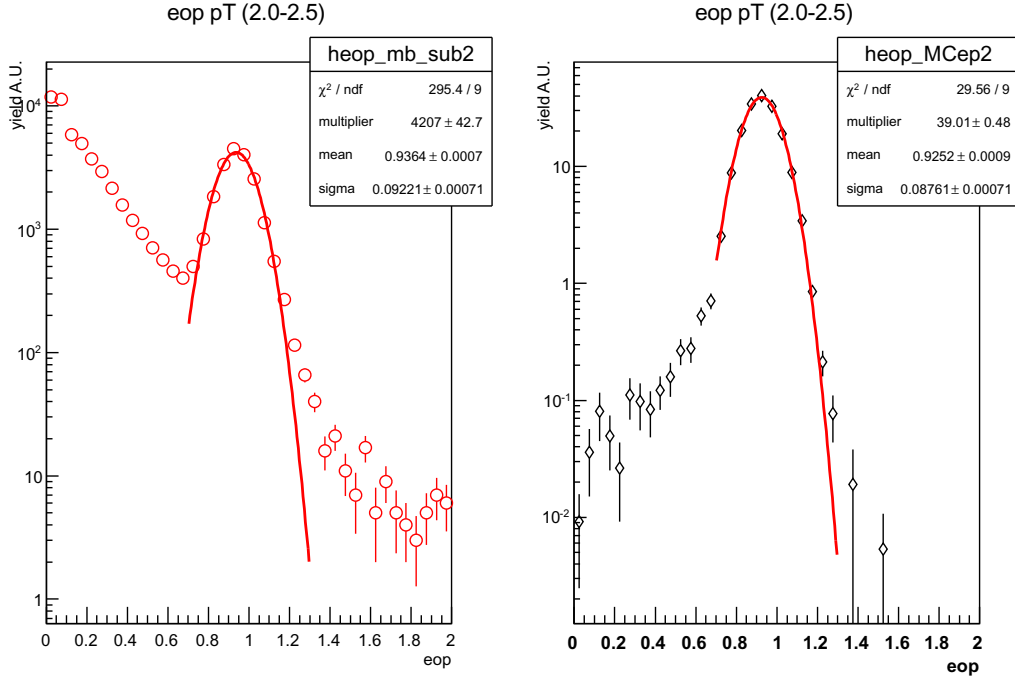


Figure 3.13: The E/p distribution fit with a Gaussian. Left: MB data. Right: Simulation.

The GEANT simulation does not accurately represent the DC and RICH gaps close to zero, so a fiducial cut is made is $\cos(\theta)$ vs $\text{bbc}z$ in both data and simulation. The result is shown in Figure 3.16. Comparison of the phi and zed variables are shown in Figures 3.17, 3.18 and 3.19.

3.6.2 RICH cut correction

In order to properly correct the data the simulation must accurately represent the different cuts that are used. The $n1 \geq 5$ cut is not well represented by the simulation and so simulated tracks are reconstructed with the $n1 \geq 3$ cut

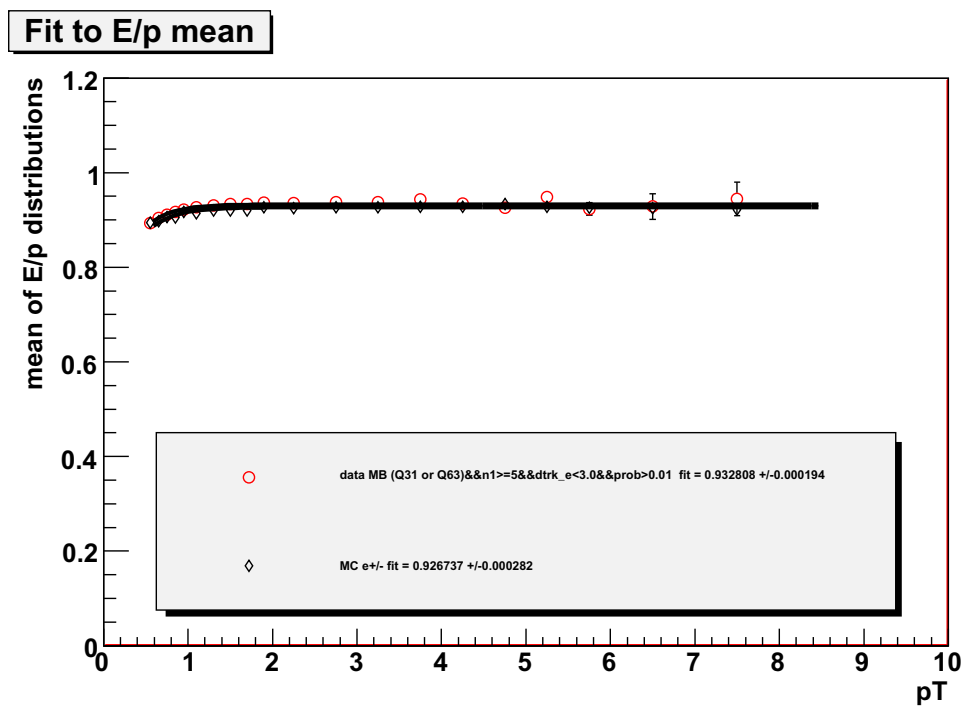


Figure 3.14: Mean of each Gaussian fit plotted vs p_T .

Fit to E/p sigma

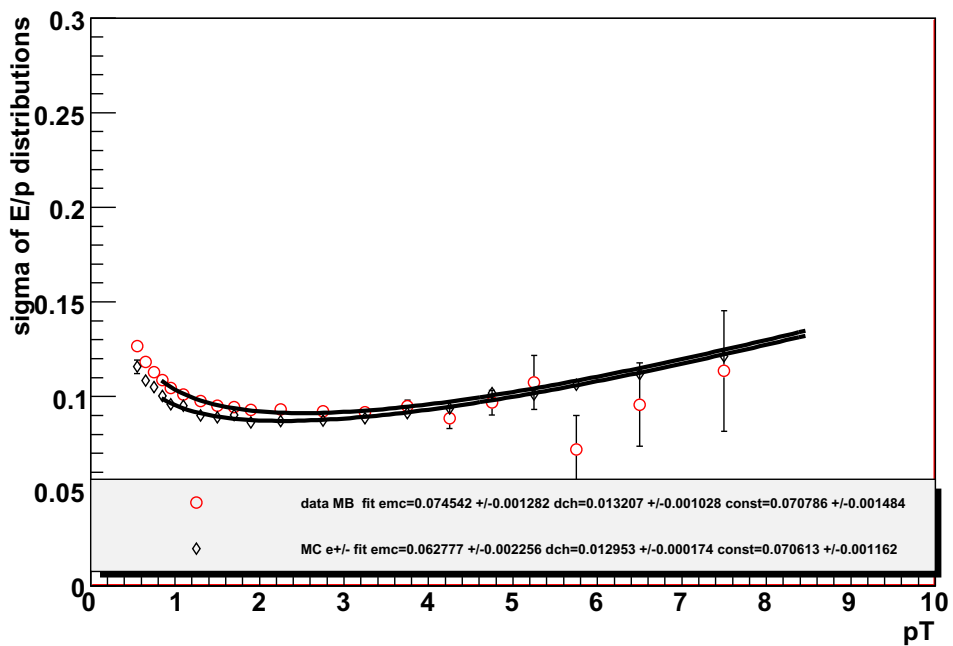


Figure 3.15: Sigma of each Gaussian fit plotted vs p_T .

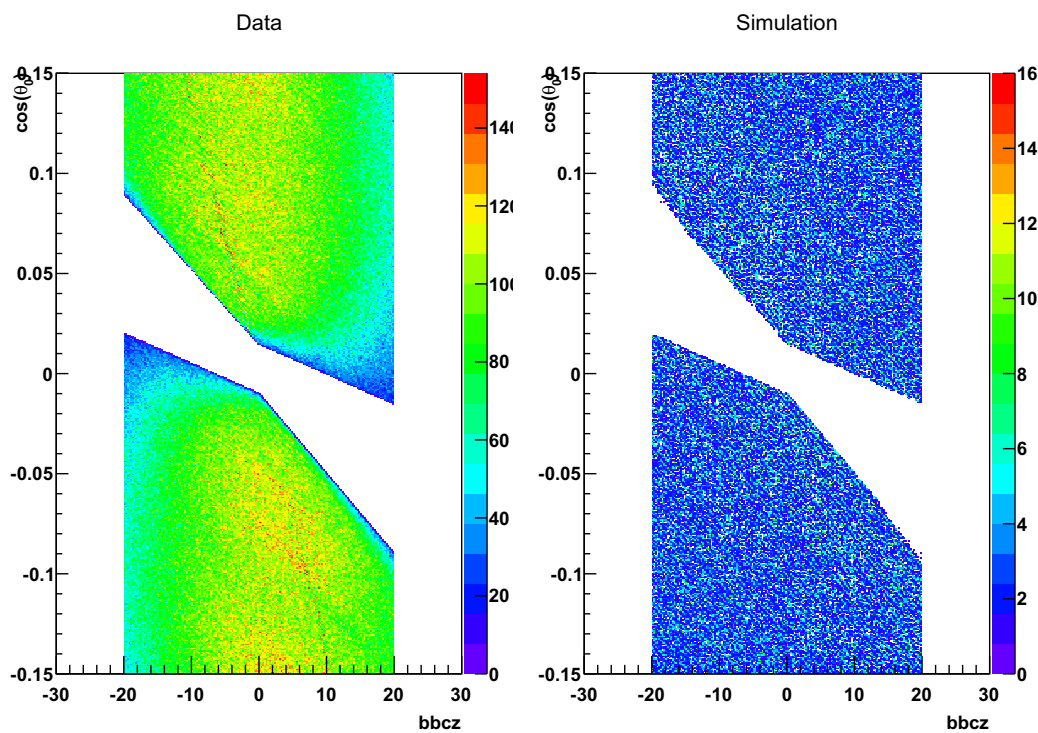


Figure 3.16: $\cos(\theta_0)$ vs bbc_z in data on left and in simulation on the right.

dN/dphi n1>=3 Run5CuCu200

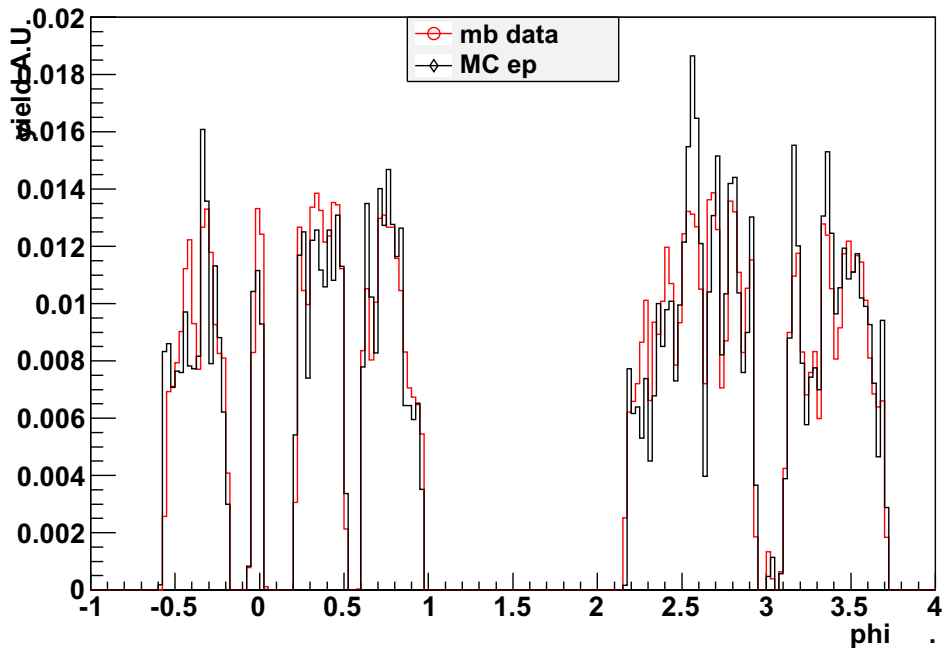


Figure 3.17: Comparison of real and simulated phi distributions. Data is in red.

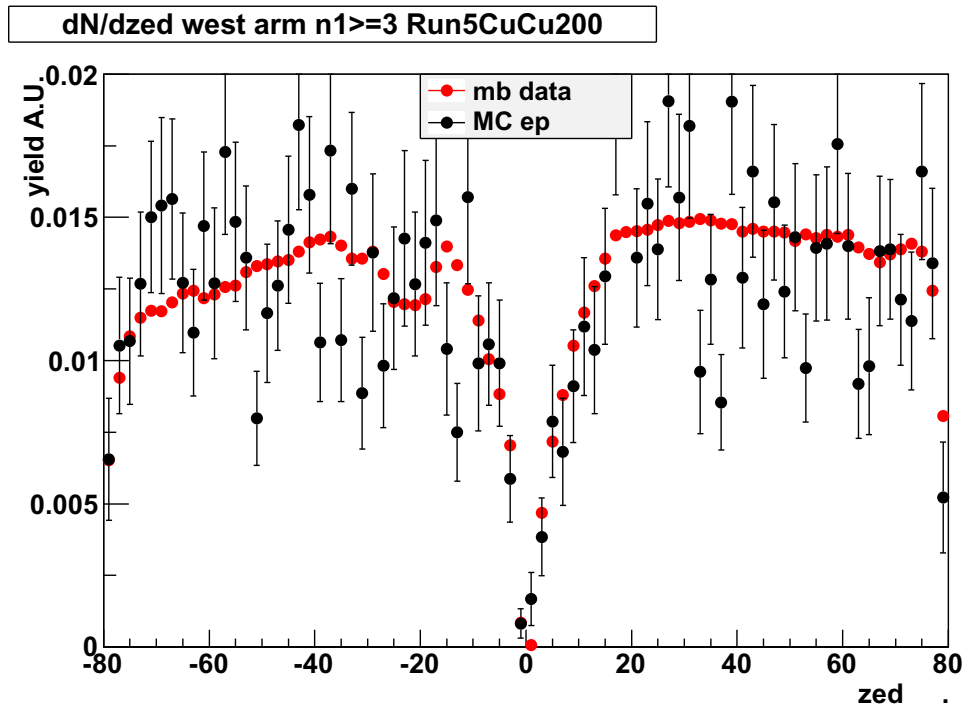


Figure 3.18: Comparison of real and simulated zed distribution for the west arm. Data is in red.

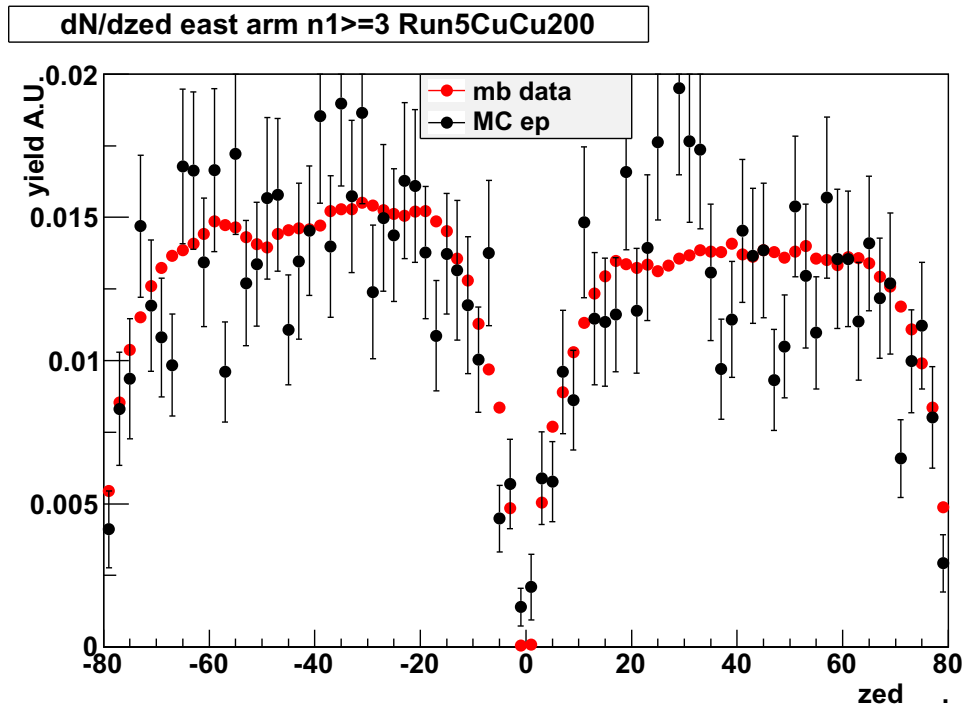


Figure 3.19: Comparison of real and simulated zed distribution for the east arm. Data is in red.

instead. The pions begin to radiate in the RICH at $p_T \sim 5$ GeV and the harder $n1 \geq 5$ cut is needed there. Instead of using the looser cut and then stitching the two together, the harder $n1 \geq 5$ cut is used over the whole p_T range in data. To correct for the usage of different cuts in the data and simulation, we take the ratio of the $n1 \geq 3$ and $n1 \geq 5$ spectra in data and correct up the $n1 \geq 5$ curve by that factor for each centrality. This ratio is shown in the left panel of Figure 3.20. The same is done to the $sn1$ curves before subtraction, in the right panel of Figure 3.20.

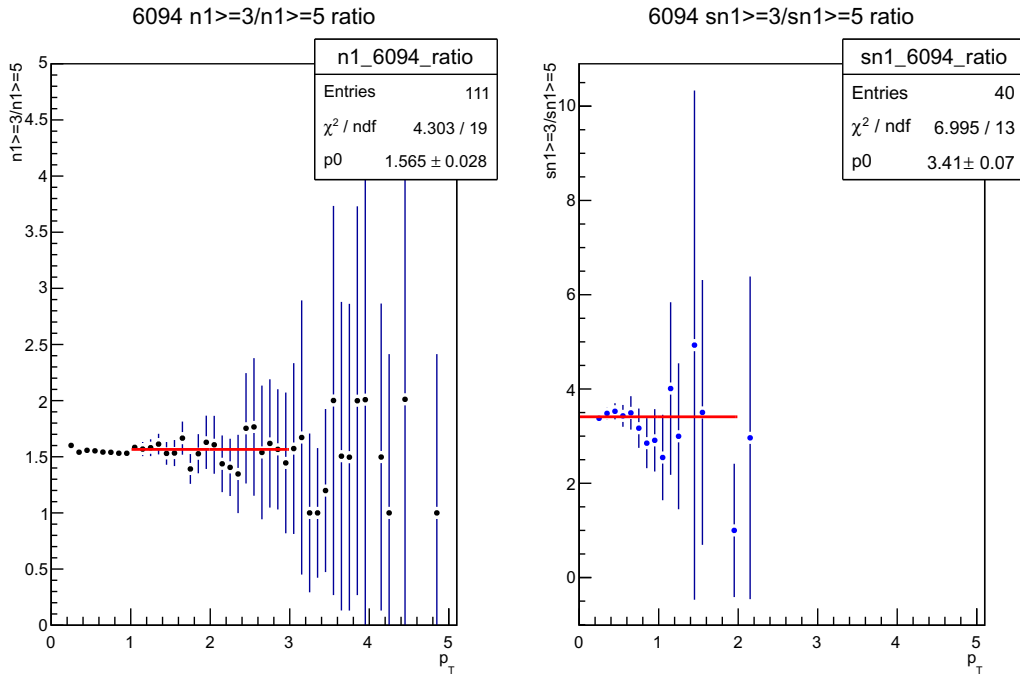


Figure 3.20: Left: Ratio of the $n1 \geq 3$ and $n1 \geq 5$ spectra. Right: Ratio of $sn1 \geq 3$ and $sn1 \geq 5$ spectra.

3.6.3 Acceptance×efficiency correction

The output spectrum of reconstructed electrons is subsequently corrected for bin width, number of particles and the smaller eta distribution in PHENIX. To calculate the acceptance*efficiency correction the corrected output spectrum is divided by the input spectrum of generated electrons. The resulting

curve, shown in Figure 3.21, is fit to a function of the form:

$$\frac{p_0 + p_1 * p_T + p_2 * p_T^2}{1 + \exp[-\frac{p_T - p_3}{p_4}]} \quad (3.7)$$

which is then used to correct the data. This correction does not include the n1 correction from Section 3.6.2.

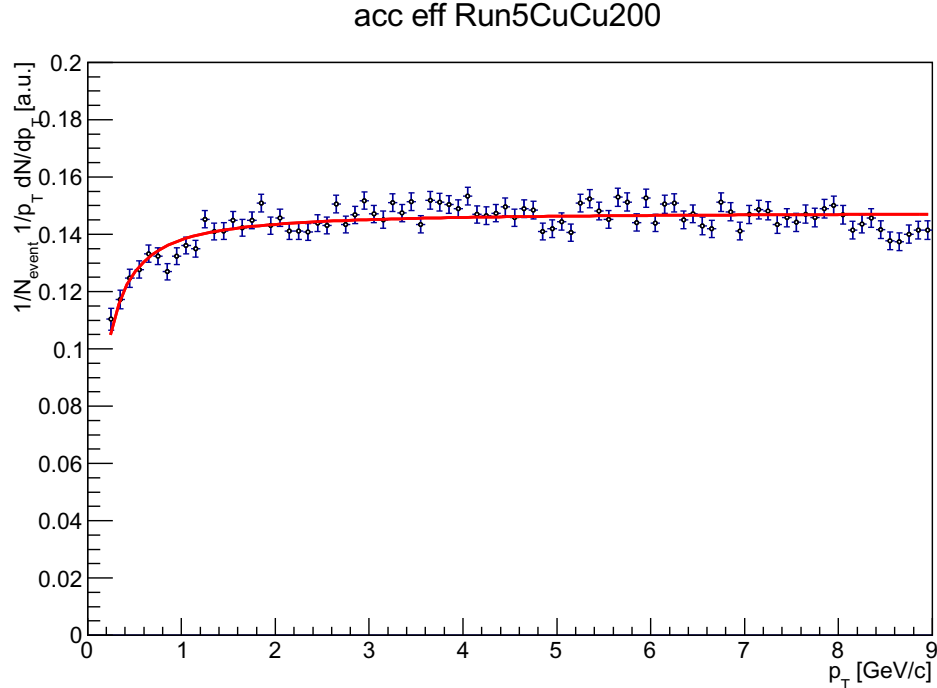


Figure 3.21: Acc* Eff curve.

3.6.4 Invariant yield

After the acceptance*efficiency correction is applied to the raw yield, there are still a few corrections to make to get an invariant yield. Equation 3.4 for the invariant yield can be rewritten as,

$$\frac{1}{2\pi p_T} \frac{d^2 N}{dp_T dy} = \frac{1}{N_{\text{events}}} \frac{1}{2\pi} \frac{1}{2} \frac{1}{p_T} \frac{N_e}{\Delta p_T} \frac{1}{\Delta y} \frac{\epsilon_{\text{BBC}}}{\epsilon_{\text{eID}}}, \quad (3.8)$$

where the various factors are:

- N = number of electrons and positrons per event divided by two
- $\frac{N_e}{\Delta p_T}$ = total number of measured electrons and positrons in a particular p_T bin
- N_{events} = number of events
- ϵ_{BBC} = BBC efficiency for Minimum Bias
- ϵ_{eID} = Acceptance*efficiency correction

Bin width correction

The invariant yield is a differential distribution in p_T . There are limited statistics and thus we cannot measure the yield for each p_T and instead a measurement is made over a range of p_T , called the bin width, and the average value of the bin is taken as the yield and is plotted in the center of the bin. However, for a steeply falling spectrum, the actual p_T that corresponds to the average value of the bin will not be in the center, but rather to the left.

The initial measurement is made in p_T bins with a width of 0.1 GeV. These bins are small enough that any error that occurs from placing the bin average at the center of the bin is negligible. In the final spectra, bins are combined to reduce the statistical uncertainty and the error due to the bin shift cannot be ignored. We use the standard PHENIX re-binning technique to correct for this by adjusting the height of the bin to represent the value of the yield at the p_T bin center. This procedure assumes that the invariant differential yield as a function of p_T does not oscillate wildly, which is a reasonable assumption.

First, we fit the yield with a modified power law,

$$f(p_T) = \frac{A}{(p_0 + p_T)^n}, \quad (3.9)$$

where the bin center are the initial p_T values and A , p_0 , and n are fitting parameters that are determined by the fit at each iteration.

Next the values of p_T are found where Equation 3.9 takes on its average value in each bin ($[a,b]$) by solving for p_T in the equation

$$\langle f \rangle_{[a,b]} \equiv \frac{1}{b-a} \int_a^b f(x) dx = f(p_T^{mean}). \quad (3.10)$$

Then Equation 3.9 is plugged into Equation 3.10 and we solve for p_T^{mean} ,

$$p_T^{mean} = \left(\frac{A}{\langle f \rangle}\right)^{-n} - p_0. \quad (3.11)$$

Next the center of the bins are moved to the p_T^{mean} and the procedure is iterated until the p_T^{mean} 's converge.

Finally, the value of the bin and its error are rescaled so the center of the bin corresponds to the bin value,

$$y' = y \times \frac{f(\frac{b-a}{2})}{f(p_T^{mean})}, \delta y' = \delta y \times \frac{f(\frac{b-a}{2})}{f(p_T^{mean})}. \quad (3.12)$$

This is then the value of the invariant yield at the value of p_T where the final plotted data point rests. The yield is then independent of a particular momentum binning and can be more easily compared to other data and theories.

Inclusive spectra

After all of the corrections are applied, we are then left with an invariant yield of all electrons, the inclusive yield. The inclusive electron yield for the MB and five centrality bins are shown in Figure 3.22.

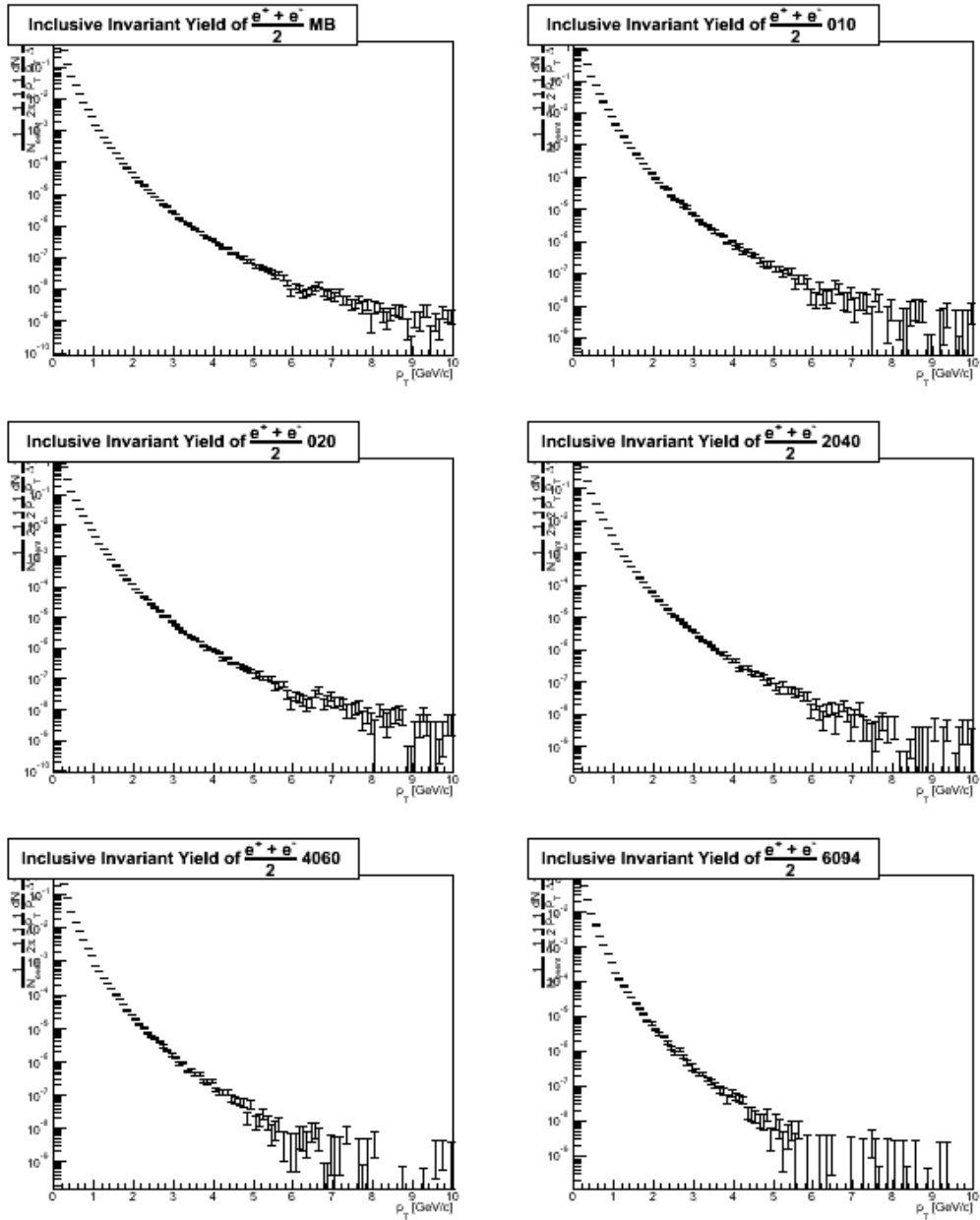


Figure 3.22: Fully corrected inclusive electron spectrum for MB and 5 centralities.

Chapter 4

Estimation of Electron Background Sources

After the inclusive yield is measured, the electrons from open heavy flavor decays must be isolated. The inclusive yield can be broken up into two parts, electrons from photonic sources and electrons from non-photonic sources. Electrons from photonic sources come from the Dalitz decays of light mesons (π^0 , η , η') [40] and photon conversions, all of which are background. The non-photonic electrons are from the following sources:

- Decays of light vector mesons (ρ , ω , ϕ)
- Decays of hidden heavy flavor (J/ψ , Υ)
- Weak kaon decays (K_{e3})
- Decays of open heavy flavor hadrons (one heavy quark, the rest light quarks)

The electrons from open heavy flavor decays are what we want to isolate and the other sources need to be removed. The photonic background electrons are removed with two separate methods, the cocktail method and the converter method. The cocktail method uses a decay generator to create a “cocktail” of background electrons which are then subtracted from the inclusive yield. The converter method is a data driven method that involves wrapping a brass sheet around the beam pipe to increase the photonic component of the electron yield. From the increased number of photon conversions with the converter installed, the non-photonic component of the inclusive yield can be isolated.

The converter method, however, cannot isolate the background electrons from non-photonic sources, the cocktail is needed for that. Though the cocktail method removes all background sources, it suffers from poor systematic uncertainty, in particular at low p_T where the background is large. The converter method has better systematic errors, but there were not many runs with the converter installed and thus it suffers from low statistics. To get the yield of electrons from open heavy flavor decays a combination of the two methods is used.

4.1 Cocktail Method

In the Cocktail method the electron background is estimated with the EXODUS decay generator [41]. Particles are generated flat in p_T from 0-15 GeV and flat in rapidity $-1 < y < 1$.

4.1.1 Light Mesons

Electrons from the pion Dalitz decay are the primary source of background. PHENIX has made a measurement of neutral pions in the Run 5 CuCu data set [42]. A modified Hagedorn function,

$$\frac{1}{2\pi p_T} \frac{d^2N}{dp_T dy} = \frac{c}{[e^{ap_T - bp_T^2} + p_T/p_0]^n} \quad (4.1)$$

is fit to the π^0 data and used as the input parent π^0 spectrum to EXODUS. The fits are done separately for each centrality and the MB and are shown in Figure 4.1. The ratios of the fit to the data are shown in Figure 4.2. The neutral pion data begins at 1 GeV and thus does not constrain the fit in the low p_T region. In previous analyses the average of the charged pion data was used in the low p_T region, but there is no such equivalent final analysis in the Run 5 Cu+Cu data set. However, the cocktail background subtraction technique is only used above 1 GeV in this analysis because there is sufficient converter data (described in Section 4.2) to use below 1 GeV where the signal to background ratio is low. A double check was devised to make sure we are not losing any information by using only the neutral pion yield, which is described in Section 4.1.2.

The following light mesons are included in the cocktail.

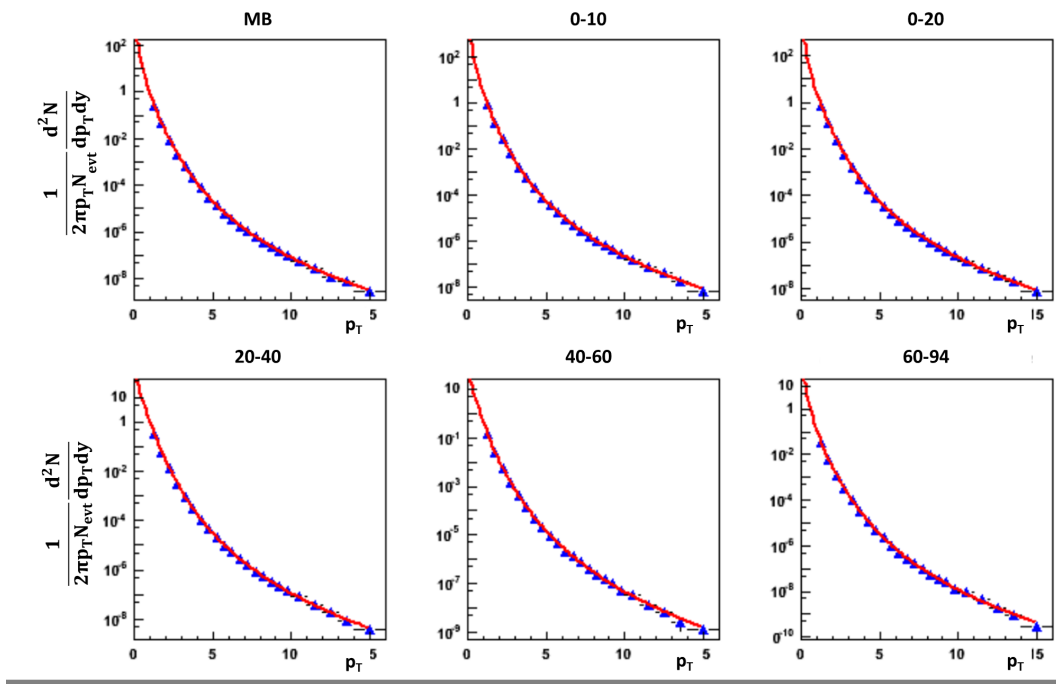


Figure 4.1: Hagedorn fit to the neutral pion data in MB and 5 centralities.

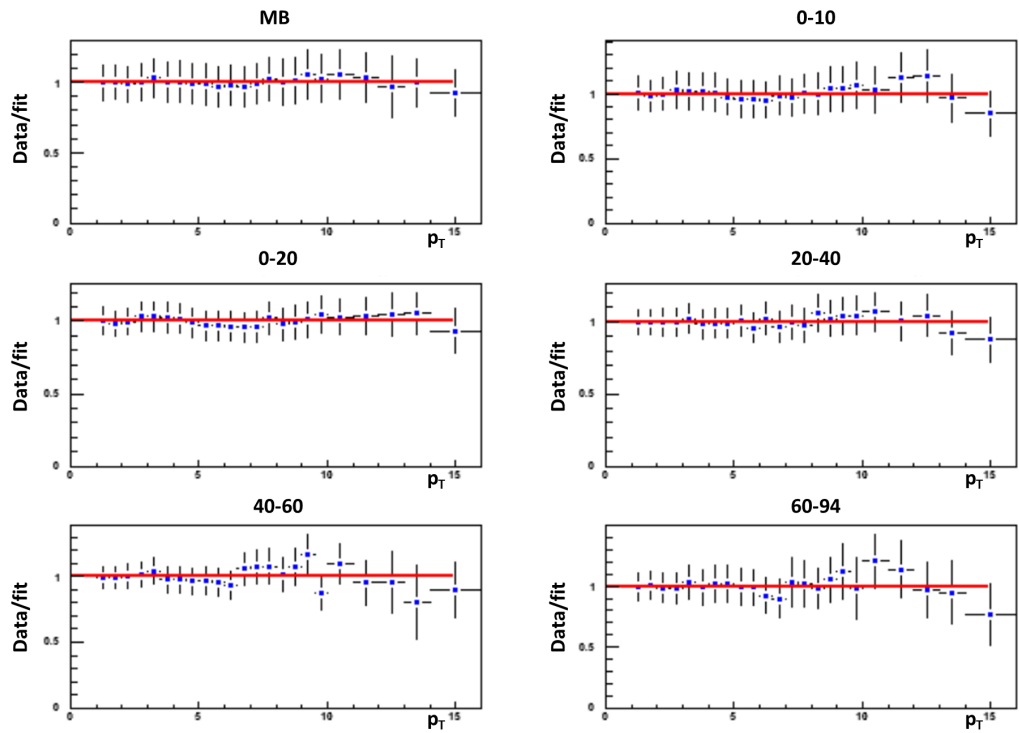


Figure 4.2: Ratio of the data to the fit for MB and 5 centralities.

- $\pi^0 \rightarrow \gamma e^+ e^-$
- $\eta \rightarrow \gamma e^+ e^-$
- $\eta' \rightarrow \gamma e^+ e^-$
- $\rho \rightarrow e^+ e^-$
- $\omega \rightarrow \pi^0 e^+ e^-$ and $\omega \rightarrow e^+ e^-$
- $\phi \rightarrow \eta e^+ e^-$ and $\phi \rightarrow e^+ e^-$

The input parent spectra of the other mesons is approximated by m_T scaling the pion fit using the substitution

$$p_T \rightarrow m_T = \sqrt{p_T^2 + (M_{\text{meson}}^2 - M_{\pi^0}^2)} \quad (4.2)$$

and normalizing to the meson/ π^0 ratio at high momentum. The ratios are shown in Table 4.1.

η/π^0	0.48 ± 0.03 [43]
η'/π^0	0.25 ± 0.075 [41]
ρ/π^0	1.00 ± 0.30 [41]
ω/π^0	0.90 ± 0.06 [44]
ϕ/π^0	0.40 ± 0.12 [41]

Table 4.1: meson/ π^0 ratios at high momentum.

4.1.2 Pion double check

As a cross check an alternative method was developed to determine the π^0 spectrum from the single electron data. For this method we use the converter data. The simulated EXODUS spectrum for π^0 is used to create a new pion input for EXODUS in an iterative procedure until the pion output matched the newly created input. It is described in the equation below,

$$\pi_{\text{new}} = (e_\gamma)_{\text{converter}} \left(\frac{e_\pi}{e_\gamma} \right)_{\text{cocktail}} \left(\frac{\pi}{e_\pi} \right)_{\text{cocktail}} \quad (4.3)$$

where $(e_\gamma)_{\text{converter}}$ is the photonic electron spectrum from the converter analysis (detailed in the next section), $(e_{\pi(\gamma)})_{\text{cocktail}}$ is the electron decay spectrum from

pions(all photonic sources), π_{cocktail} is the pion spectrum output from EXODUS and π_{new} is the new pion spectrum from the combined components. First the neutral pions are fit to the Hagedorn function and the fit is used as the input pion parent spectrum in EXODUS as outlined above and shown in Figure 4.1. This EXODUS output gives us the following:

- $(\pi)_{\text{cocktail}}$ - pion spectrum
- $(e_\pi)_{\text{cocktail}}$ - electron decay spectrum from pions
- $(e_\gamma)_{\text{cocktail}}$ - electron decay spectrum from all photonic sources.

The converter analysis, detailed in the next section, gives us the other photonic electron spectrum. Once all the pieces are combined, the resulting spectrum, π_{new} , is compared to $(\pi)_{\text{cocktail}}$, the pion spectrum from EXODUS. The ratio of the two, in the first iteration, are shown in Figure 4.3 for the MB. The only importance is that the ratio is flat, overall scaling problems are fixed in the comparison of the cocktail and converter analyses. Figure 4.3 shows that the two methods match in shape except at low momentum where there is no data for the neutral pions and we know the original Hagedorn is not constrained.

Since the two do not completely match, the π_{new} spectrum and the neutral pions are combined and refit to the Hagedorn. The spectra and fits are shown in Figure 4.4 for the first iteration. This new fit is then put into EXODUS and the output creates new versions of $(\pi)_{\text{cocktail}}$, $(e_\pi)_{\text{cocktail}}$, and $(e_\gamma)_{\text{cocktail}}$ in Equation 4.3 to calculate π_{new} for the next iteration. The π_{new} for this iteration is then compared to the EXODUS output just as done previously. The results for the MB and 5 centralities are shown in Figure 4.5. Since all the ratios are flat no additional iterations are necessary.

The cocktail using the final iteration of π_{new} was then carried through the rest of the analysis steps to determine the open heavy flavor yield which was then compared to the yield calculated with just the neutral pions. The two agree within statistical errors. In order to use the iterative procedure for the final yield, we must calculate the systematic errors, which is not trivial. We can be satisfied that using cocktail calculated from the neutral pion data does not affect the final outcome.

4.1.3 Conversions

Conversion electrons are the next main source of background for electrons. Conversion electrons come mostly from the conversion of a decay photon from

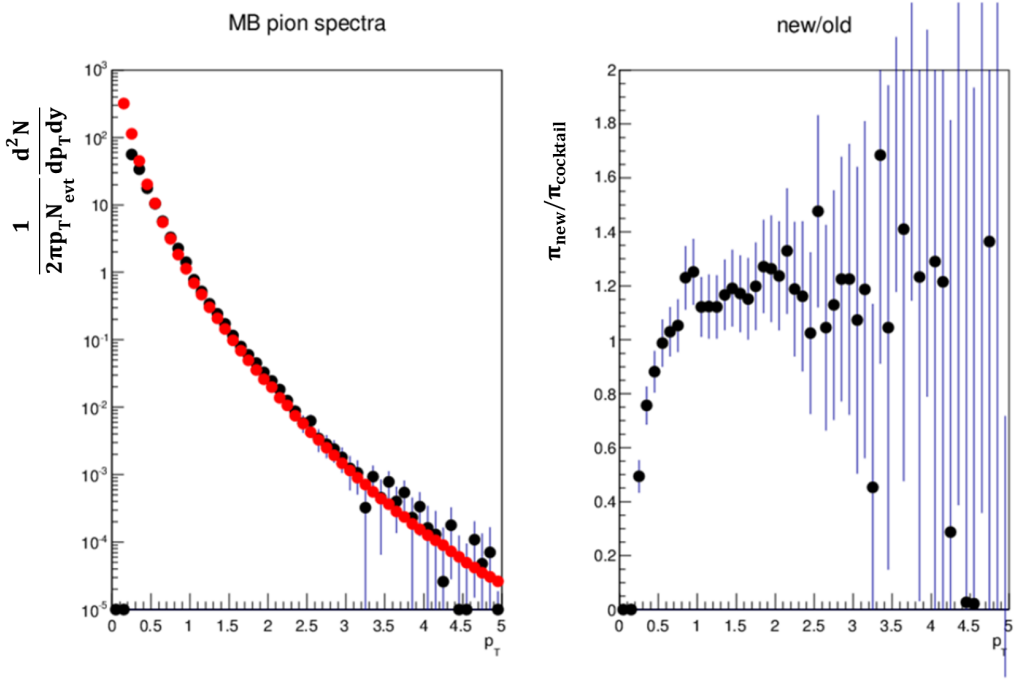


Figure 4.3: Left: π_{new} in black, $(\pi)_{\text{cocktail}}$ in red. Right: Ratio of π_{new} and $(\pi)_{\text{cocktail}}$.

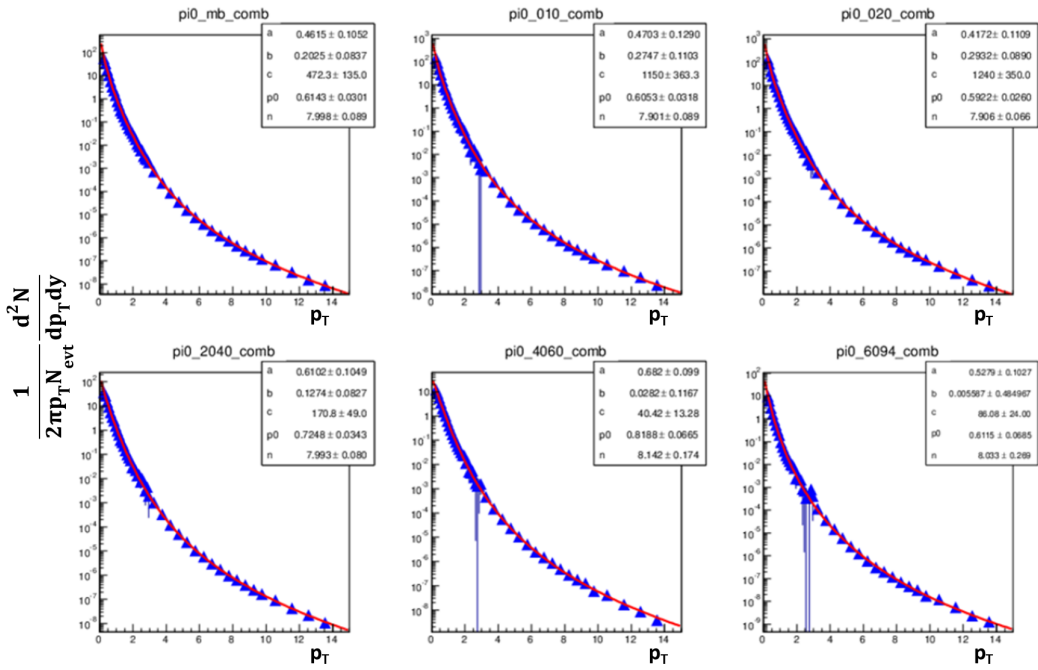


Figure 4.4: Hagedorn fit to the combination of π_{new} and the original neutral pions. π_{new} ends at 3 GeV where the statistics start to run out.

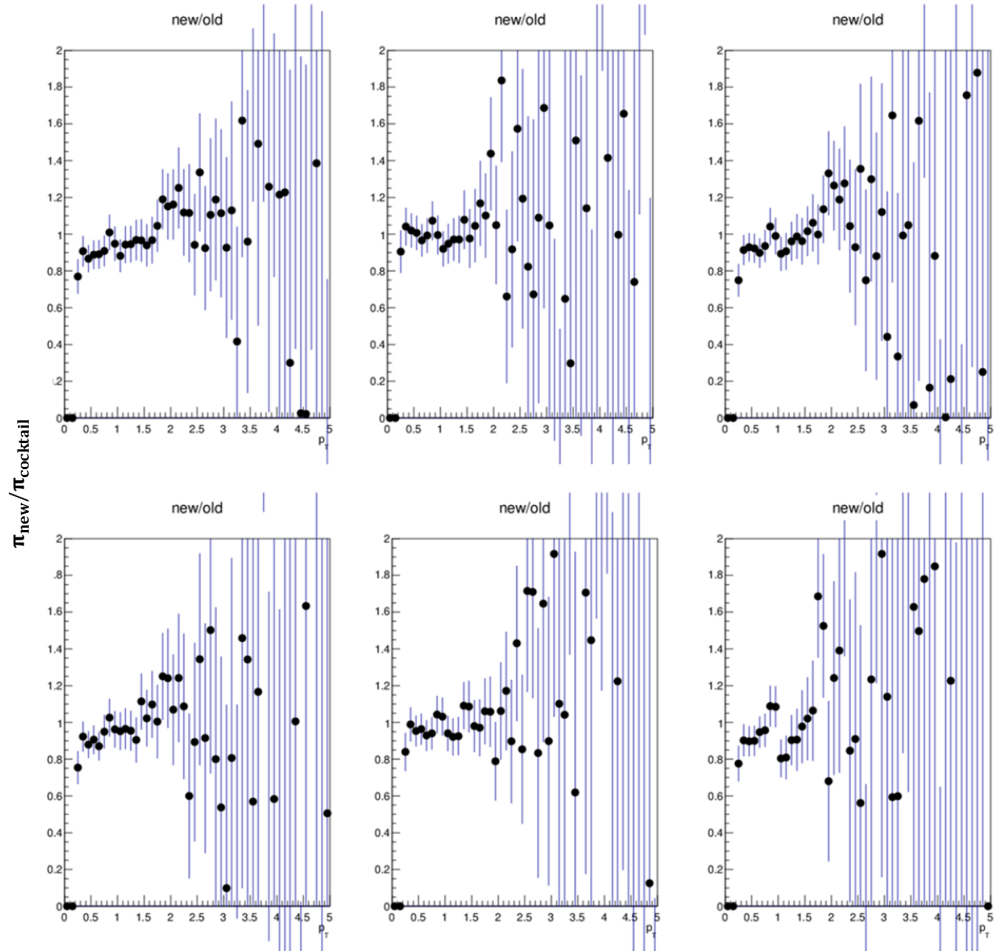


Figure 4.5: Ratios of π_{new} and $(\pi)_{\text{cocktail}}$ for a second iteration for MB and 5 centralities.

$\pi^0 \rightarrow \gamma\gamma$, and so their kinematics will closely resemble those that come from the pion Dalitz decay. Therefore we can estimate the conversion contribution by scaling the pion Dalitz decay by an appropriate factor.

Using a decay generator, $\pi^0 \rightarrow \gamma\gamma$ decays and $\pi^0 \rightarrow e^+e^-\gamma$ decays were generated and run through the reconstruction framework. The ratio of electrons from the conversion of photons from $\pi^0 \rightarrow \gamma\gamma$ decays to electrons from π^0 Dalitz decays is 0.403 and has a 10% systematic error.

Conversions from the η (the only other light meson with a significant contribution) are treated similarly. The ratio is rescaled to properly account for the difference in branching ratios as the parent mass is increased.

4.1.4 Ke3 Decays

Ke3 decays provide an additional source of background. Electrons from the Ke3 decay of Kaons in flight originate away from the vertex, outside of the magnetic field. The momentum of these electrons is reconstructed too high, and as a result most do not pass the E/p cut. Those that do remain are a small portion of the background and have the most effect at low momentum ($\sim 10\%$ at the lowest p_T , negligible by 1 GeV). A full simulation was performed for p+p [45] and is N_{coll} scaled for the Cu+Cu data.

4.1.5 Direct Photon Contributions

Contributions from direct photons come from two sources, virtual direct photons and conversions of real direct photons in material. The relationship between the real and virtual photon contributions is similar to the relationship between the pion Dalitz decay, $\pi^0 \rightarrow e^+e^-\gamma$, and pions to two gammas, $\pi^0 \rightarrow \gamma\gamma$. This is manifested in a so-called “direct pion”, an imaginary particle implemented in the EXODUS decay generator as a parent particle for these photons. The direct pion is a neutral pion where the invariant p_T spectrum and normalization are chosen so that the spectrum of decay photons from the pion to two gammas matches the spectrum of measured direct photons [46]. The Dalitz decay of the direct pion is the virtual photon contribution. Conversions of real direct photons are estimated using the same technique for the π^0 , scaling by the factor 0.403.

4.1.6 Quarkonia and Drell-Yan

It is possible to complete the cocktail at this point which would result in an electron spectrum from all heavy flavor decays. To make a cleaner interpretation we subtract electrons from quarkonia (J/ψ and Upsilon) and Drell-Yan processes to isolate electrons from open heavy flavor. These decays have a small contribution to the total cross section, but begin to contribute significantly to the background as p_T increases. PHENIX has measured the J/ψ spectra from 0-9 GeV/c in p_T for four different centralities in the 2005 Cu+Cu runs [47]. The data are fit to a Kaplan function,

$$B \frac{1}{2\pi p_T \frac{d^2\sigma}{dp_T dy}} = \frac{A}{[1 + (p_T/B)^2]^n} \quad (4.4)$$

for each centrality and the resulting fits are used as the input parent spectra in EXODUS. The fits are shown below in Figure 4.6. Other analyses ([16],[28]) have used an average of the Kaplan fit and a modified Hagedorn, but as the Kaplan function is the function used in [47] it is the only function used in this thesis.

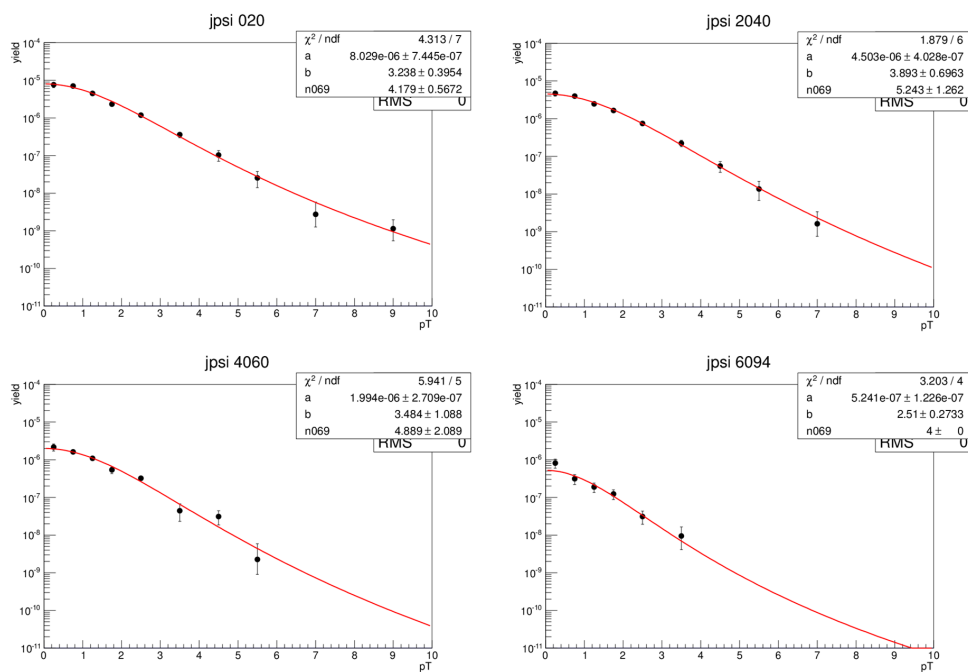


Figure 4.6: Kaplan fit to J/ψ spectra for four centralities. Data from [48].

The J/ψ spectra are only measured for four centrality bins. This thesis includes a 0-10% bin to make a better comparison to the Au+Au data and so a 0-10% bin needed to be created for the J/ψ data. Integrated R_{CuCu} for the J/ψ have been quoted in [47] for ten percent centrality bins. They are as follows:

- $(R_{\text{CuCu}})_{J/\psi 0-10} = 0.4960$
- $(R_{\text{CuCu}})_{J/\psi 0-20} = 0.54445$

Since we do not expect the p_T dependence to change from the 0-10% bin to the 0-20% bin, a 0-10% bin was created by scaling the spectra in the 0-20% bin by the ratio of the integrated yields. The 0-10% bin and the Kaplan fit are shown in Figure 4.7. A MB spectra was not quoted in [47] so one was created by taking the weighted average of the four centrality bins. The newly created MB bin is then also fit to the Kaplan function and is shown in Figure 4.8.

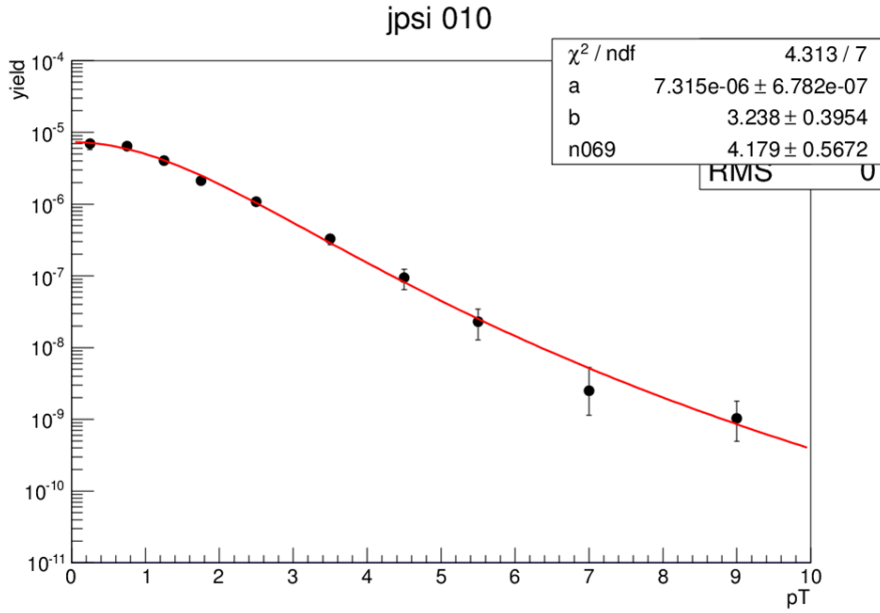


Figure 4.7: Kaplan fit to the 0-10% central J/ψ bin.

The Upsilon has not yet been measured in PHENIX for the Cu+Cu runs and so there is no data fit to use as an input into EXODUS. Instead we

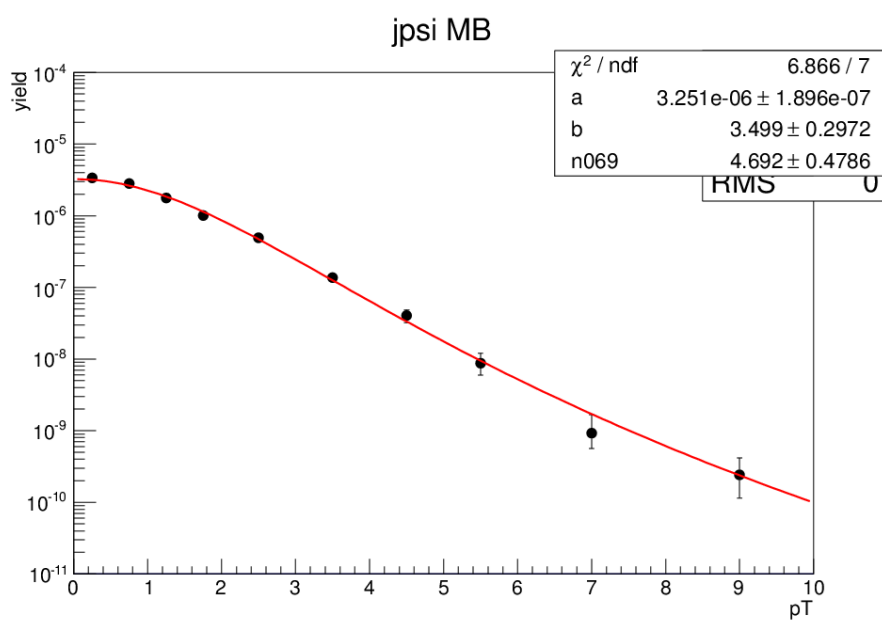


Figure 4.8: Kaplan fit to the MB J/ψ bin.

use an NLO calculation from R. Vogt as the parent distribution [49]. The calculation is done for p+p and so the resultant electron spectra are scaled up by N_{coll} . The Upsilon contribution is small, less than 5% of the background. The Drell-Yan contribution, electrons from the annihilation of quark-antiquark pairs from interacting hadrons, is negligibly small over all p_T , but is included for completeness. It is estimated using a LO calculation from Vogelsang scaled up by N_{coll} [50],[51].

4.1.7 Total cocktail

The total cocktail is the sum of all the above components for each centrality. The resultant cocktail is shown for the MB in Figure 4.9.

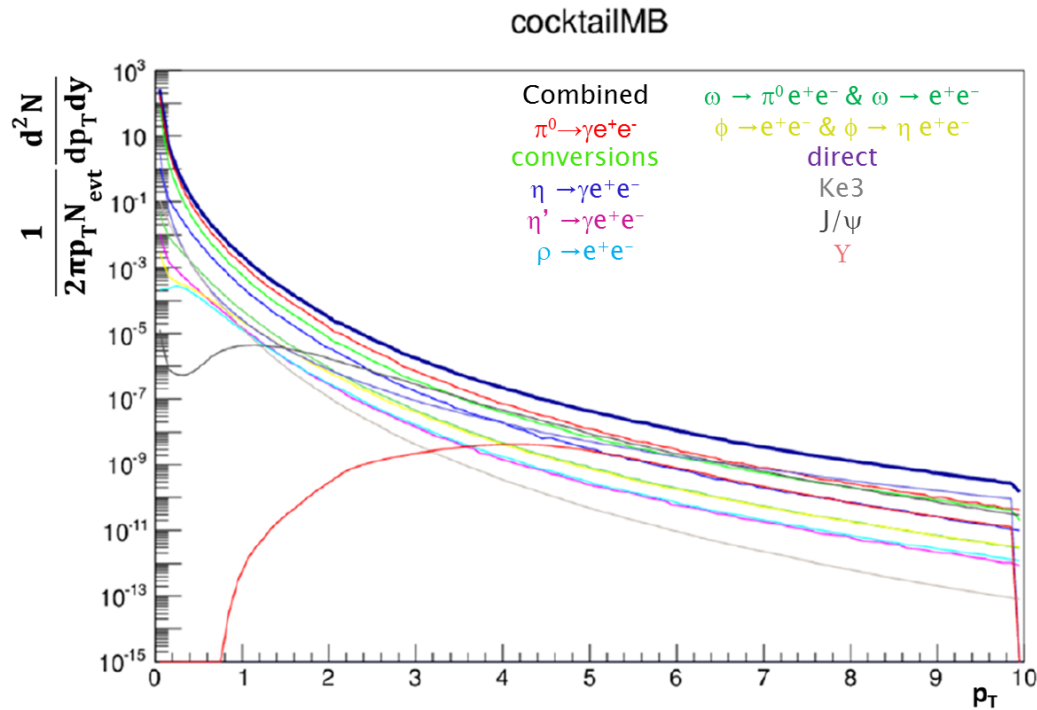


Figure 4.9: The background electron cocktail for MB.

4.2 Converter Analysis

During Run 5 a brass converter was wrapped around the beam pipe to increase the photonic component of the electron spectrum. This increase can be seen in the higher number of electrons per event in Figure 3.2. The known thickness and radiation length of the converter allows us to determine this photonic component. As a cross check for the converter we must make sure that the acceptance did not change between the converter and non-converter runs due to any changes in the detector live area. Figure 4.10 shows $dn/d\phi$ for the converter and non-converter runs. It is clear that they match very well. The inclusive electron yield can be separated into two parts, a photonic yield (N_γ , from conversions and Dalitz decays) and a non-photonic yield ($N_{\text{non}-\gamma}$) and expressed as

$$N_{\text{inc}} = N_\gamma + N_{\text{non}-\gamma} \quad (4.5)$$

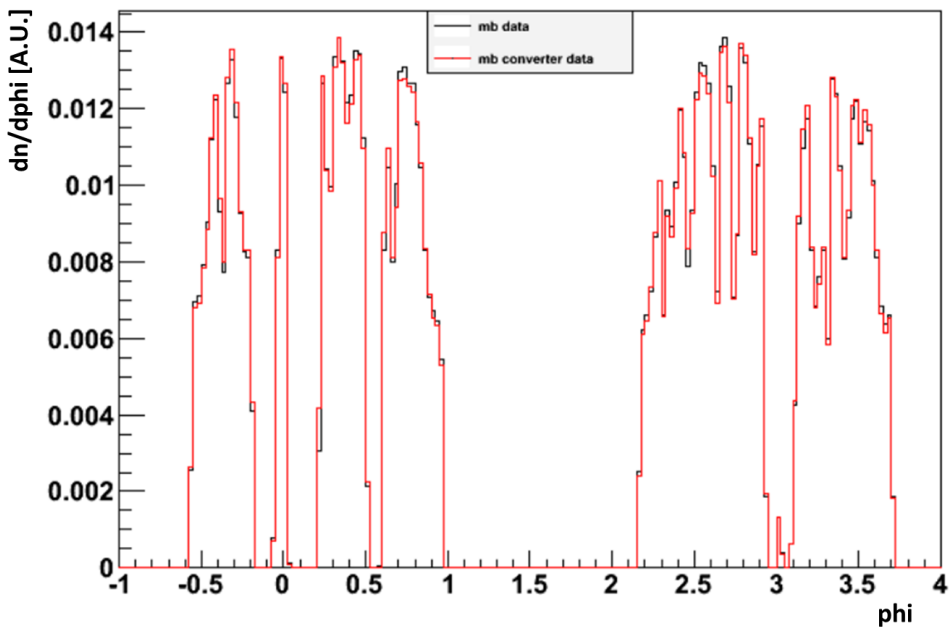


Figure 4.10: $dn/d\phi$ for the converter runs in red and non-converter runs in black.

The converter increases the photonic component by a factor R_γ . There is a small loss, ϵ , of the non-photonic component because of the increase in

mass of the converter. The total yield with the converter installed can then be expressed as

$$N_{\text{inc}}^C = R_\gamma N_\gamma + (1 - \epsilon) N_{\text{non}-\gamma} \quad (4.6)$$

The above equations can then be rearranged to give us the photonic and non-photonic components

$$N_{\text{non}-\gamma} = \frac{R_\gamma N_{\text{inc}} - N_{\text{inc}}^C}{R_\gamma - 1 + \epsilon} \quad (4.7)$$

$$N_\gamma = \frac{N_{\text{inc}}^C - (1 - \epsilon) N_{\text{inc}}}{R_\gamma - 1 + \epsilon} \quad (4.8)$$

where N_{inc}^C and N_{inc} are the measured inclusive spectra with and without the converter installed respectively. The two yields are shown in Figure 4.11. To solve for $N_{\text{non}-\gamma}$, ϵ and R_γ must be found from simulation.

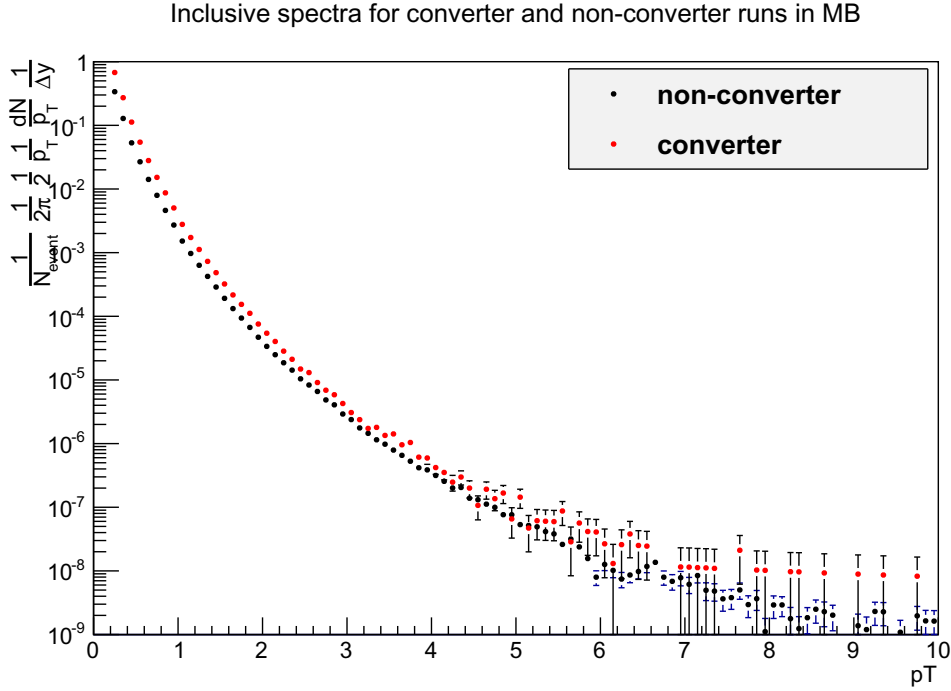


Figure 4.11: Minimum bias inclusive yield for the converter(red) and non-converter (black) runs.

The loss of non-photonic yield due to the converter was determined in

simulation in [52]. It was found to be 2.1% with a systematic error of 25%. R_γ is the increase in the photonic yield due to the presence of the converter. Since the dominant source of photonic background is the neutral pion with the eta having the only other significant contribution, R_γ is calculated separately for each and then combined. A simulation was run in the 2004 p+p analysis to determine R_γ . Since the 2005 Cu+Cu had the same detector setup, it also applies to this analysis. Neutral pions were generated and sent through the simulation chain with and without the converter installed and weighted with a Hagedorn fit to the pion data. The ratio between the two gives R_γ . The same was done for the eta and the two are combined to give the total R_γ which is found to have a slight p_T dependence that is prevalent in the low p_T region and shown in Figure 4.12. Though we don't calculate R_γ specifically

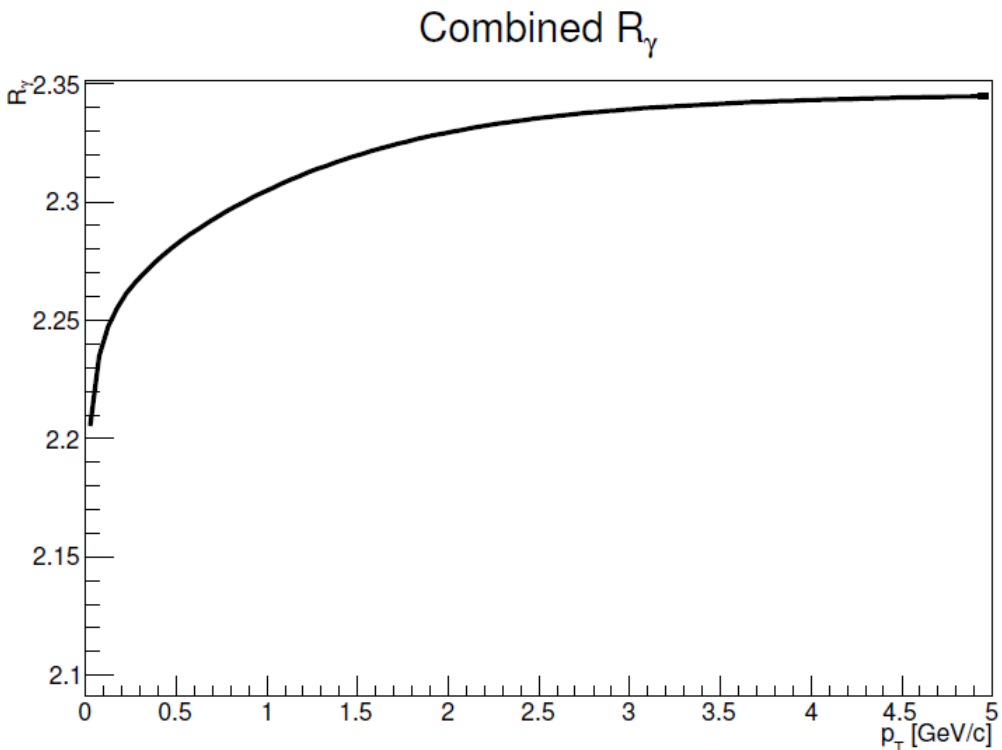


Figure 4.12: The p_T dependence of R_γ .

for this analysis we can do a rough check to make sure the value we are using is appropriate. Using Equations 4.5 and 4.6 we can define a new variable

R_{CN} , defined in Equation 4.9 below, as the ratio of the two.

$$R_{\text{CN}} = \frac{N_{\text{inc}}^C}{N_{\text{inc}}} = \frac{R_\gamma N_\gamma + (1 - \epsilon) N_{\text{non}-\gamma}}{N_\gamma + N_{\text{non}-\gamma}} \quad (4.9)$$

If we plot this ratio, at low p_T the photonic component is dominant and $N_\gamma > N_{\text{non}-\gamma}$. We can then expect that the y-intercept of R_{CN} will be approximately equal to R_γ . R_{CN} is shown in Figure 4.13 for MB and all 5 centralities. It is clear that if you project the slope back to the y-axis that the value will be around 2.3, in rough agreement with the value determined in simulation.

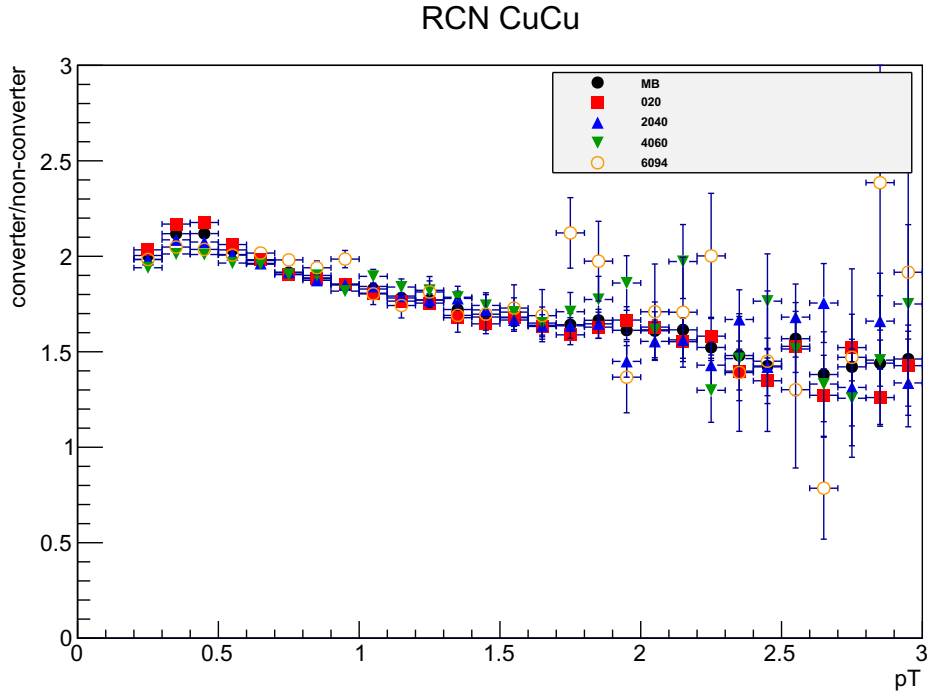


Figure 4.13: R_{CN} for MB and 5 centralities. Y-intercept value is approximately R_γ .

Using these values of ϵ and R_γ the two equations can be solved for the photonic and non-photonic yield. Using the converter method gives the entire photonic background yield of electrons and is important in normalizing the cocktail.

4.3 Comparison of the Two Methods

In theory the photonic cocktail and the photonic yield from the converter method should match. Because the converter method uses data directly it includes all photonic background sources and is the more reliable method. The photonic cocktail is dependent on a number of things, most importantly that the input pion spectra is correct and that we have included all photonic background sources. In the 2005 Cu+Cu run data both of these issues come into play.

It is known that there are thermal photons in the central Au+Au collisions. These photons can convert into electrons and contribute to the photonic background at low p_T . There is currently no way to simulate these photons and so they are not included in the cocktail. It is at most a 20% effect in the central Au+Au yield and so will be much smaller in the Cu+Cu yield, though any contribution from these thermal photons to the photonic background will be found in the photonic yield from the converter method.

The larger effect is the input pion spectra. In previous electron analyses both the charged and neutral pion spectra were used to create an input pion parent spectra for EXODUS. The average of the charged pions extended the input spectra to a lower p_T and helped constrain the Hagedorn fit. The Cu+Cu runs do not yet have a published charged pion spectra and so only the neutral pions were used. The neutral pion spectra begins at 1 GeV/c and is therefore not constrained very well at low p_T .

To combat these two issues we use the photonic yield from the converter to normalize the photonic component of the cocktail. The ratio of the two yields for each centrality is shown in Figure 4.14. The normalization factor increases as we go to more peripheral collisions which is the opposite of what is expected from thermal photons. This indicates that the main issue at hand is the input pion spectra. Though the normalization factors get a bit large, the ratios are flat and we can be reassured that the shape is correct and apply the normalization without worry.

4.3.1 R_{NP}

We would like to make a direct comparison of the converter and cocktail methods in our final result, the nuclear modification factor (defined previously in Equation 6.1 and discussed further in the Results section), but the error bars become quite large with the additional subtraction of the non-photonic

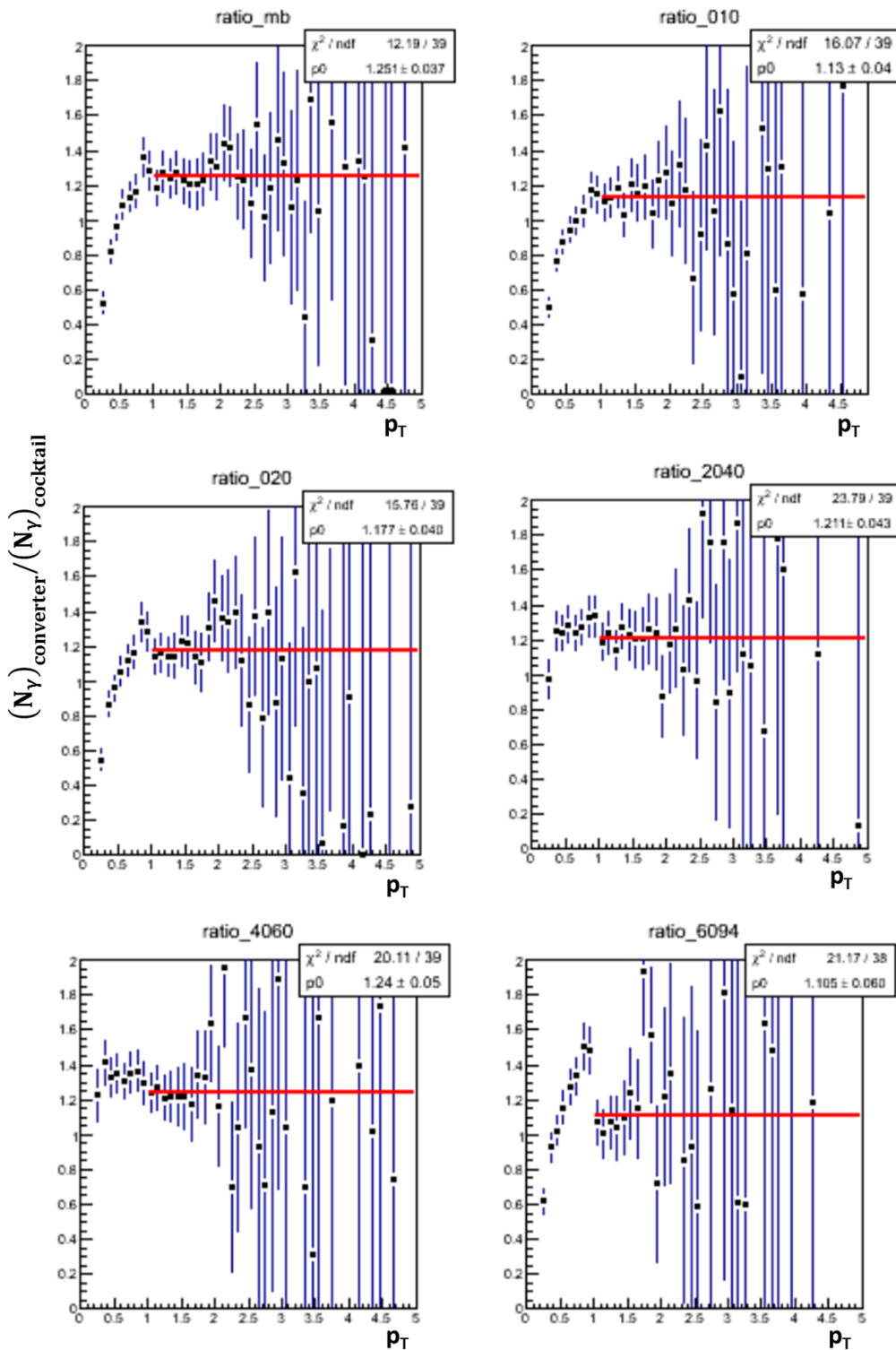


Figure 4.14: The ratio of the photonic spectra as determined by the converter and the photonic cocktail for MB and 78% centralities.

cocktail and the inclusion of the p+p data. Instead a method was devised to compare the two results more directly without the use of the p+p data. Recall Equations 4.5 - 4.9 from the converter analysis. Using those equations we can define a new one:

$$R_{NP} = \frac{N_{non-\gamma}}{N_\gamma}, \quad (4.10)$$

the ratio of the non-photonic and photonic components of the inclusive spectra. R_{NP} is not exclusive to the converter analysis and can be calculated for the cocktail analysis as well. R_{NP} will lead to R_{CuCu} , the nuclear modification factor for non-photonic electrons in Cu+Cu, as shown in Equation 4.11.

$$(R_{CuCu,e})_{non-\gamma} = \frac{R_{NP,CuCu}}{R_{NP,pp}} * (R_{CuCu,e})_\gamma \quad (4.11)$$

where $R_{NP,pp}$ is from the p+p analysis [52] and $R_{CuCu,\gamma}$ is the nuclear modification factor for photonic electrons in Cu+Cu calculated in simulation. Since neither the $R_{NP,pp}$ nor $R_{CuCu,\gamma}$ will be different whether we calculate $R_{NP,CuCu}$ in the cocktail or converter methods, we can convince ourselves that if the $R_{NP,CuCu}$ of the two methods agree, so will $(R_{CuCu,e})_{non-\gamma}$. R_{NP} for the converter method is calculated by dividing Equations 4.7 and 4.8. In the cocktail method, the cocktail is subtracted from the inclusive spectra to leave just the non-photonic electrons which are then divided by the photonic cocktail. The results for MB and 5 centralities are shown in Figure 4.15. Unfortunately a full comparison cannot be made over the entire p_T range. Below 1 GeV/c the cocktail analysis is not constrained and above 3 GeV/c the statistics of converter analysis do not allow for a meaningful comparison. However, we can see that the two methods agree very nicely in the overlap region where both methods are reliable.

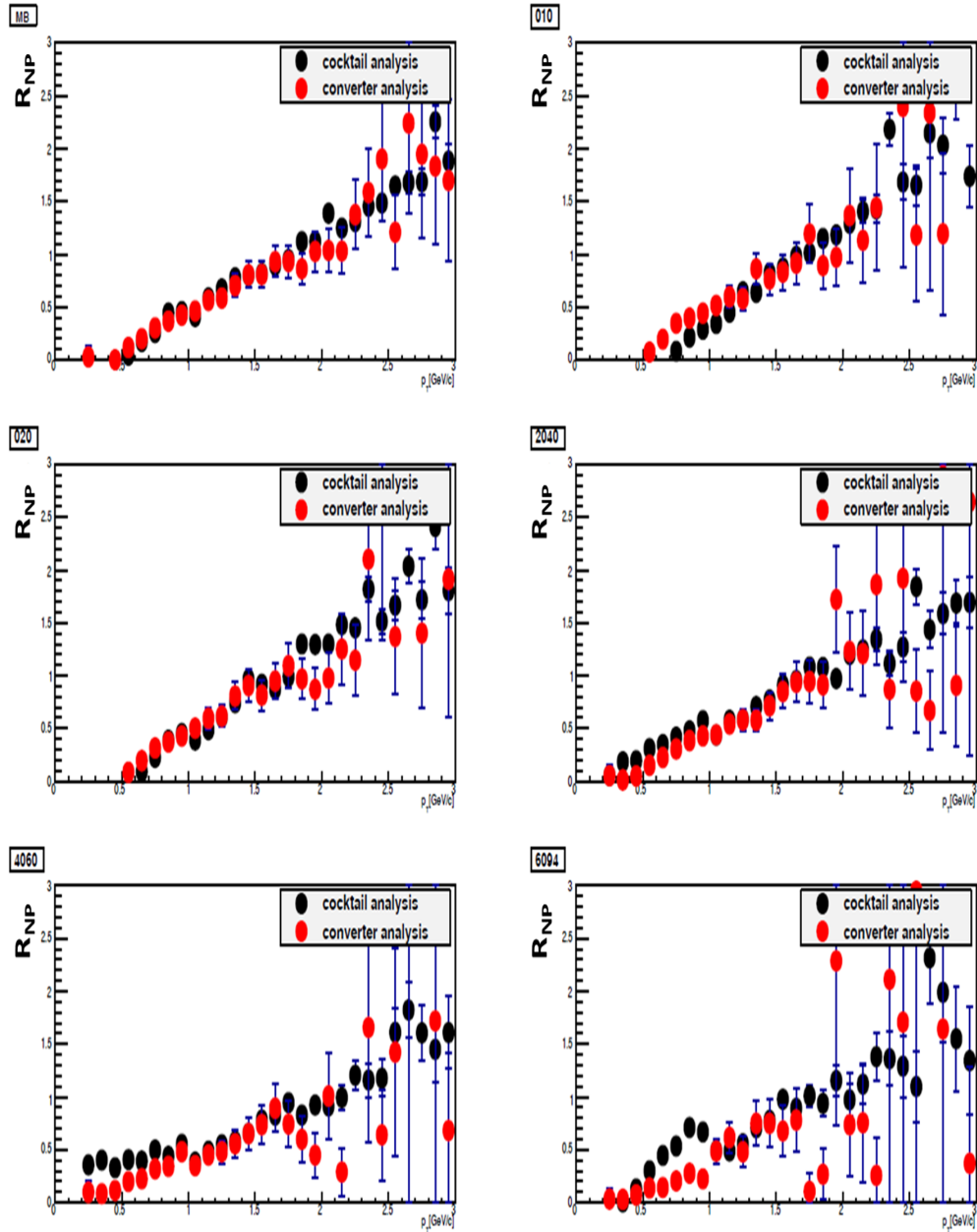


Figure 4.15: R_{NP} for the cocktail method (black) and converter method (red) for MB and 5 centralities.

Chapter 5

Systematic Error Estimation

In this chapter I will discuss how the systematic errors were determined for this analysis.

5.1 Inclusive Yield

First are the errors on the inclusive yield. They are a combination of three parts, the error on the run group correction, electron identification and the geometric matching. For the ERT analysis there is an additional error that comes from determining the trigger efficiency.

5.1.1 Run Group Correction

It was discussed earlier that in the minimum bias triggered sample run groups are not treated separately since there is no discernible difference between the two. There are still fluctuations run to run however and this is included in a systematic error by the uncertainty on the determination of $\langle N_e/N_{\text{evt}} \rangle$. This error was found to be 0.6% and so a systematic error of 1% is assigned.

5.1.2 Electron Identification

The uncertainty on identifying electrons comes from the inability to perfectly model the detector in simulation. It is estimated by repeating the acc*eff

calculation for tighter and looser electron cuts. These cuts are shown in Table 5.1.

Parameter	Loose Cuts	Standard Cuts	Tight Cuts
n1	≥ 2	≥ 5	≥ 5
disp	<i>none</i>	$< \text{none}$	< 5.0
prob	> 0.001	> 0.01	> 0.2

Table 5.1: The sets of electron ID parameters used to evaluate systematic errors on the acc×eff correction.

Each acc×eff correction is applied to an inclusive spectra made with the same cuts. To the extent that the simulation reproduces the data correctly all three spectra should be the same. The ratio is taken between the standard cuts and the tight and loose cuts respectively. Figure 5.1 shows the spread levels around 6% and so that is taken as the systematic error.

5.1.3 Geometric Matching

Mismatching in the detector acceptance in the simulation and data is an additional uncertainty. To determine this uncertainty, the $dN/d\phi$ yield is integrated over the west arm for both the data and the simulation. The simulation is then normalized to have the same integral as the data in the west arm. The integral of the two in the east arm are then compared to each other and the difference is the systematic error. In this analysis the difference was found to be 4%.

5.1.4 Trigger Efficiency

The ERT data set is only used in the high p_T region where the trigger efficiency is at the plateau value and so the only error is due to the determination of the trigger plateau. Figure 3.11 shows the ratio between the ERT after correction and the MB data sets. As discussed previously, though they are approximately 10% different, the ratio is flat and the resulting constant value is used as an additional correction. The error on the constant value is taken

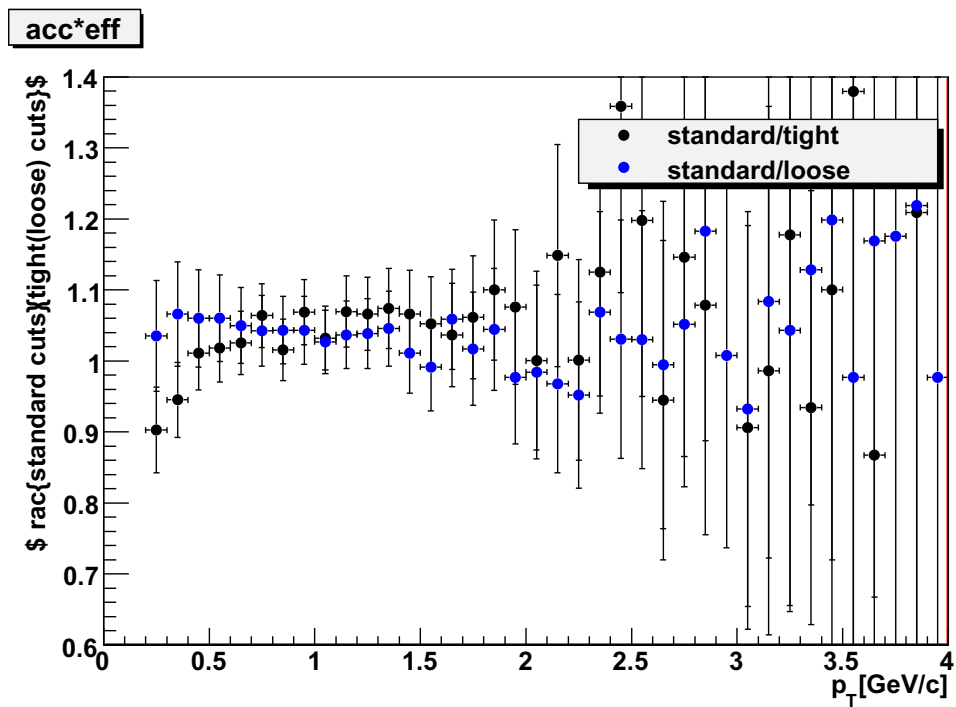


Figure 5.1: Loose, standard and tight eid cuts. Spread is systematic error on electron identification.

to be the systematic error of the trigger correction, conservatively estimated as 2%.

5.1.5 Total Inclusive Systematic Error

The systematic errors are shown in Table 5.2.

Run Group Correction	1%
Acceptance*Efficiency	6%
Geometric Matching	4%
Trigger Efficiency	2%

Table 5.2: Systematic errors on the inclusive spectrum.

These yield a total systematic error of 7.3% on the inclusive MB yield and 7.5% on the inclusive ERT yield.

5.2 Cocktail

The dominant systematic error on the cocktail comes from the uncertainty on the Run 5 Cu+Cu pion data that is used as the input parent spectra for all of the light mesons. The pion data are moved up and down by their systematic errors and refit to the modified Hagedorn function. These are then input into the decay generator as input parent spectra. The output decay spectra become the upper and lower spread of the systematic error.

For the other light mesons, the central values of the decay spectrum are moved up and down by the uncertainty on the meson/ π ratios show in Table 4.1. The systematic error on the conversion yield is found by scaling the conversion probability up and down by 10%. This gives a conservative estimate on the amount of conversion material within PHENIX and has been used for previous analyses. The direct photon uncertainty is found using the same method as in [46] where the direct photon measurement is used. The Ke3 is assigned a 50% error as in previous analyses.

The systematic error on the J/ψ spectra is done in the same manner as the pions. Namely moving the points up and down by their systematic errors and refitting. However, the 60-94% J/ψ bin only has points at low p_T and therefore the fit is not constrained well at higher p_T . The result is an unreasonably

large systematic error for the cocktail at the higher p_T . To combat this the 60-94% bin is treated a little differently. Instead of letting all parameters of the Kaplan function float, the exponent is fixed to the value from the fit to the 60-94% points. The fit to the upper and lower systematic points have the same exponent. Figure 5.2 shows all the systematic errors for the minimum bias cocktail. The errors are added in quadrature and shown in black. The upper and lower errors are symmetric enough that the average is taken to determine the final systematic error.

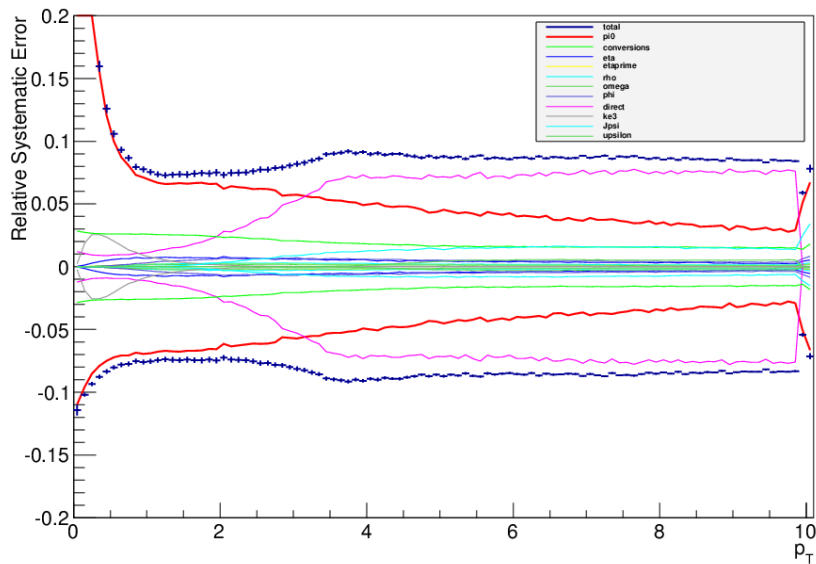


Figure 5.2: Minimum Bias cocktail systematic errors.

5.3 Converter

The systematic error on the converter analysis comes from two sources, the already described systematic error on the inclusive spectra and the uncertainty derived from extracting a non-photonic (and photonic) spectra from the converter analysis. These errors are independent and are added in quadrature. Accuracy in the converter method relies on the reproduction of the converter

in simulation. This is described in detail in [52] and again in [53]. This analysis uses the Run 4 R_γ and ϵ values and thus the respective errors of 2.7% and 25% found in [52] apply here. The final error comes from the difference in detector live area between the converter and non-converter runs. This is calculated the same way as the geometric matching. The $dN/d\phi$ distributions are normalized to have the same integral in the west arm and then that normalization is applied to the east arm. The difference between the integrals is 0.2% and so a conservative error of 1% is taken as the systematic error on N_{inc}^C . R_γ , ϵ and N_{inc}^C are moved up and down by their systematic errors and the effect on the spectra is calculated and then added in quadrature. The systematic error on the converter analysis is shown in Figure 5.3 for the MB.

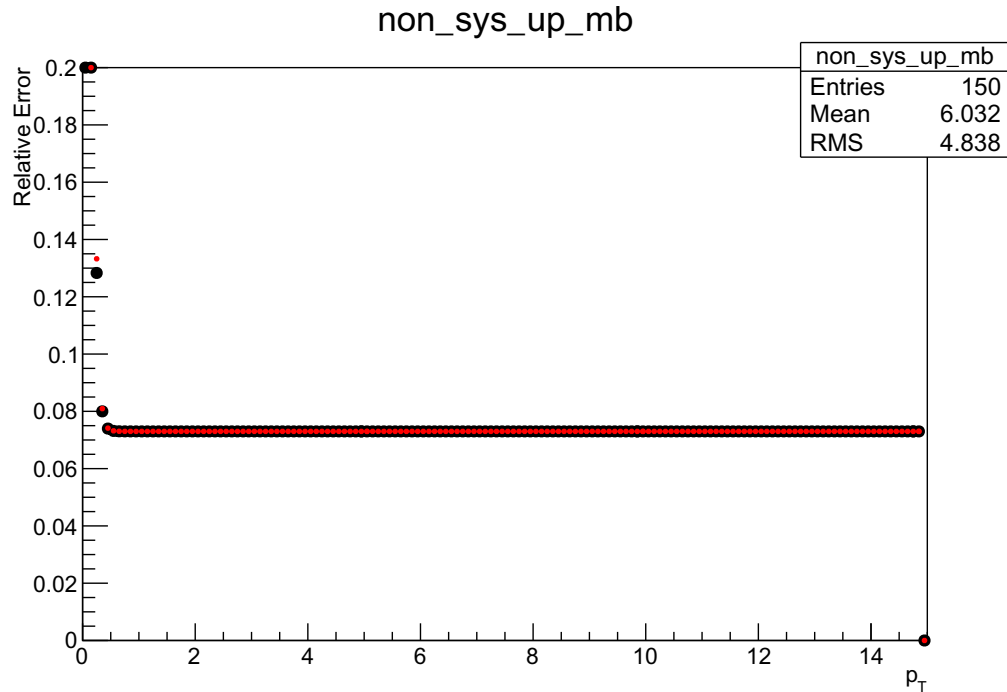


Figure 5.3: Minimum Bias converter systematic errors.

Chapter 6

Results and Discussion

6.1 Heavy Flavor Spectra

The invariant yield of electrons from heavy flavor decays (heavy flavor spectra) are found by a combination of the cocktail and converter methods. Using the cocktail method the photonic cocktail of background sources (normalized to the converter) is subtracted from the inclusive spectra along with the additional non-photonic background sources, leaving only electrons from open heavy flavor. Since the statistical errors on the cocktail are negligible, the statistical errors are taken from the inclusive yield. The systematic errors are those of the inclusive yield and cocktail subtraction added in quadrature.

In the low p_T region the signal to background ratio is small and the relative error on the inclusive yield is enhanced by subtracting a large background. As was mentioned in a previous section the photonic cocktail is heavily dominated by the pions at low p_T for which we do not have data below 1 GeV/c. Instead we use the converter method below 1 GeV/c. The heavy flavor spectra is found via the converter method by solving Equation 4.8 and subtracting the non-photonic cocktail. The systematic error is the quadrature sum of the inclusive error, the converter error and the error on the non-photonic cocktail.

The invariant yields for heavy flavor electron are shown in Figure 6.1 for the MB and five different centralities. The heavy flavor electron yield in p+p collisions is fit to a spectral shape take from the FONLL calculation [54] and is scaled up by N_{coll} and compared to each centrality bin. Modification to the spectra in different centralities can be seen particularly in the most central, 0-10%, bin and the most peripheral, 60-94% bin. To better see this modification

we calculate the ratio between the points and the curves in Figure 6.1.

6.2 Nuclear Modification Factor

As previously defined the nuclear modification factor is

$$R_{\text{AA}} = \frac{dN_{\text{AA}}}{\langle N_{\text{coll}} \rangle \times dN_{\text{pp}}} \quad (6.1)$$

and is found by dividing the Cu+Cu heavy flavor spectra by the N_{coll} scaled p+p heavy flavor spectrum. The p+p reference is used from [16]. Below 1.6 GeV the p+p reference is divided point by point. The statistical(systematic) errors are the quadrature sum of the Cu+Cu and p+p statistical(systematic) errors. Above 1.6 GeV the p+p data is consistent with a pQCD shape and the fit is used scaled by N_{coll} . The form of the fit function is

$$Y(p_T) = \frac{A}{(p_T + B)^n} \quad (6.2)$$

which was used to fit the p+p heavy flavor spectrum in [16]. The fit was used to calculate R_{AuAu} [16] and R_{dAu} [28] and so I have also used it to calculate R_{CuCu} . The statistical errors are taken to be those of the Cu+Cu heavy flavor spectra and the statistical error on the p+p fit is used to estimate the systematic error on R_{CuCu} . The systematic error on R_{CuCu} is the quadrature sum of the Cu+Cu systematic error and the statistical uncertainty on the fit.

Finally, the global scaling uncertainty is the quadrature sum of the global uncertainty on the p+p spectra and the error in the trigger bias and N_{coll} [33]. Figures 6.2 - 6.7 shows the R_{CuCu} for MB and five centralities. Figure 6.3, the 0-10% most central bin, shows a hint of suppression in the mid p_T region. This is unsurprising since this bin is in the N_{coll} region where there is suppression seen in the Au+Au results. In the same p_T region in Figure 6.4, the Cu+Cu 0-20% data is systematically lower than the p+p but still consistent within the large systematic errors. The three most peripheral bins in Figures 6.5 - 6.7 show clear enhancement. This is different from what was seen in the Au+Au data [16]. It is, however, similar to the results for the d+Au data [28].

This shift from enhancement in the peripheral bins to the suppression in

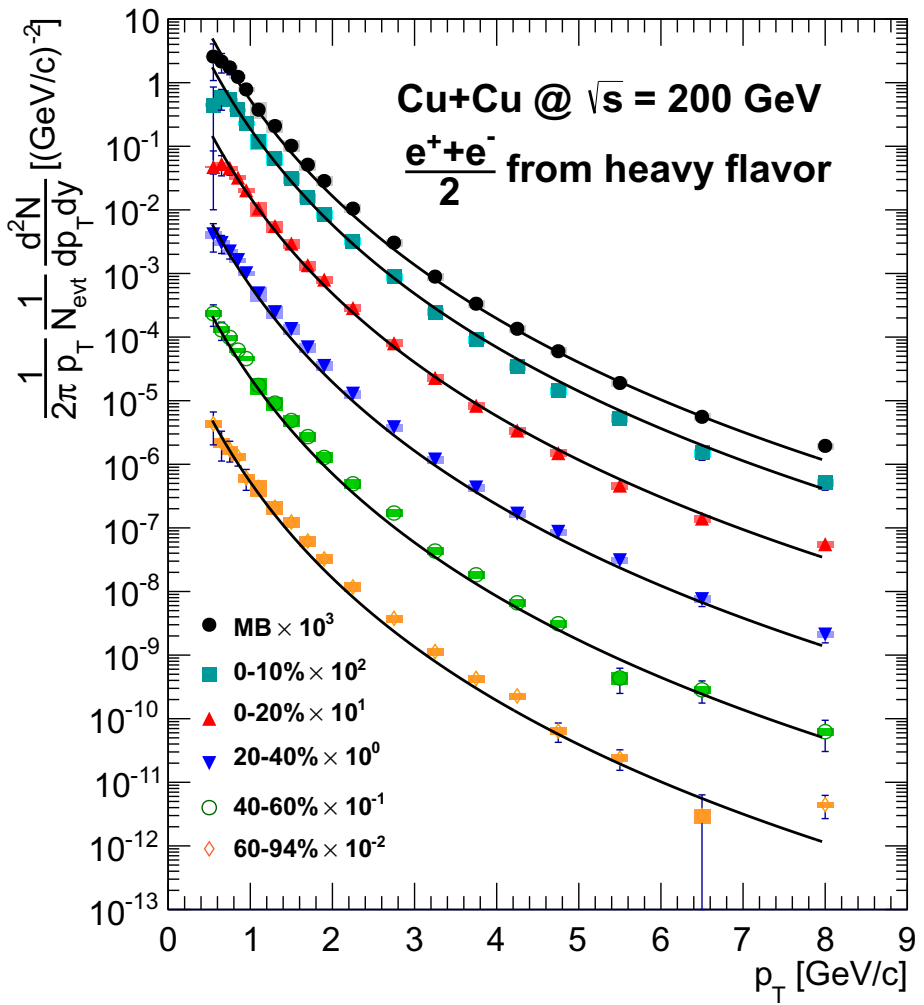


Figure 6.1: Yield of electrons from open heavy flavor.

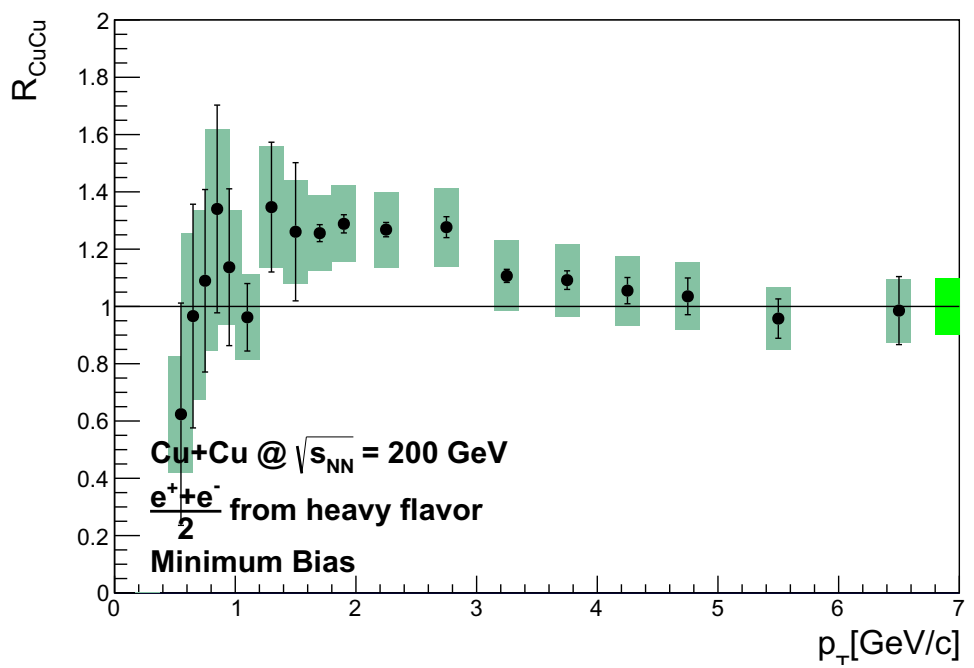


Figure 6.2: Nuclear modification factor for minimum bias collisions.

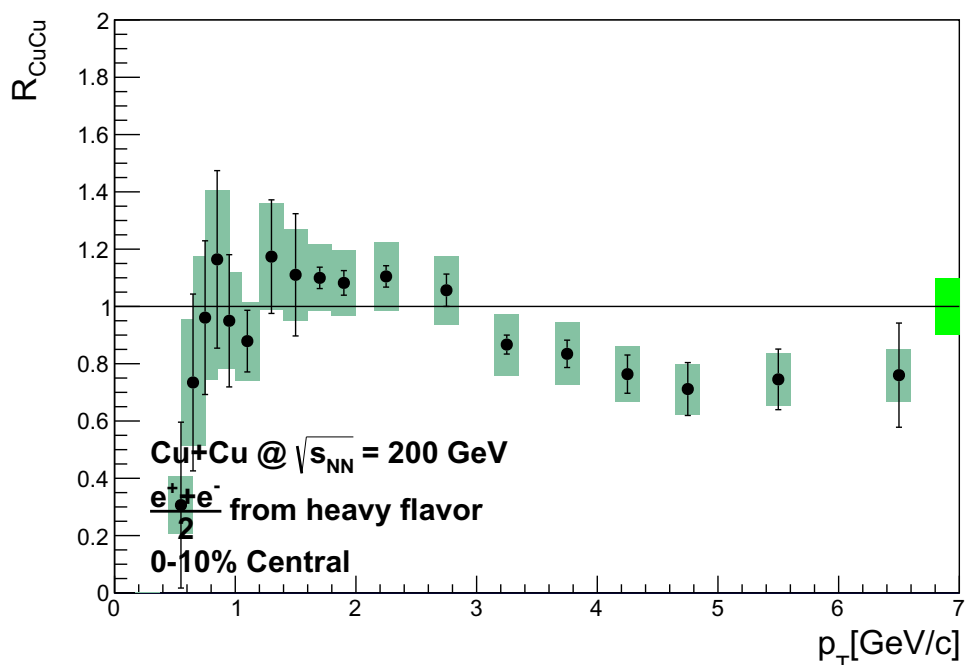


Figure 6.3: Nuclear modification factor for 0-10% central collisions.

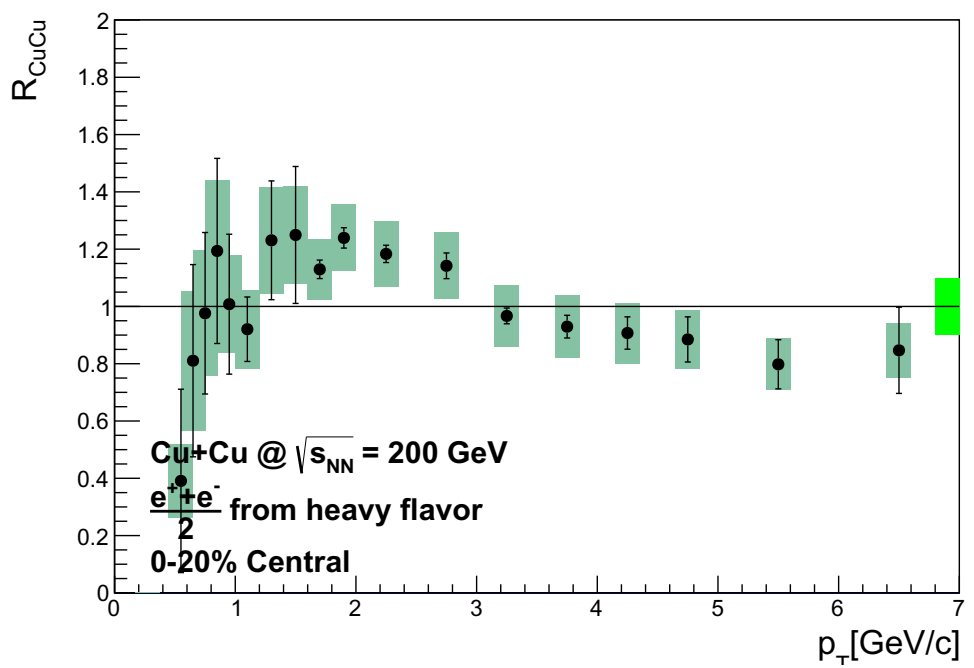


Figure 6.4: Nuclear modification factor for 0-20% central collisions.

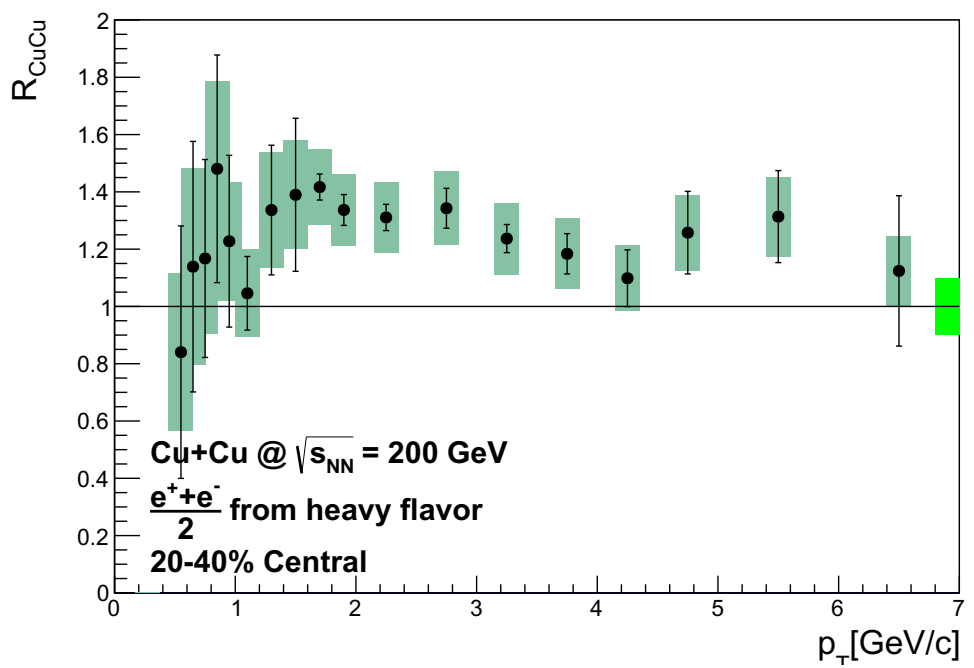


Figure 6.5: Nuclear modification factor for 20-40% collisions.

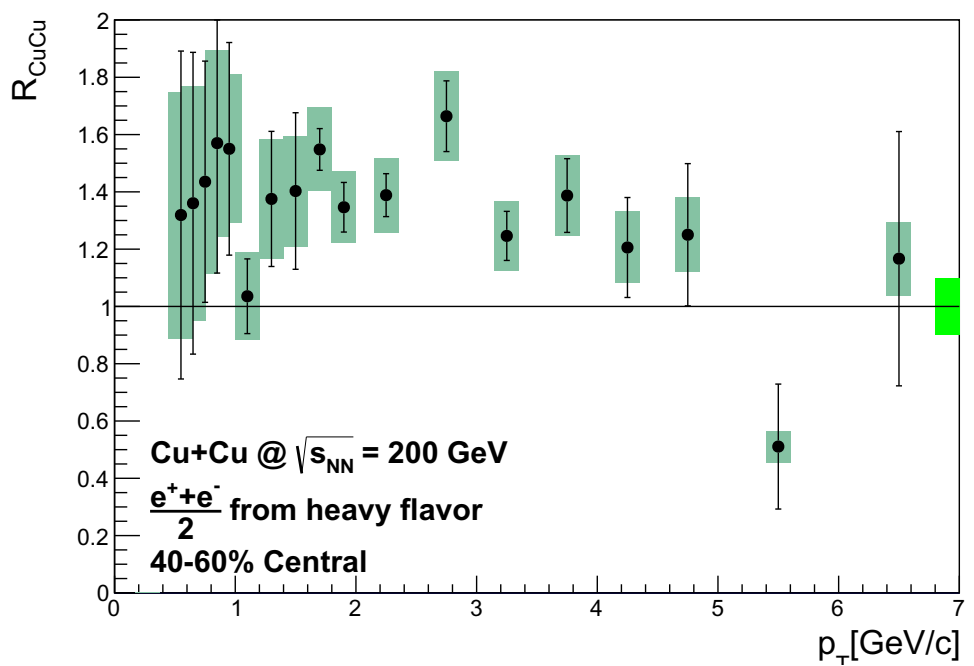


Figure 6.6: Nuclear modification factor for 40-60% collisions.

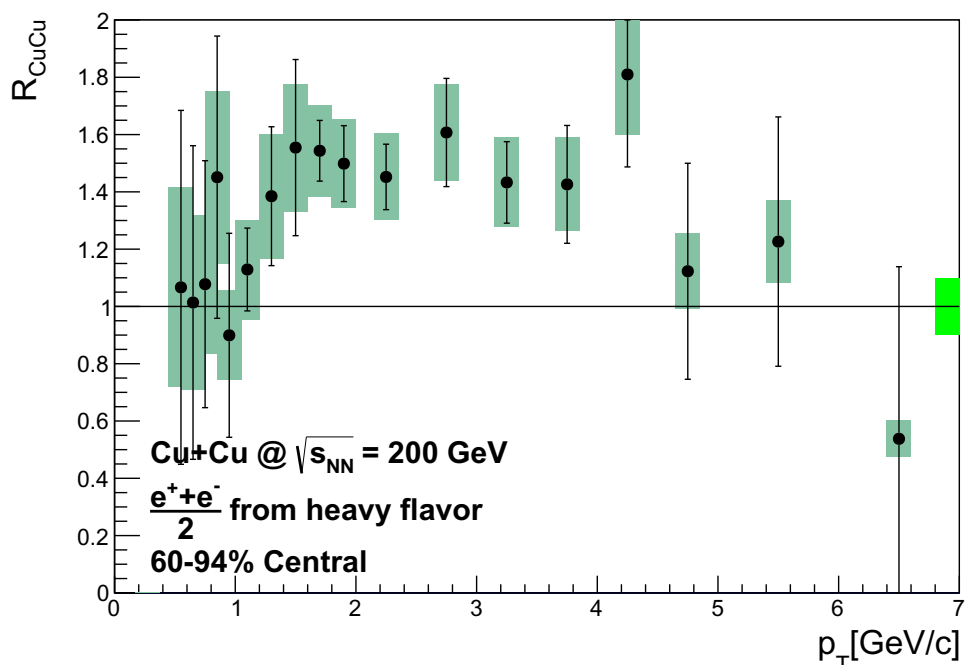


Figure 6.7: Nuclear modification factor for 60-94% central collisions.

the most central can be clearly shown in the factor R_{CP} , defined as

$$R_{\text{CP}} = \frac{(R_{\text{CuCu}})_{\text{central}}}{(R_{\text{CuCu}})_{\text{peripheral}}} = \frac{(dN_{\text{CuCu}})_{\text{central}}}{(dN_{\text{CuCu}})_{\text{peripheral}}} \times \frac{\langle N_{\text{coll}} \rangle_{\text{peripheral}}}{\langle N_{\text{coll}} \rangle_{\text{central}}}. \quad (6.3)$$

The most peripheral bin, 60-94%, is used as the baseline for the R_{CP} calculation. Figure 6.8 shows R_{CP} for the four most central bins. The most peripheral bin is excluded since the R_{CP} is just one. You can clearly see the dramatic difference as you move from the 0-10% bin at the top left to the 40-60% bin at the bottom right of Figure 6.8.

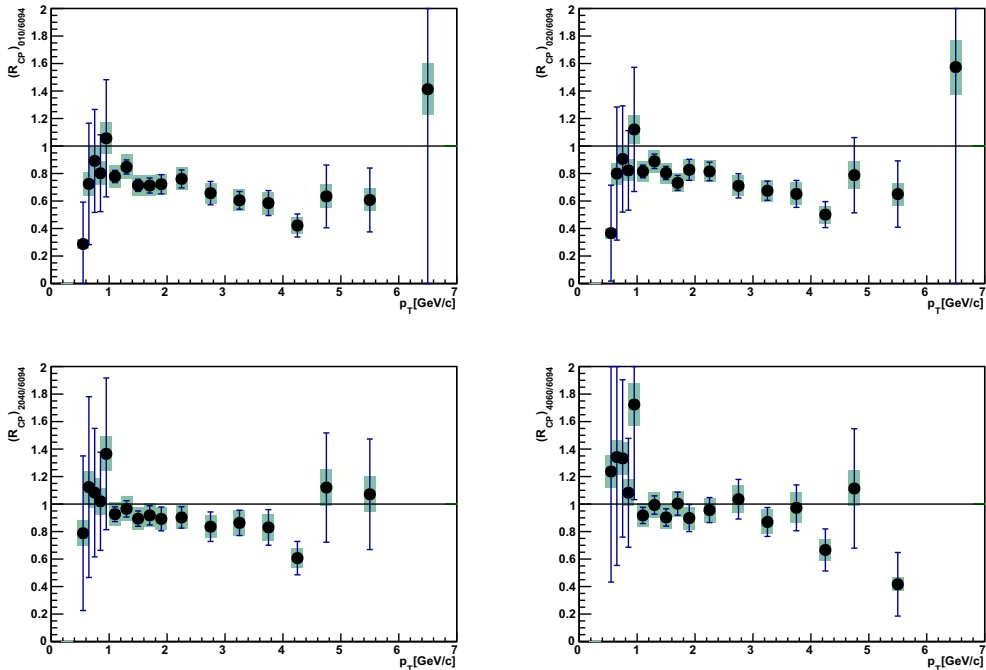


Figure 6.8: R_{CP} for four centralities.

In Figure 6.9 a direct comparison is made between the Cu+Cu and Au+Au data in similar N_{coll} regions. R_{AuAu} 20-40% ($N_{\text{coll}} \sim 296$) and R_{CuCu} 0-10% ($N_{\text{coll}} \sim 182$) are compared on the top of Figure 6.9. Though there is a large difference in the average N_{coll} they are consistent within error bars. Since the Cu+Cu data is of a lower average N_{coll} one can imagine that the suppression would increase if we could probe a higher N_{coll} region. The bottom panel of Figure 6.9 is the comparison of the 40-60% ($N_{\text{coll}} \sim 91$) R_{AuAu} and the 0-20% ($N_{\text{coll}} \sim 152$) R_{CuCu} . Here the average N_{coll} s are more comparable and the two

data sets match up very well.

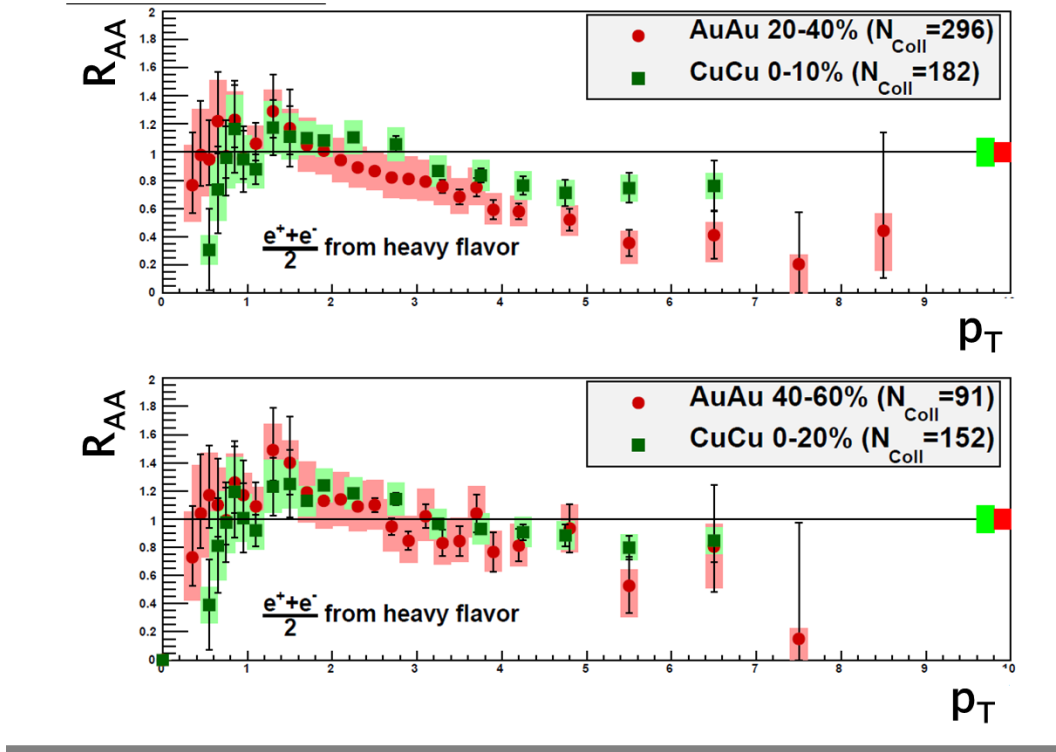


Figure 6.9: Top: $R_{\text{AuAu},20-40}$ and $R_{\text{CuCu},0-10}$. Bottom: $R_{\text{AuAu},40-60}$ and $R_{\text{CuCu},0-20}$.

Figure 6.10 shows the comparison of $R_{d\text{Au}}$ and R_{CuCu} of similar average N_{coll} . The N_{coll} values are much closer in this comparison and the two systems agree very well within the uncertainties.

The different nuclear effects can really be seen by comparing the most central bins of all three systems. Figure 6.11 shows the 0-20% $R_{d\text{Au}}$ bin in blue, the 0-10% R_{CuCu} in green and the 0-10% R_{AuAu} in red. There is a clear enhancement in the d+Au system which disappears as the system size increases to a slight suppression in the central Cu+Cu and finally, a large suppression in the most central Au+Au bin.

A better way to describe this is by comparing R_{AA} vs N_{coll} for the d+Au, Cu+Cu and Au+Au. The average R_{AA} is taken in two p_T regions for each centrality in the three systems and plotted versus the average N_{coll} . In Fig-

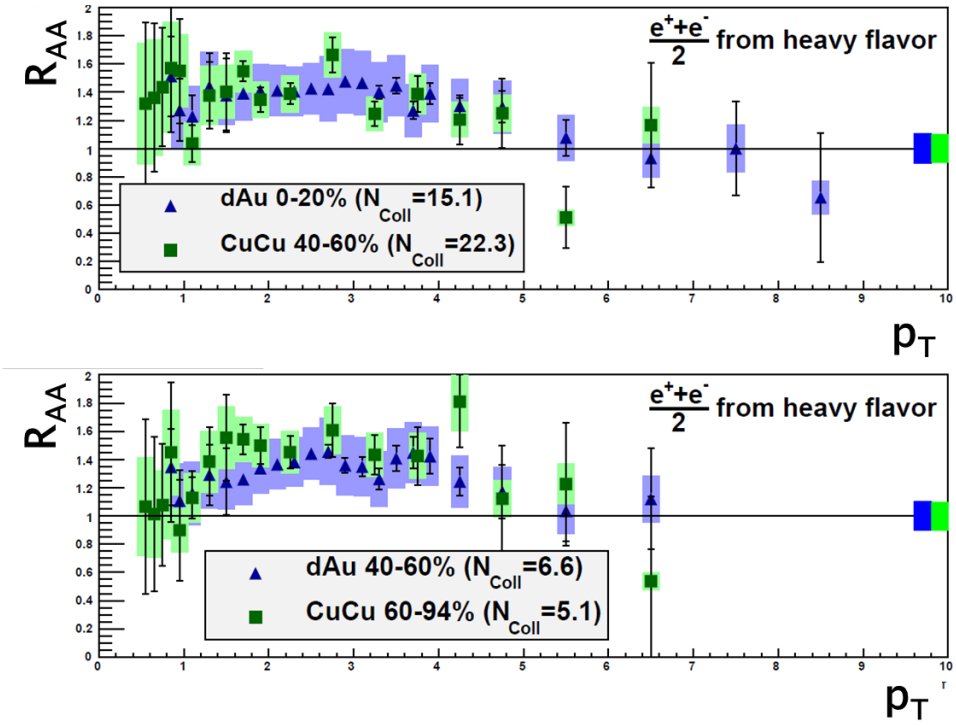


Figure 6.10: Top: $R_{\text{dAu},0-20}$ and $R_{\text{CuCu},40-60}$. Bottom: $R_{\text{dAu},40-60}$ and $R_{\text{CuCu},60-94}$.

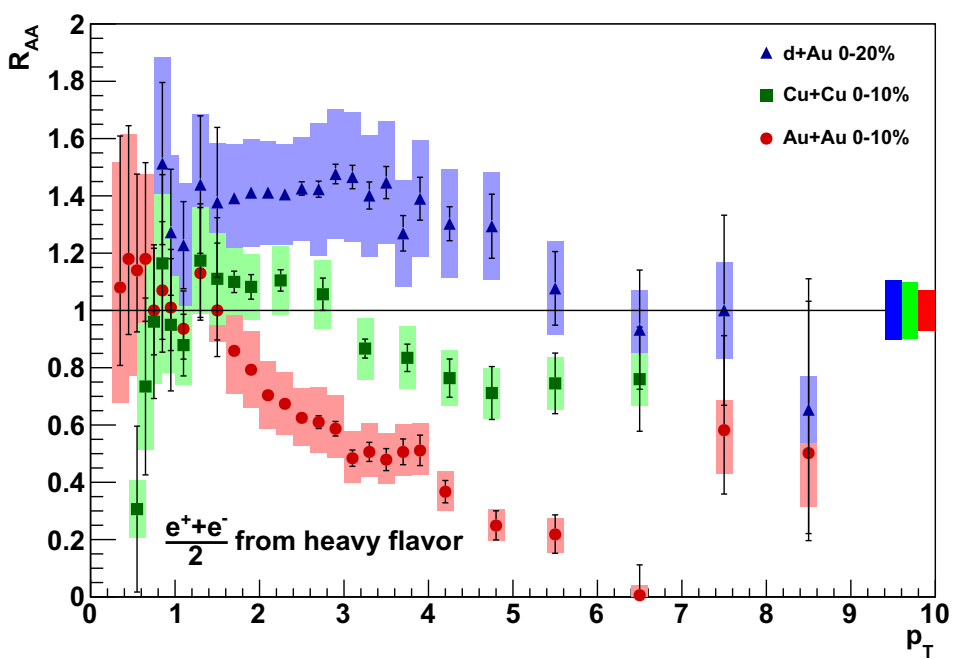


Figure 6.11: Blue: $R_{d\text{Au},0-20}$, green: $R_{\text{Cu}\text{Cu},0-10}$, red: $R_{\text{Au}\text{Au}}$.

ure 6.12 the average R_{AA} between 1-3 GeV/c in p_T is plotted versus the average N_{coll} for 5 centralities in Au+Au, 5 centralities in Cu+Cu and 4 centralities in d+Au. The systematic errors are the average of the systematic error for each of the p_T bins in the average. The horizontal error bars are the errors on the average N_{coll} values. The p_T range between 1-3 GeV/c is where most of the enhancement is seen in the Cu+Cu and d+Au systems and the signal to background has increased. Figure 6.13 is the average R_{AA} between 3-5 GeV/c in p_T . This p_T range was chosen to showcase the suppression seen in the central Cu+Cu and the Au+Au and where the statistics are sufficient.

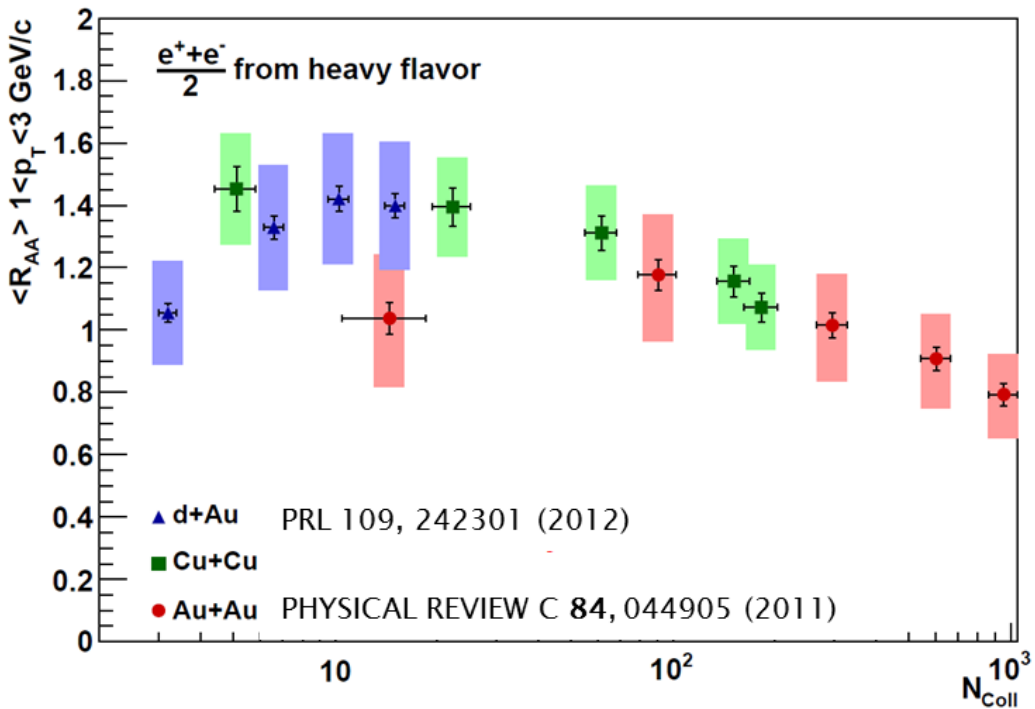


Figure 6.12: Average R_{AA} between 1-3 GeV/c in p_T as a function of N_{coll} .

The same exercise can be done as a function of N_{part} which would describe the rate of soft bulk production and would be a better representation of energy loss, whereas N_{coll} is a measure of the hard scattering. The average R_{AA} vs N_{part} for the same two p_T ranges are shown in Figures 6.14 and 6.15. There are arguments for both variables and so both are shown for completeness.

Though the error bars are large, there seems to be a hint of a trend as we move from the cold nuclear matter effects in the d+Au system and the peripheral Cu+Cu to where the hot medium begins to take over in the central

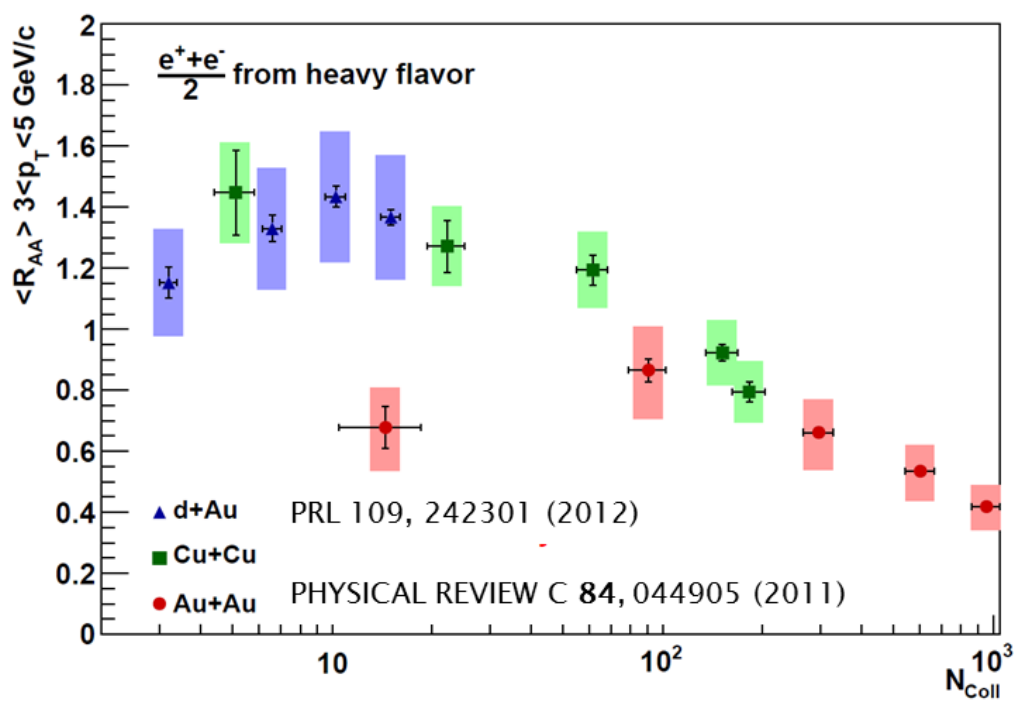


Figure 6.13: Average R_{AA} between 3-5 GeV/c in p_{T} as a function of N_{coll} .

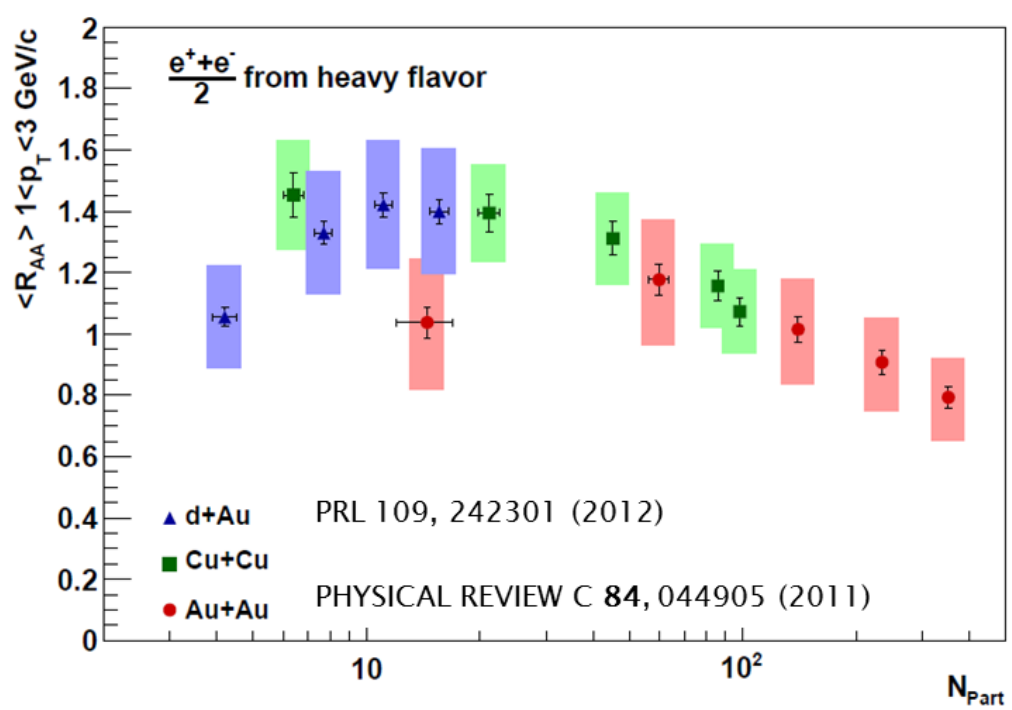


Figure 6.14: Average R_{AA} between 1-3 GeV/c in p_{T} as a function of N_{part} .

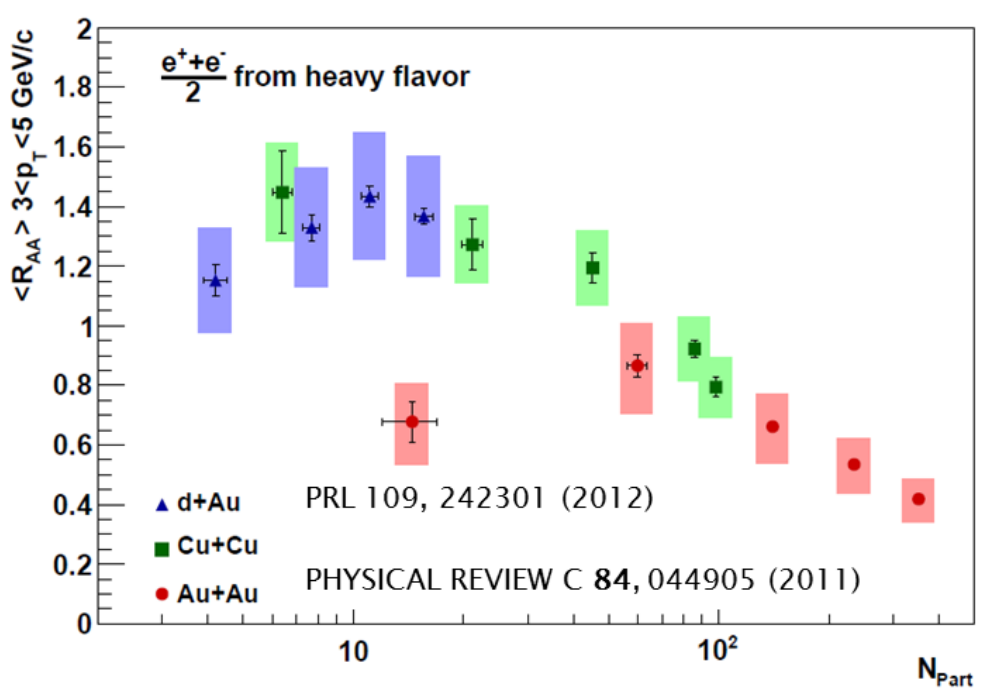


Figure 6.15: Average R_{AA} between 3-5 GeV/c in p_{T} as a function of N_{part} .

$\text{Cu}+\text{Cu}$ and $\text{Au}+\text{Au}$. This is very clear in Figures 6.13 and 6.15. The large enhancement in $\text{d}+\text{Au}$ and a similar enhancement in peripheral $\text{Cu}+\text{Cu}$ seem to suggest that the $\text{p}+\text{p}$ is not the proper baseline for the $\text{Cu}+\text{Cu}$ or $\text{Au}+\text{Au}$ data. There is a large effect that occurs to modify the charm and bottom baseline. The $\text{d}+\text{Au}$ could be the baseline for $\text{Au}+\text{Au}$ but there is no $\text{d}+\text{Cu}$ data to provide a baseline for the $\text{Cu}+\text{Cu}$ data.

The heavy flavor electron R_{CuCu} can also be compared to the R_{CuCu} for the π^0 as was shown previously in Figure 1.5 for $\text{d}+\text{Au}$ and $\text{Au}+\text{Au}$. The two are plotted in Figure 6.16. The heavy flavor electrons do not reach the level of suppression of the neutral pions, though the electron p_T range is limited. This might also suggest that the charm and bottom baseline have a modification that is not seen in the light mesons.

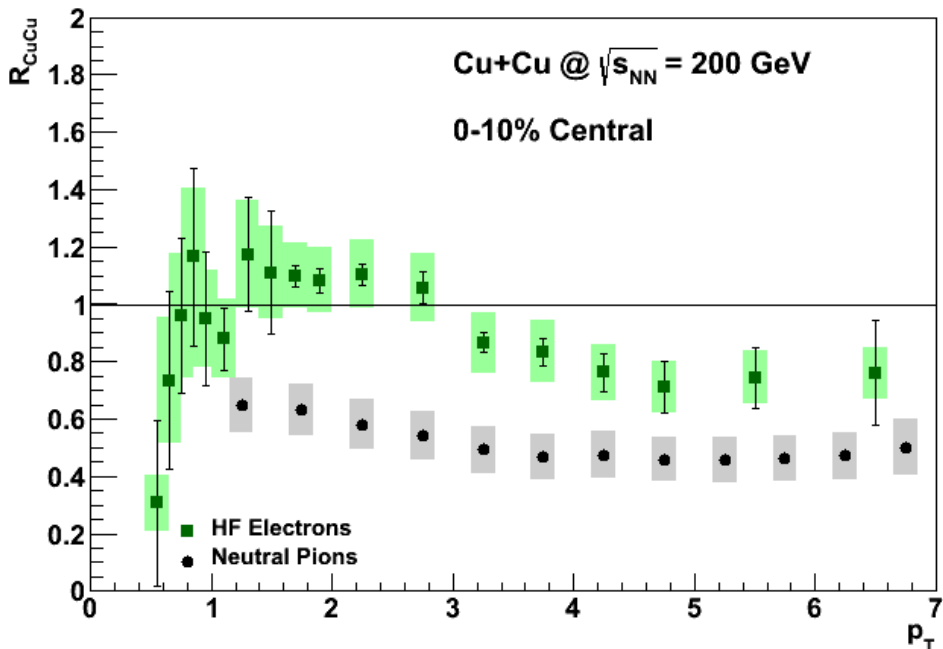


Figure 6.16: R_{CuCu} for π^0 ([42]) and e^\pm_{HF} .

6.3 Comparison to Theory

In this section different theory calculations are discussed and compared to the data. There are few theories that currently compare to the $\text{Cu}+\text{Cu}$ data,

so results will be mainly shown for the Au+Au results with discussion on the implication for the Cu+Cu results.

6.3.1 Partonic Energy Loss

Before the first heavy flavor results at RHIC, predictions were made about the energy loss in the hot medium [6]. Radiative energy loss was thought to be the dominant contribution to the heavy quark energy loss. With small-angle gluon radiation suppressed (the “dead cone” effect) the heavy quarks were predicted to lose less energy in the medium than the light quarks [6]. As the Au+Au data has shown the suppression levels are about the same, and it is now clear that radiative energy loss is insufficient on its own. Collisional energy loss has also been added to the models without much success. To help resolve the discrepancy between the expected suppression and what is actually seen in the Au+Au data, CNM effects need to be taken into consideration. These can be separated into three different categories:

- *Cronin Effect* [22] - The effect on the differential cross section due to the transverse momentum (k_T) broadening of the partons that arise from initial-state scattering [55], [56].
- *CNM Energy Loss* - Parton mass sensitive radiative energy loss that stems from the initial-state scattering [21]. If the parton loses a fraction, ϵ , of its energy before the hard scattering, it must carry a larger fraction of the colliding hadron momentum, and therefore a larger x , to satisfy the same final-state kinematics.
- *Dynamical shadowing* - Nuclear modification of the parton distribution functions of the nucleon [23], [24], [25], [26].

Figure 6.17 shows a pQCD calculation for PHENIX π^0 and STAR $(\pi^- \pi^+)/2$ data in Cu+Cu and Au+Au collisions. The prediction comes from an approach to radiative energy loss by Gyulassy et al. [57], denoted GLV, where the main parameter is the gluon density per rapidity, dN_g/dy . Though the theory curves don’t accurately represent the data at low p_T , they do get the level of suppression correct within uncertainties. The same calculation is done for heavy flavor hadrons and the results are shown in Figure 6.18. The top panel shows the R_{AuAu} of electrons from heavy flavor measured by STAR and PHENIX. The flat dashed line is the level of suppression seen in the π^0 from Figure 6.17 and the blue and red theory curves are from B and D mesons

respectively. It is not a direct comparison, but as we increase p_T the bottom component should become more important and it is clear that the contribution from the B mesons does not reach the level of suppression seen in the data. The bottom panel in Figure 6.18 shows the same calculation for the Cu+Cu data. The 0-10% Cu+Cu bin from this thesis is laid on top of the theory calculation for comparison. In the p_T region where there is suppression, the data and the prediction agree within uncertainties, and though it is still unknown just how much the B contributes, it under predicts the suppression. Nonetheless, the prediction does better for the Cu+Cu data than it does for the Au+Au. The enhancement in the d+Au and peripheral Cu+Cu data would suggest that the initial state is highly modified and would need to be taken into account in the theory.

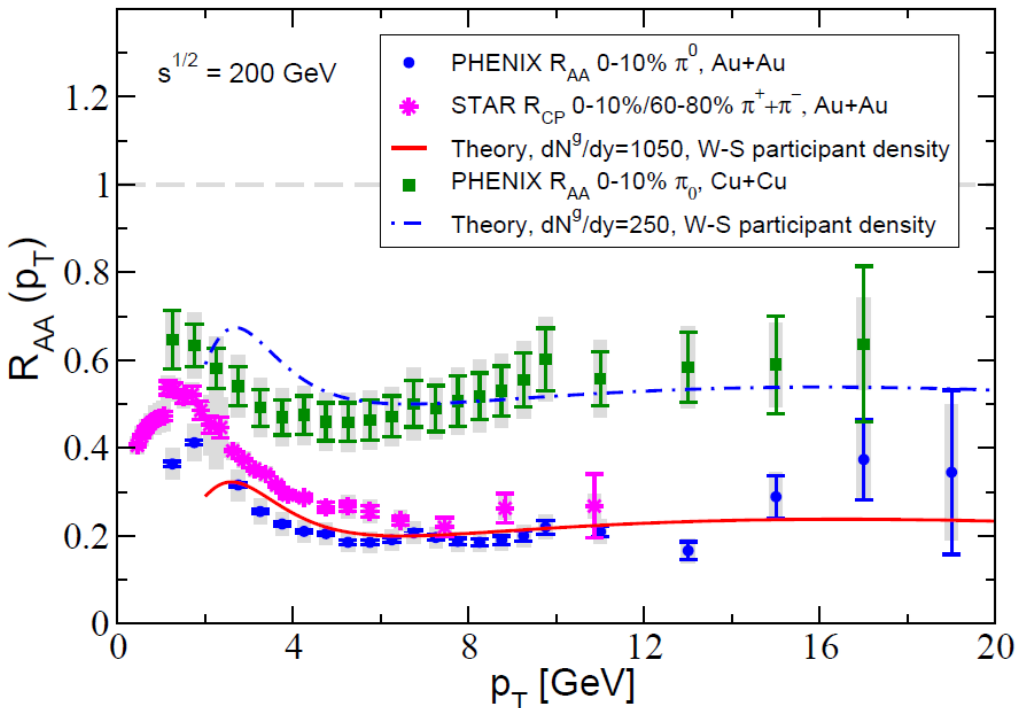


Figure 6.17: Perturbative QCD calculation of the pion suppression in central Au+Au and Cu+Cu collisions at RHIC [58].

6.3.2 Dissociation

The previous section delved into what is now well known, that partonic energy loss in the medium is not sufficient enough to explain the large sup-

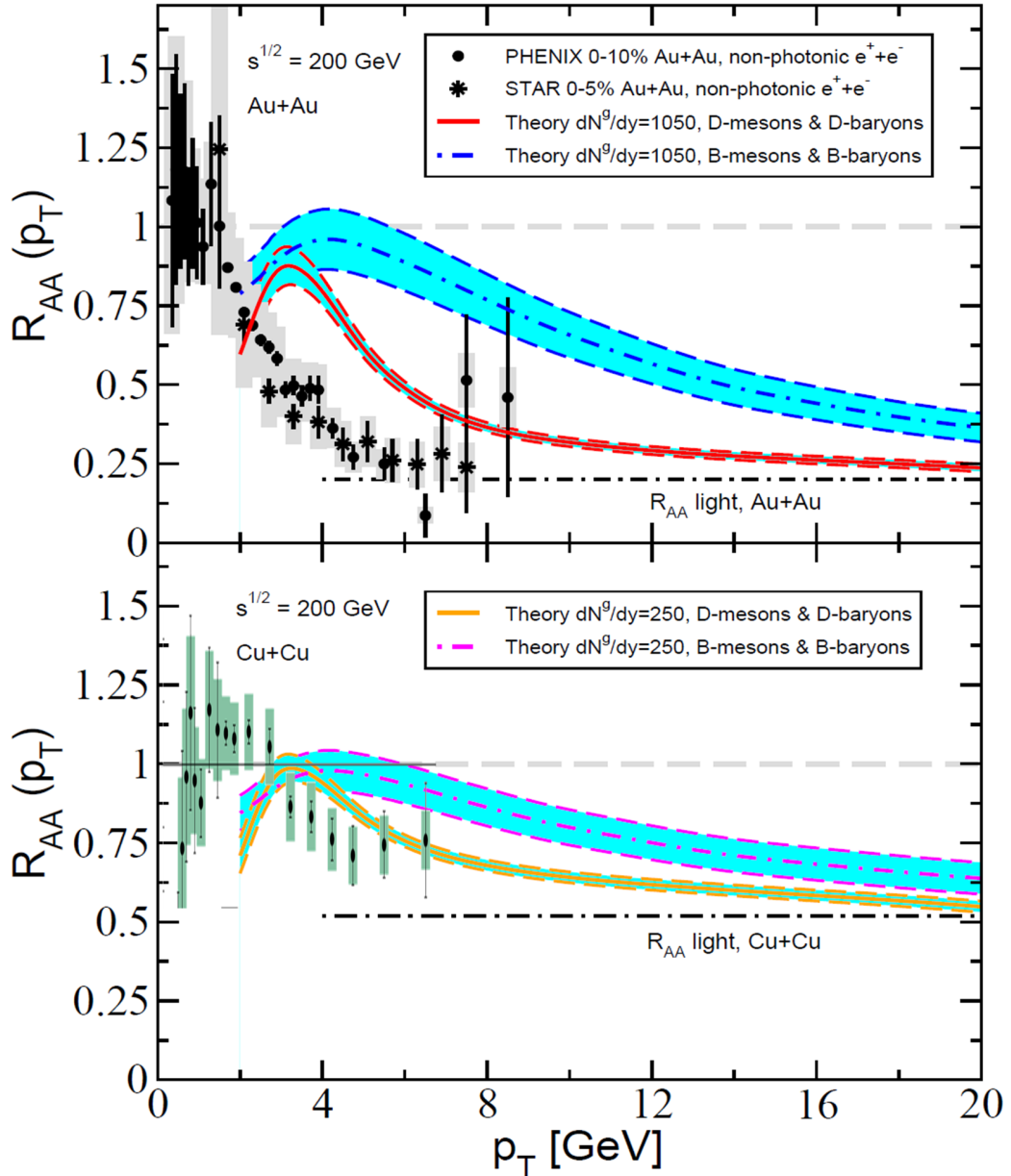


Figure 6.18: Perturbative QCD calculation of D and B mesons production cross sections in central Au+Au (top) and Cu+Cu (bottom) collisions. Calculations are compared to the Au+Au data [59] and the Cu+Cu 0-10% bin from this thesis. The effect of parton mass on the CNM is shown as uncertainty bands [58].

pression seen in the heavy flavor R_{AuAu} . Electrons from heavy flavor are mainly produced by the semi-leptonic decays of D and B mesons. These decays are thought to happen after the mesons have transversed the medium.

The formation time for hadrons is proportional to the energy and inversely proportional to the mass of the hadron. The higher the energy (or p_T) and lighter the hadron the longer the formation time. So for light hadrons (π^0) the formation time is much longer than the lifetime of the medium and thus the pQCD approach holds. For heavy hadrons the formation time can become shorter than the lifetime of the medium. Thus, it is possible for the mesons to dissociate in the medium, which would cause suppression in the heavy flavor electron R_{AA} . This has led to recent studies on the effect of meson dissociation on energy loss [9], [10], [11]. Fragmentation and dissociation are extremely sensitive to formation times of hadrons and the QGP, and the effect will persist longer for bottom and B mesons because of their heavier mass. Figure 6.19 shows an example from [29] which shows good agreement with the heavy flavor electron R_{AA} . However, this calculation does not take into account any CNM effects or the partonic energy loss, both of which are known to have a significant contribution. It should be noted that fragmentation and dissociation simulate suppression by shifting the quarks/hadrons to lower p_T .

6.3.3 The Energy Loss Picture

The effects of partonic energy loss and energy loss from fragmentation and dissociation will both play a part in the total energy loss of electrons from heavy flavor. A new calculation that combines the two effects was made in [58]. It includes all of the CNM effects listed previously. The width of the transverse distribution function due to the initial-scattering grows proportional to ξ which is a numerical factor that accounts for the enhancement of the broadening. They use the light-cone wavefunctions for hadrons and calculate the thermal modification of PDFs and FFs for open heavy flavor in a co-moving plasma. The B mesons are heavier and so the dissociation is the dominant contribution to the energy loss for the entire p_T range at RHIC. On the other hand with its lighter mass the D meson transitions from hadronic energy loss processes to the traditional partonic energy loss. The results for D and B mesons are shown in Figure 6.20. The top(bottom) panel shows the results for the central Au+Au(Cu+Cu) R_{AA} . With the inclusion of fragmentation and dissociation the suppression of the B meson comes on par with that of the D meson. PYTHIA is used to decay the charm and bottom through their semi-leptonic

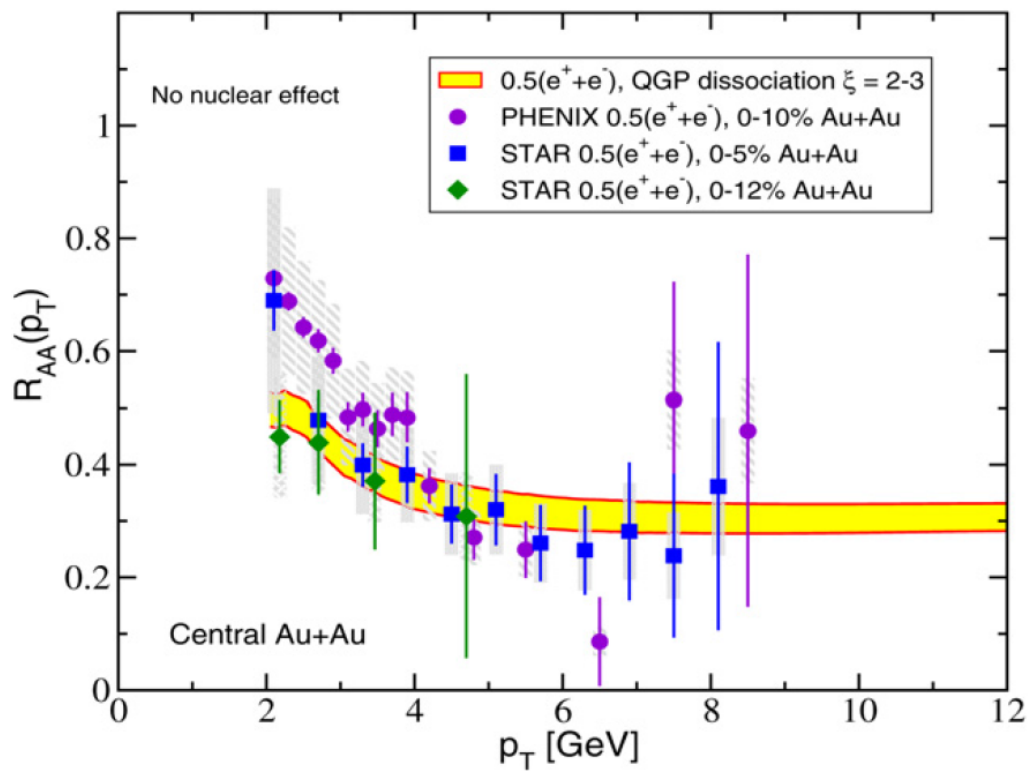


Figure 6.19: Suppression of heavy-flavor electrons from D and B meson spectra softened by collisional dissociation in central Au+Au collisions [9].

channel. The results are shown in Figure 6.21 for the heavy flavor electrons in Au+Au compared to the data and the Cu+Cu predictions. The Au+Au theory matches well with STAR and PHENIX data. In Figure 6.22 the prediction is overlaid with the 0-10% R_{CuCu} bin. Within errors the prediction does agree with the data, though all of the data points are systematically higher.

6.4 Comparison to Forward Results

So far in this thesis we have discussed the results from the semi-leptonic decay of open heavy flavor into electrons at mid-rapidity. Open heavy flavor mesons also decay into muons, a measurement that is made at PHENIX with the muon arms at forward rapidity ($|y|=1.65$) [60]. Making a forward measurement probes a different x region and thus potentially different medium effects. The R_{CuCu} of the muons is shown in Figure 6.23 compared to that of the electrons. The muon result is in three centrality bins, 0-20%, 20-40%, and 40-94%. The 40-60% and 60-94% bins are combined into one in the muon analysis and so the comparison of the 40-94% muon is made with both peripheral bins for the electrons. By the 20-40% bin the results agree in the low p_T region, but then deviate at intermediate p_T .

The most central bin of the heavy flavor muon measurement shows a significant suppression. It is significantly larger than the suppression of the electron in the most central bin, but is at the same level as the central Au+Au electron measurement. Since the Bjorken energy density of the matter produced at mid-rapidity in the central Au+Au collisions is expected to be twice that of the matter produced at forward rapidity in the Cu+Cu collisions, it would suggest that there are additional significant CNM effects at forward rapidity, namely shadowing and initial-state energy loss. The same model calculated for the mid-rapidity Cu+Cu electrons, that was shown previously in Figure 6.22, was calculated for the forward rapidity muons and is shown, with comparison to the electrons and muons, in Figure 6.24 [58]. There is good agreement between the theory and the forward heavy flavor muons. Though the prediction is in better agreement with the muons than the electrons, it is clear that the theory predicts different effects for the mid-rapidity electrons and the forward rapidity muons. These models that now succeed in fitting the heavy flavor electrons in Au+Au, in addition to the heavy flavor muons in Cu+Cu, overpredict the amount of suppression in the Cu+Cu heavy flavor electrons. This would suggest that there still isn't a good understanding of the interplay between hot and cold nuclear matter effects. Further studies that include the

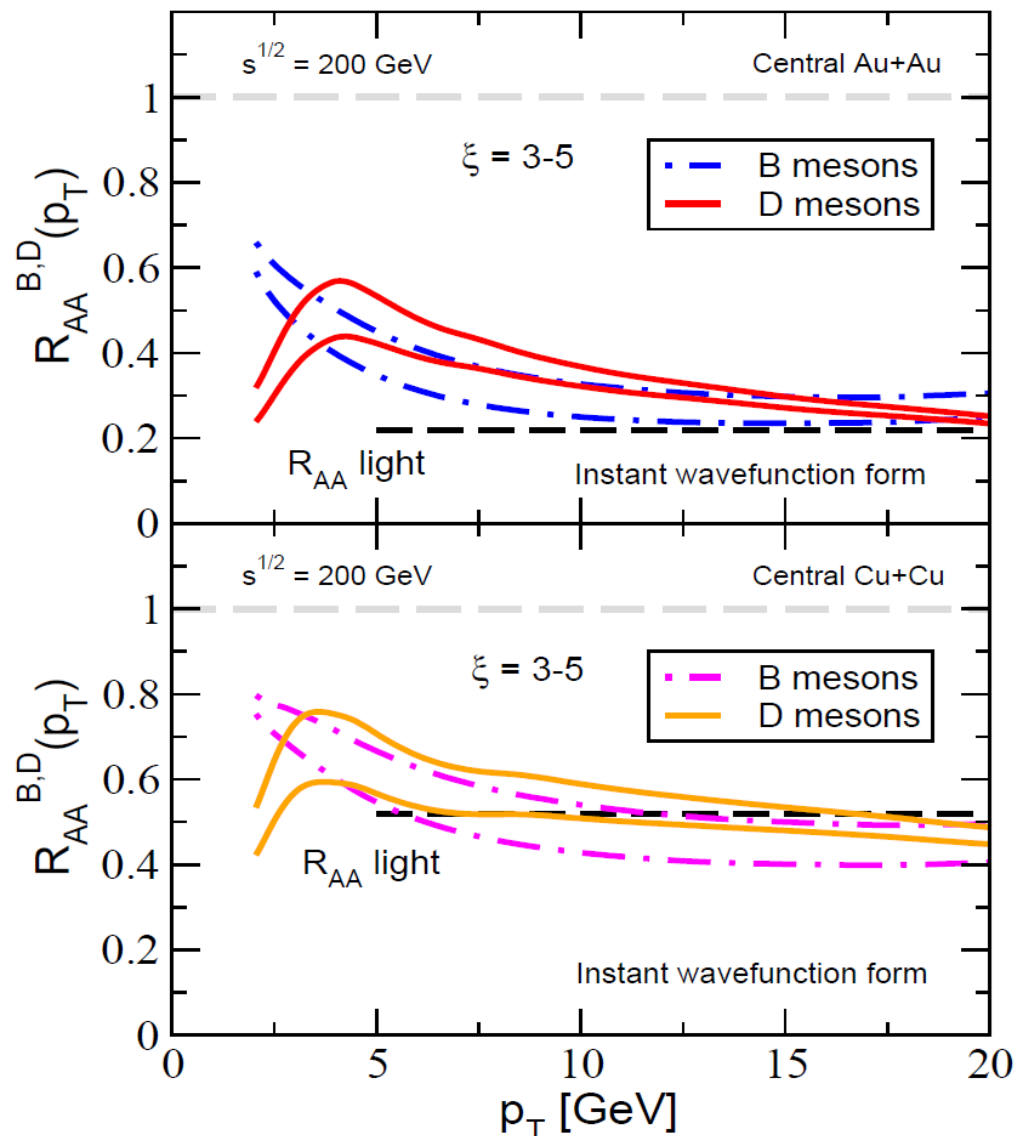


Figure 6.20: Suppression of D and B production from dissociation and partonic energy loss in central Au+Au (top) and Cu+Cu (bottom) [58].

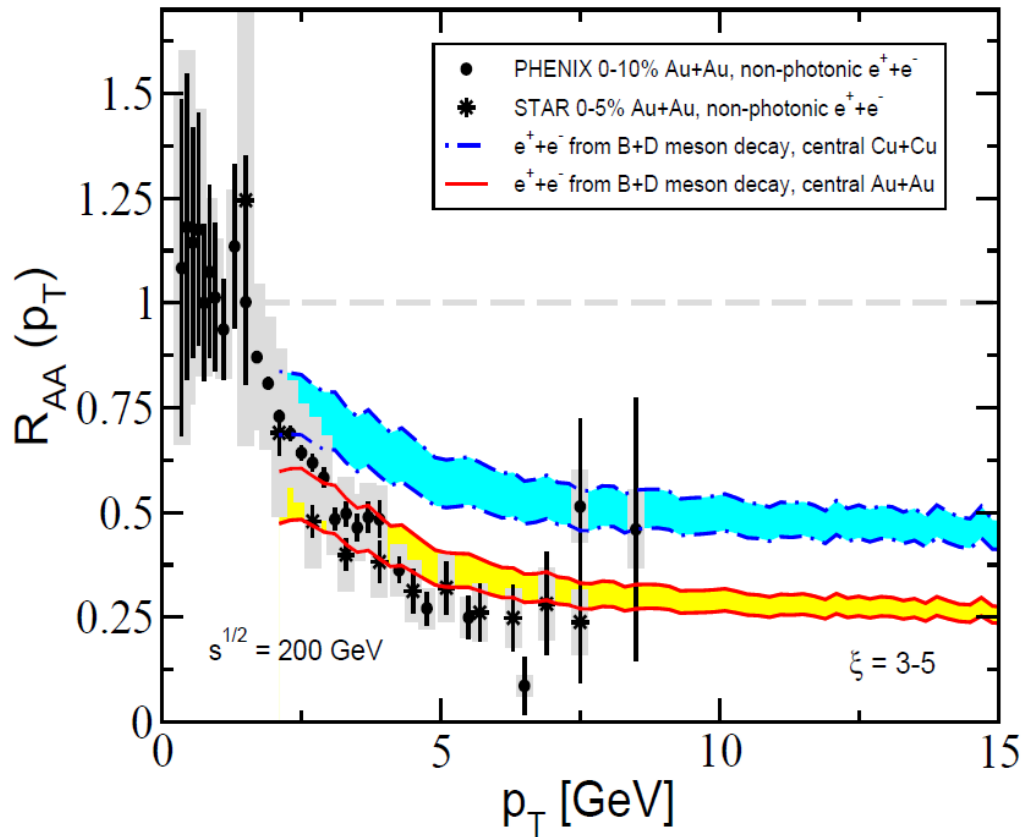


Figure 6.21: R_{AA} for single non-photonic electrons in central Au+Au and Cu+Cu collisions [58].

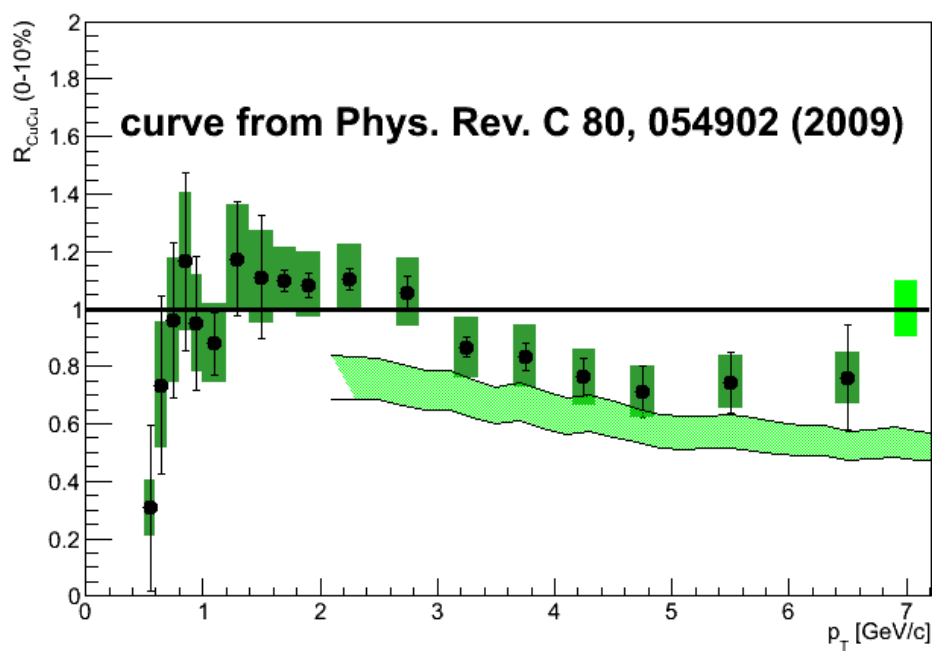


Figure 6.22: R_{CuCu} for 0-10% central collisions compared to suppression due to meson dissociation and heavy quark quenching [58].

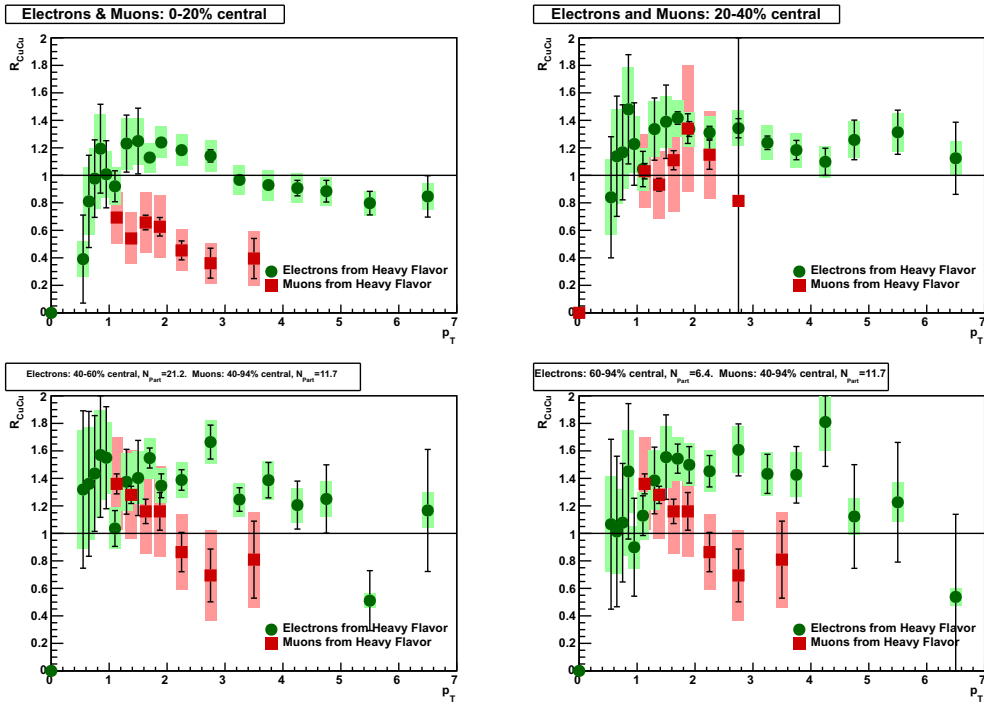


Figure 6.23: R_{CuCu} for electrons and muons from heavy flavor. From top left: e and μ 0-20% central, e and μ 20-40% central, e 40-60% central and μ 40-94% central, e 60-94% central and μ 40-94% central. [60].

d+Au heavy flavor electrons and the more peripheral heavy flavor electrons in Cu+Cu could help to nail down these competing effects.

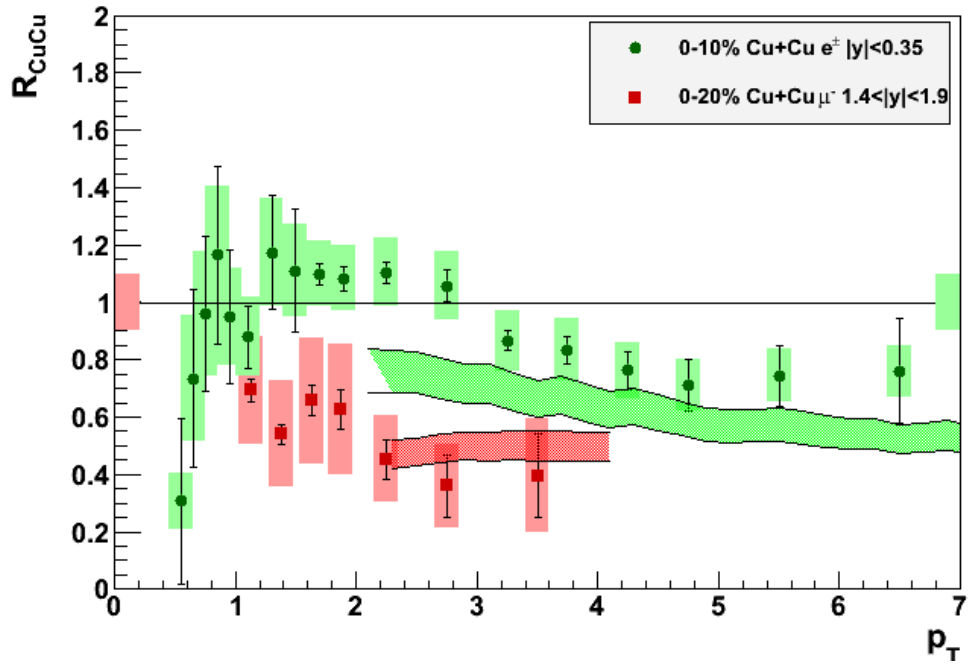


Figure 6.24: R_{CuCu} for electrons and muons from heavy flavor [60]. Theory curves are from [58].

Chapter 7

Conclusion

In this thesis we have presented a measurement of electrons from the semi-leptonic decay of heavy quarks in Cu+Cu collisions at $\sqrt{s} = 200\text{ GeV}$. The invariant yields were shown along with the nuclear modification factor, R_{CuCu} as a function of p_T for 5 different centralities. The analysis of the Cu+Cu data has bridged the gap between the suppression seen in the Au+Au result and the enhancement seen in the d+Au result. R_{CuCu} has shown statistically significant modification from the p+p result in most centrality bins. The most central R_{CuCu} is suppressed in relation to the N_{coll} scaled p+p result, which is in agreement with what is seen in the Au+Au result. The peripheral R_{CuCu} show an enhancement that is in agreement with the d+Au result. We have plotted the R_{AA} for the three different collision species as both a function of N_{coll} and N_{part} and, though the error bars are large, we can see the transition of the CNM effects seen clearly in the d+Au and peripheral Cu+Cu to the takeover of the hot medium as the system size increases in the central Cu+Cu and Au+Au.

It has been shown previously, and again in this thesis, that partonic energy loss models alone are not enough to describe the suppression seen in the central Au+Au results. In particular the predicted suppression of the B mesons is less than that of the D mesons, which leads to an underprediction of the suppression of the heavy flavor electrons in Au+Au at high p_T , where we expect the B contribution to be dominant. A similar calculation for the central Cu+Cu is in closer agreement, but the B meson is still under-suppressed. New results include the effects due to CNM, particularly the Cronin effect and CNM energy loss. The dissociation of mesons in the medium has been suggested as an additional source contributing to the suppression. This effect is largest in the B mesons because their higher mass makes for a shorter formation time

and thus a chance to dissociate in the medium. On its own, dissociation does a good job of describing the data, but it is not a complete picture since there is known partonic energy loss. A new calculation was done for the central Au+Au data that combines both the partonic energy loss and dissociation and describes the data well. The same calculation was done for the Cu+Cu and is systematically lower than the suppression seen, but does agree within error. The addition of the enhanced peripheral Cu+Cu data will provide a different look and could give constraints to the initial state and CNM effects that are present in the central events, but masked by the hot medium. Finally the Cu+Cu at mid-rapidity from this thesis were compared to results from single muons from heavy flavor at forward rapidity. The forward results were shown to be more suppressed in comparison to the mid-rapidity results, but this is supported by the theory with the addition of more CNM energy loss effects.

These new results for single electrons from heavy flavor in the Cu+Cu data show that there is much more to look for in these analyses. The addition of the enhancement in the d+Au results and the peripheral Cu+Cu results should provide more constraints on the energy loss picture that has been continuously studied. The installation of new detectors, namely the Silicon Vertex Detector (VTX) and the Forward Vertex Detector (FVTX), will provide the opportunity to separate charm and bottom mesons by their decay lengths. Separating the charm and bottom contributions will be essential for constraining theories with predictions for heavy flavor energy loss in the medium. But until all three beam species are collided again, the data presented in this thesis provides a crucial stepping stone to unfolding the many different, competing affects of the medium produced at RHIC.

Appendix A

Heavy Flavor Spectra

p_T	yield	stat. error	sys. error
0.55	0.00257239	0.00149206	3.29109e-05
0.65	0.00214701	0.000727913	0.000131235
0.75	0.0017387	0.000406646	0.000109404
0.85	0.00123391	0.000249202	9.78755e-05
0.95	0.0007829	0.000138793	5.93158e-05
1.10	0.000375556	1.14564e-05	0.000111216
1.30	0.000208301	4.7273e-06	4.49007e-05
1.50	0.000101825	2.33837e-06	2.01624e-05
1.70	5.13157e-05	1.21097e-06	9.39032e-06
1.90	2.84495e-05	7.01552e-07	4.64208e-06
2.25	1.04712e-05	2.063e-07	1.62198e-06
2.75	3.05329e-06	8.7351e-08	4.21789e-07
3.25	8.92606e-07	1.84383e-08	1.23349e-07
3.75	3.34531e-07	9.94013e-09	4.45689e-08
4.25	1.35108e-07	5.86725e-09	1.7883e-08
4.75	5.99117e-08	3.70885e-09	7.92538e-09
5.50	1.89721e-08	1.36102e-09	2.71953e-09
6.50	5.5773e-09	6.72014e-10	7.77392e-10
8 10.	94804e-09	2.27773e-10	2.37675e-10

Table A.1: Heavy-flavor $\frac{e^+ + e^-}{2}$ yield, 0-94% MB centrality. Yield and errors in units of $(\text{GeV}/c)^{-2}$, p_T is in units of GeV/c .

p_T	yield	stat. error	sys. error
0.55	0.00445674	0.00409087	0.000287499
0.65	0.00575601	0.00206131	0.000290022
0.75	0.00540785	0.00117522	0.000345631
0.85	0.00378032	0.000741238	0.000267689
0.95	0.00230704	0.000415945	0.000171464
1.10	0.00121009	3.71015e-05	0.000321074
1.30	0.000640344	1.75663e-05	0.000131173
1.50	0.00031632	9.23914e-06	5.66413e-05
1.70	0.000158484	5.37759e-06	2.62845e-05
1.90	8.42824e-05	3.34371e-06	1.29993e-05
2.25	3.21745e-05	1.08703e-06	4.51944e-06
2.75	8.91131e-06	4.76225e-07	1.13898e-06
3.25	2.46601e-06	9.41409e-08	3.30945e-07
3.75	9.01794e-07	5.16045e-08	1.19879e-07
4.25	3.44878e-07	3.01384e-08	4.73969e-08
4.75	1.45253e-07	1.88507e-08	2.06436e-08
5.50	5.20877e-08	7.39171e-09	7.51573e-09
6.50	1.51722e-08	3.63012e-09	2.21117e-09
8.00	5.18458e-09	1.27061e-09	6.54079e-10

Table A.2: Heavy-flavor $\frac{e^++e^-}{2}$ yield, 0-10% centrality. Yield and errors in units of $(\text{GeV}/c)^{-2}$, p_T is in units of GeV/c .

p_T	yield	stat. error	sys. error
0.55	0.00472469	0.00372041	9.22161e-05
0.65	0.00527723	0.00185123	0.00041169
0.75	0.00456502	0.00104727	0.000355239
0.85	0.00322058	0.000651133	0.00027594
0.95	0.00203387	0.000364771	0.000174035
1.10	0.00105291	3.13798e-05	0.000268491
1.30	0.000557889	1.37419e-05	0.000111008
1.50	0.000295756	6.75283e-06	4.82567e-05
1.70	0.00013525	3.86339e-06	2.27507e-05
1.90	8.01942e-05	2.29855e-06	1.13704e-05
2.25	2.8635e-05	7.30955e-07	3.89775e-06
2.75	8.00232e-06	3.14427e-07	1.00958e-06
3.25	2.28545e-06	6.49924e-08	2.95746e-07
3.75	8.34529e-07	3.55579e-08	1.0798e-07
4.25	3.40398e-07	2.11707e-08	4.39677e-08
4.75	1.5005e-07	1.33701e-08	1.9531e-08
5.50	4.63327e-08	4.98004e-09	6.54218e-09
6.50	1.40441e-08	2.49601e-09	1.96685e-09
8.00	5.54708e-09	9.03954e-10	6.02361e-10

Table A.3: Heavy-flavor $\frac{e^++e^-}{2}$ yield, 0-20% centrality. Yield and errors in units of $(\text{GeV}/c)^{-2}$, p_T is in units of GeV/c .

p_T	yield	stat. error	sys. error
0.55	0.00412158	0.00195221	0.000522219
0.65	0.00300883	0.000947319	0.000310068
0.75	0.00221521	0.000528306	0.000202309
0.85	0.00162073	0.000322656	0.000129817
0.95	0.00100533	0.000182877	8.74062e-05
1.10	0.000485488	1.5684e-05	0.000127488
1.30	0.000245814	7.37865e-06	5.33086e-05
1.50	0.000133478	3.89584e-06	2.44591e-05
1.70	6.88431e-05	2.20404e-06	1.12803e-05
1.90	3.51031e-05	1.41453e-06	5.71794e-06
2.25	1.28695e-05	4.49945e-07	1.93483e-06
2.75	3.81849e-06	1.97977e-07	5.11993e-07
3.25	1.18636e-06	4.70918e-08	1.57259e-07
3.75	4.31335e-07	2.561e-08	5.58948e-08
4.25	1.67256e-07	1.50862e-08	2.22708e-08
4.75	8.65504e-08	9.91407e-09	1.05584e-08
5.50	3.09503e-08	3.78478e-09	3.70977e-09
6.50	7.56483e-09	1.76578e-09	9.75219e-10
8.00	2.1029e-09	5.45644e-10	2.45885e-10

Table A.4: Heavy-flavor $\frac{e^++e^-}{2}$ yield, 20-40% centrality. Yield and errors in units of $(\text{GeV}/c)^{-2}$, p_T is in units of GeV/c .

p_T	yield	stat. error	sys. error
0.55	0.00234218	0.000869071	0.000288157
0.65	0.00130109	0.000414729	0.000145844
0.75	0.000986063	0.0002319	9.8087e-05
0.85	0.000622314	0.000140645	5.08581e-05
0.95	0.000459578	8.06198e-05	3.58687e-05
1.10	0.000174017	7.38386e-06	5.15607e-05
1.30	9.15741e-05	3.70568e-06	2.18765e-05
1.50	4.87823e-05	2.0986e-06	9.96953e-06
1.70	2.72313e-05	1.28053e-06	4.85292e-06
1.90	1.27978e-05	8.23199e-07	2.30703e-06
2.25	4.93566e-06	2.66438e-07	7.99281e-07
2.75	1.71321e-06	1.27095e-07	2.25147e-07
3.25	4.32731e-07	2.97541e-08	6.20585e-08
3.75	1.82968e-07	1.69746e-08	2.39623e-08
4.25	6.64665e-08	9.61894e-09	8.98536e-09
4.75	3.11481e-08	6.18658e-09	4.13553e-09
5.50	4.35682e-09	1.86047e-09	1.00369e-09
6.50	2.84246e-09	1.08153e-09	3.86664e-10
8.00	6.24778e-10	3.19841e-10	8.97649e-11

Table A.5: Heavy-flavor $\frac{e^++e^-}{2}$ yield, 40-60% centrality. Yield and errors in units of $(\text{GeV}/c)^{-2}$, p_T is in units of GeV/c .

p_T	yield	stat. error	sys. error
0.55	0.000433115	0.000231174	5.53272e-05
0.65	0.000221744	0.000109385	3.94812e-05
0.75	0.000169313	6.08716e-05	2.48774e-05
0.85	0.000131535	3.78634e-05	1.72484e-05
0.95	6.09664e-05	2.20017e-05	9.49233e-06
1.10	4.33866e-05	2.09725e-06	1.25627e-05
1.30	2.10882e-05	1.12968e-06	5.07833e-06
1.50	1.23618e-05	6.81377e-07	2.35283e-06
1.70	6.20915e-06	4.26464e-07	1.11812e-06
1.90	3.25798e-06	2.88151e-07	5.55732e-07
2.25	1.18046e-06	9.2884e-08	1.91909e-07
2.75	3.78422e-07	4.44762e-08	5.1524e-08
3.25	1.13794e-07	1.12965e-08	1.52457e-08
3.75	4.30212e-08	6.20524e-09	5.43978e-09
4.25	2.28173e-08	4.06989e-09	2.54367e-09
4.75	6.39758e-09	2.14837e-09	8.70315e-10
5.50	2.39237e-09	8.49031e-10	3.24248e-10
6.50	2.9971e-10	3.34781e-10	7.56023e-11
8.00	4.45882e-10	1.7721e-10	4.47191e-11

Table A.6: Heavy-flavor $\frac{e^++e^-}{2}$ yield, 60-94% centrality. Yield and errors in units of $(\text{GeV}/c)^{-2}$, p_T is in units of GeV/c .

Appendix B

R_{CuCu}

p_{T}	R_{CuCu}	stat. error	sys. error
0.55	0.623707	0.388034	0.20353
0.65	0.966358	0.390505	0.291001
0.75	1.08959	0.318525	0.244497
0.85	1.34031	0.362599	0.278122
0.95	1.13691	0.273739	0.199499
1.1	0.962121	0.117778	0.149089
1.3	1.3468	0.226539	0.212546
1.5	1.2607	0.241239	0.181537
1.7	1.25589	0.0296371	0.130943
1.9	1.2884	0.0317713	0.134392
2.25	1.26819	0.0249854	0.132211
2.75	1.27677	0.0365269	0.136697
3.25	1.10667	0.0228602	0.123788
3.75	1.09185	0.0324427	0.127117
4.25	1.05516	0.0458218	0.121847
4.75	1.03528	0.0640889	0.117814
5.5	0.95754	0.0686921	0.108365
6.5	0.985495	0.118743	0.111506

Table B.1: R_{CuCu} , 0-94% centrality. The p_{T} is in units of GeV/c.

p_T	R_{CuCu}	stat. error	sys. error
0.55	0.306374	0.289548	0.100062
0.65	0.734542	0.308681	0.22124
0.75	0.960849	0.268328	0.215628
0.85	1.16424	0.309885	0.241593
0.95	0.949874	0.230821	0.167684
1.1	0.878952	0.107631	0.13707
1.3	1.17386	0.198276	0.186373
1.5	1.11039	0.213419	0.160464
1.7	1.09971	0.0373148	0.115368
1.9	1.08219	0.0429334	0.113804
2.25	1.10482	0.0373268	0.118733
2.75	1.05652	0.0564611	0.119563
3.25	0.866855	0.0330925	0.106548
3.75	0.834495	0.0477533	0.108646
4.25	0.76365	0.0667342	0.0975126
4.75	0.711641	0.0923555	0.089025
5.5	0.745362	0.105774	0.0908695
6.5	0.760097	0.181862	0.0909492

Table B.2: R_{CuCu} , 0-10% centrality. The p_T is in units of GeV/c.

p_T	R_{CuCu}	stat. error	sys. error
0.55	0.390908	0.320136	0.127641
0.65	0.810528	0.335572	0.244112
0.75	0.976202	0.281901	0.219068
0.85	1.19375	0.323143	0.247715
0.95	1.00786	0.244206	0.169906
1.1	0.920456	0.112518	0.136163
1.3	1.23089	0.207376	0.186355
1.5	1.24953	0.239082	0.170379
1.7	1.12953	0.0322648	0.10571
1.9	1.2393	0.0355211	0.116363
2.25	1.18343	0.030209	0.113518
2.75	1.14188	0.0448666	0.116111
3.25	0.9666919	0.0274967	0.107337
3.75	0.929447	0.0396021	0.109511
4.25	0.907158	0.0564198	0.105776
4.75	0.884789	0.0788382	0.1022
5.5	0.797969	0.0857692	0.0903993
6.5	0.846805	0.1505	0.0946037

Table B.3: R_{CuCu} , 0-20% centrality. The p_T is in units of GeV/c.

p_T	R_{CuCu}	stat. error	sys. error
0.55	0.840343	0.44066	0.274242
0.65	1.13881	0.437337	0.342936
0.75	1.16735	0.345579	0.261948
0.85	1.48041	0.397326	0.307193
0.95	1.22765	0.299795	0.20606
1.1	1.04588	0.128514	0.153455
1.3	1.3365	0.226334	0.201086
1.5	1.38968	0.267096	0.189028
1.7	1.41681	0.0453599	0.131704
1.9	1.33681	0.0538685	0.125212
2.25	1.31068	0.0458244	0.123432
2.75	1.34272	0.0696159	0.128702
3.25	1.23687	0.0490969	0.12404
3.75	1.18383	0.0702885	0.123849
4.25	1.09842	0.0990756	0.114551
4.75	1.25766	0.144061	0.132347
5.5	1.31358	0.160631	0.139273
6.5	1.12403	0.262372	0.121348

Table B.4: R_{CuCu} , 20-40% centrality. The p_T is in units of GeV/c.

p_T	R_{CuCu}	stat. error	sys. error
0.55	1.31913	0.572426	0.430431
0.65	1.3603	0.526767	0.409622
0.75	1.43539	0.421105	0.322088
0.85	1.5702	0.453671	0.325824
0.95	1.55026	0.371146	0.258481
1.1	1.03555	0.130395	0.152389
1.3	1.37534	0.235883	0.208235
1.5	1.40296	0.273267	0.192234
1.7	1.54809	0.0727974	0.14551
1.9	1.34628	0.0865974	0.12566
2.25	1.38854	0.0749563	0.12946
2.75	1.66411	0.123452	0.156742
3.25	1.24624	0.0856904	0.12185
3.75	1.38716	0.128691	0.140982
4.25	1.20577	0.174498	0.124345
4.75	1.25026	0.248325	0.129934
5.5	0.510782	0.218117	0.0542498
6.5	1.16667	0.44391	0.127565

Table B.5: R_{CuCu} , 40-60% centrality. The p_T is in units of GeV/c.

p_T	R_{CuCu}	stat. error	sys. error
0.55	1.06661	0.617816	0.348022
0.65	1.01371	0.547491	0.305253
0.75	1.07768	0.431092	0.24182
0.85	1.45119	0.492681	0.301128
0.95	0.899228	0.356054	0.155934
1.1	1.12894	0.144537	0.173374
1.3	1.38488	0.242442	0.217626
1.5	1.55452	0.307492	0.222336
1.7	1.54346	0.106009	0.159394
1.9	1.49859	0.132542	0.154362
2.25	1.45211	0.114258	0.150171
2.75	1.60724	0.1889	0.169282
3.25	1.43297	0.142254	0.156924
3.75	1.42616	0.205704	0.16326
4.25	1.80993	0.322834	0.209305
4.75	1.12284	0.377062	0.131016
5.5	1.22639	0.435235	0.143597
6.5	0.537887	0.600829	0.0631523

Table B.6: R_{CuCu} , 60-94% centrality. The p_T is in units of GeV/c.

Bibliography

- [1] E. Shuryak, Phys. Repts. **61**, 71 (1980).
- [2] I. Arsene et al. (BRAHMS Collaboration), Nucl.Phys. **A757**, 1 (2005), [nucl-ex/0410020](#).
- [3] K. Adcox et al. (PHENIX Collaboration), Nucl.Phys. **A757**, 184 (2005), [nucl-ex/0410003](#).
- [4] B. Back, M. Baker, M. Ballintijn, D. Barton, B. Becker, et al., Nucl.Phys. **A757**, 28 (2005), [nucl-ex/0410022](#).
- [5] J. Adams et al. (STAR Collaboration), Nucl.Phys. **A757**, 102 (2005), [nucl-ex/0501009](#).
- [6] E. Shuryak, Phys. Rev. **C55**, 961 (1997).
- [7] B. Zhang, E. Wang, and X. Wang, Phys. Rev. Lett. **93**, 072301 (1004).
- [8] S. Wicks, W. Horowitz, M. Djordjevic, and M. Gyulassy, Nucl. Phys. A **783**, 493 (2007).
- [9] A. Adil and I. Vitev, Phys. Lett. B **649**, 139 (2007).
- [10] F. Dominguez and B. Wu, Nucl. Phys. A **818**, 246 (2009).
- [11] F. Dominguez, C. Marquet, and B. Wu, Nucl. Phys. A **823**, 99 (2009).
- [12] S. S. Adler et al. (PHENIX Collaboration), Phys. Rev. Lett. **94**, 082301 (2005), URL <http://link.aps.org/doi/10.1103/PhysRevLett.94.082301>.
- [13] A. Adare et al., Phys. Rev. Lett. **97**, 252002 (2006).
- [14] M. Cacciari, P. Nason, and R. Vogt, Phys. Rev. Lett. **95**, 122001 (2005).
- [15] S. Adler et al., Phys. Rev. Lett. **94**, 082301 (2005).

- [16] A. Adare et al. (PHENIX Collaboration), Phys. Rev. C **84**, 044905 (2011), URL <http://link.aps.org/doi/10.1103/PhysRevC.84.044905>.
- [17] A. Adare et al. (PHENIX Collaboration), Phys. Rev. Lett. **101**, 232301 (2008), URL <http://link.aps.org/doi/10.1103/PhysRevLett.101.232301>.
- [18] S. Wicks, W. Horowitz, M. Djordjevic, and M. Gyulassy, Nuclear Physics A **784**, 426 (2007), ISSN 0375-9474, URL <http://www.sciencedirect.com/science/article/pii/S0375947406009699>.
- [19] K. Eskola, H. Paukkunen, and C. Salgado, Journal of High Energy Physics **2009**, 065 (2009), URL <http://stacks.iop.org/1126-6708/2009/i=04/a=065>.
- [20] R. Vogt, International Journal of Modern Physics E **12**, 211 (2003), <http://www.worldscientific.com/doi/pdf/10.1142/S0218301303001272>, URL <http://www.worldscientific.com/doi/abs/10.1142/S0218301303001272>.
- [21] I. Vitev, Phys. Rev. C **75**, 064906 (2007), URL <http://link.aps.org/doi/10.1103/PhysRevC.75.064906>.
- [22] J. Cronin, H. J. Frisch, M. Shochet, J. Boymond, R. Mermod, et al., Phys.Rev. **D11**, 3105 (1975).
- [23] J. Qiu and G. Sterman, Int. J. Mod. Phys. E **12**, 149 (2003).
- [24] J. Qiu and I. Vitev, Phys. Rev. Lett. **93**, 262301 (2004), URL <http://link.aps.org/doi/10.1103/PhysRevLett.93.262301>.
- [25] J.-W. Qiu and I. Vitev, Physics Letters B **632**, 507 (2006), ISSN 0370-2693, URL <http://www.sciencedirect.com/science/article/pii/S0370269305015789>.
- [26] I. Vitev, T. Goldman, M. B. Johnson, and J. W. Qiu, Phys. Rev. D **74**, 054010 (2006), URL <http://link.aps.org/doi/10.1103/PhysRevD.74.054010>.
- [27] S. Adler et al., Phys. Rev. C **74**, 024904 (2006).
- [28] A. Adare et al. (PHENIX Collaboration), Phys. Rev. Lett. **109**, 242301 (2012), URL <http://link.aps.org/doi/10.1103/PhysRevLett.109.242301>.

- [29] A. Adil and I. Vitev, Physics Letters B **649**, 139 (2007), ISSN 0370-2693, URL <http://www.sciencedirect.com/science/article/pii/S0370269307004248>.
- [30] F. Dominguez and B. Wu, Nuclear Physics A **818**, 246 (2009), ISSN 0375-9474, URL <http://www.sciencedirect.com/science/article/pii/S0375947408008245>.
- [31] F. Dominguez, C. Marquet, and B. Wu, Nuclear Physics A **823**, 99 (2009), ISSN 0375-9474, URL <http://www.sciencedirect.com/science/article/pii/S0375947409001833>.
- [32] J. Nagle, PHENIX Analysis Note 900 (2010).
- [33] J. Nagle, S. Belikov, K. Homma, S. Milov, D. Morrison, and K. Reygers, PHENIX Analysis Note 395 (2005).
- [34] M. L. Miller, K. Reygers, S. J. Sanders, and P. Steinberg, arXiv:nucl-ex/0701025v1 (2007).
- [35] K. A. et al., Nucl. Instr. Meth. **A499**, 469 (2003).
- [36] K. A. et al., Nucl. Instr. Meth. **A499**, 489 (2003).
- [37] S. C. Johnson, J. W. Noe, F. Ceretto, A. Drees, T. K. Hemmick, B. Jacak, and F. T. P. Collaboration, *Three-dimensional track finding in the phenix drift chamber by a combinatorial hough transform method* (1998).
- [38] L. A. et al., Nucl. Instr. Meth. **A499**, 521 (2003).
- [39] W. C. M. M. Aggarwal and et al (2000), [nucl-ex/0006007](#).
- [40] N. Kroll and W. Wada, Phys. Rep. p. 1355 (1955).
- [41] R. Averbeck, A. Drees, Y. Akiba, and T. Hachiya, PHENIX Analysis Note 089 (2001).
- [42] A. Adare et al. (PHENIX Collaboration), Phys. Rev. Lett. **101**, 162301 (2008), URL <http://link.aps.org/doi/10.1103/PhysRevLett.101.162301>.
- [43] S. S. Adler et al. (PHENIX Collaboration), Phys. Rev. Lett. **96**, 202301 (2006), URL <http://link.aps.org/doi/10.1103/PhysRevLett.96.202301>.

- [44] S. S. Adler et al. (PHENIX Collaboration), Phys. Rev. C **69**, 034909 (2004), URL <http://link.aps.org/doi/10.1103/PhysRevC.69.034909>.
- [45] Y. Akiba, R. Averbeck, F. Kajihara, and H. Themann, PHENIX Analysis Note 509 (2007).
- [46] D. Hornback and V. Ciancolo, PHENIX Analysis Note 755 (2008).
- [47] A. Adare et al. (PHENIX Collaboration), Phys. Rev. Lett. **101**, 122301 (2008), URL <http://link.aps.org/doi/10.1103/PhysRevLett.101.122301>.
- [48] A. Adare et al. (PHENIX Collaboration), Phys. Rev. Lett. **101**, 122301 (2008), URL <http://link.aps.org/doi/10.1103/PhysRevLett.101.122301>.
- [49] A. Frawley, T. Ullrich, and R. Vogt, Phys. Rep. **462**, 125 (2008).
- [50] W. Vogelsang, personal communication.
- [51] D. Hornback and V. Ciancolo, PHENIX Analysis Note 798 (2009).
- [52] T. Hachiya and Y. Akiba, PHENIX Analysis Note 340 (2004).
- [53] Y. Akiba, R. Averbeck, A. Dion, and F. Kajihara, PHENIX Analysis Note 557 (2007).
- [54] M. Cacciari, P. Nason, and R. Vogt, Phys. Rev. Lett. **95**, 122001 (2005), URL <http://link.aps.org/doi/10.1103/PhysRevLett.95.122001>.
- [55] A. Accardi, arXiv:hep-ph/0212148 (2003).
- [56] I. Vitev, Physics Letters B **562**, 36 (2003), ISSN 0370-2693, URL <http://www.sciencedirect.com/science/article/pii/S0370269303005355>.
- [57] M. Gyulassy, I. Vitev, X.-N. Wang, and B.-W. Zhang (2003), nucl-th/0302077.
- [58] R. Sharma, I. Vitev, and B. Zhang, Phys. Rev. C **80**, 054902 (2009).
- [59] A. Adare et al. (PHENIX Collaboration), Phys. Rev. Lett. **98**, 172301 (2007), URL <http://link.aps.org/doi/10.1103/PhysRevLett.98.172301>.

- [60] A. Adare et al. (PHENIX Collaboration), Phys. Rev. C **86**, 024909 (2012), URL <http://link.aps.org/doi/10.1103/PhysRevC.86.024909>.
- [61] S. A. et al., Nucl. Instr. Meth. **A499**, 480 (2003).
- [62] M. A. et al., Nucl. Instr. Meth. **A499**, 508 (2003).
- [63] M. A. et al., Nucl. Instr. Meth. **A499**, 560 (2003).
- [64] K. A. et al., Nucl. Instr. Meth. **A497**, 263 (2003).
- [65] Y. A. et al., Nucl. Instr. Meth. **A433**, 143 (1999).
- [66] R. Vogt, *Ultrarelativistic Heavy-Ion Collisions* (Elsevier Science, 2007).
- [67] N. Armesto, M. Cacciari, A. D. C. Salgado, and U. Wiedemann, Phys. Lett. **B637**, 362 (2006).
- [68] M. Cacciari, P. Nason, and R. Vogt, Phys.Rev.Lett. **95**, 122001 (2005).
- [69] S. S. Adler et al. (PHENIX Collaboration), Phys. Rev. Lett. **96**, 032301 (2006), URL <http://link.aps.org/doi/10.1103/PhysRevLett.96.032301>.